Functional Role of Medial Septal Projections to the Parasubiculum

Inaugural-Dissertation
to obtain the academic degree
Doctor rerum naturalium (Dr. rer. nat.)

submitted to the Department of Biology, Chemistry, Pharmacy
of Freie Universität Berlin
by

Daniel Parthier

28.09.2021

The experimental work of this thesis was conducted between August 2016 and June 2021 under the supervision of Prof. Dr. Dietmar Schmitz at the Neuroscience Research Centre (NWFZ) of the Charité.

1st reviewer: Prof. Dr. Dietmar Schmitz

2nd reviewer: Prof. Dr. Mathias F. Wernet

Date of disputation: 10.02.2022

Acknowledgements

First and foremost, I would like to thank my doctoral supervisor Prof. Dietmar Schmitz for his continuous support and advice. I would especially like to thank him for encouraging me to find my own strengths and am grateful for the opportunity to follow my interests in his lab.

Thanks to Prof. Mathias F. Wernet for agreeing to be my second reviewer.

I would like to thank John Tukker for his support, all the idea-sparking discussions over the years, and the time he took to help me to learn more about all the *in-vivo* work.

Thanks to Alexander Stumpf and Rosanna Sammons for helping with some of the recordings that could sometimes feel long, but were more fun together.

Further, I would like to thank Constance Holman, Noam Nitzan and Hung Lo who made the common struggles a little bit more enjoyable and helped to anticipate success. Laura Moreno-Velasquez, Felicitas Brüntgens for wonderful breaks and encouragement throughout the years. Furthermore, I am grateful to Nikolaus Maier and Friedrich Johenning for all the vivid discussions and inputs from day one.

Special thanks to Anke Schönherr, Susanne Rieckmann, and Katja Czieselsky, for keeping everything running and making life for everyone in the lab easier.

I thank all the members of the Schmitz-Lab for all the discussions, the great work environment, and also the lively social events.

My family, who have always been supportive and helped me to become the person I am today.

Finally, Lisa, who was always there for me during challenging times and without whom nothing of this would have been possible. I will always be grateful.

Abstract

Oscillations are a hallmark of brain activity and can be generated by local synchronisation mechanisms. They have been implicated in the communication between brain areas. An important type of oscillations are θ oscillations (4-12 Hz), which are associated with different behaviours, such as movements and navigation, but they also play a crucial role in memory formation and retrieval. One of the major θ rhythm generators in the brain is the medial septum (MS), which with its different types of projecting neurons, innervates many cortical areas and synchronises their activity. I investigated two major projection types of the MS: GABAergic (γ-aminobutyric acid – GABA) and cholinergic (acetylcholine – ACh) projections. Both projections are known to target the medial entorhinal cortex (MEC) and hippocampus. Parvalbumin positive (PV^+) projections of the MS, which are GABAergic, are known to synchronise cortical networks via disinhibition often by inhibiting interneurons. In contrast, cholinergic projections of the MS project to a wide range of cell types in the MEC and hippocampus and can have substantially different effects on the target cell (e.g. activation or inhibition). Thus, their function on a network can range from increasing activity through depolarising excitatory cells, to more inhibition of the network by activating interneurons, or even modulating synaptic integration. Previous studies have focussed on identifying projections to the hippocampus and the MEC but did not consider the parasubiculum (PaS), a major input of the MEC. In this study, we electrophysiologically characterised cells in the PaS and demonstrated layer I interneurons to be distinctly different from putative layer II interneurons. The PaS, with its strong θ rhythmic firing cells, was shown to have the highest density of MS PV^+ fibres in the parahippocampal formation, suggesting that it is an important target of MS projections and yet MS inputs to the PaS are unknown. Using channelrhodopsin (ChR2), a light sensitive ion channel, expressed in the MS of PV-Cre and ChAT-Cre (choline acetyltransferase) mice *in-vivo*, I identified GABAergic and

cholinergic MS connections to the PaS *in-vitro* and demonstrated cell type specific projection patterns. I found that PV^+ MS projections mainly inhibit interneurons in the PaS, including layer I interneurons, representing a novel cortical target of PV^+ MS cells. On the other hand, cholinergic projections depolarise layer I interneurons and have multiple effects on deeper cells of the PaS, leading to a depolarisation or hyperpolarisation. To investigate a potential role of GABAergic projections in θ generation, I recorded local field potentials (LFP) in awake head-fixed mice and entrained oscillations in the PaS by stimulating with light in the MS. In contrast, local stimulation of fibres in the PaS could not entrain oscillation, suggesting that increased activity in the PaS might be required for MS PV^+ cells to entrain θ. Taken together, stimulation of PV^+ cells in the MS is sufficient to drive oscillations in the PaS, likely via disinhibition in line with other areas as the MEC and hippocampus. However, novel targets in layer I could be involved via cholinergic activation and GABAergic entrainment. Whether cholinergic activation by itself can entrain θ remains to be further investigated.

Zusammenfassung

Oszillationen sind ein Kennzeichen von Gehirnaktivität und können durch lokale Synchronisationsmechanismen generiert werden. Sie spielen eine wichtige Rolle bei der Kommunikation zwischen Gehirnarealen. Ein wichtiger Typ von Oszillationen sind θ Oszillationen ($4-12\ Hz$), welche mit verschiedenen Verhalten wie Bewegung und Navigation assoziiert sind und eine wichtige Rolle in der Gedächtnisbildung und -abrufung spielen. Einer der wichtigen θ Generatoren im Gehirn ist das Mediale Septum (MS), welches mit seinen verschiedenen projizierenden Neuronen viele kortikale Regionen innerviert. Ich habe zwei Typen von Projektionen des MS untersucht: GABAerge (γ-Aminobuttersäure – GABA) und cholinerge (Acetylcholin – ACh) Projektionen. Beide Typen projizieren zum Medialen Entohinalen Kortex (MEC) und zum Hippocampus. Parvalbumin positive (PV^+) Projektionen des MS können kortikale Netzwerke via Disinhibition, durch inhibieren von Interneuronen, synchronisieren. Im Gegensatz dazu projizieren cholinerge Projektionen des MS zu verschiedensten Zelltypen des MEC und des Hippocampus und können unterschiedliche weitreichende Effekte auf Zellen haben (z.B. Aktivierung und Inhibierung). Folglich können die Konsequenzen von Aktivierung des Netzwerkes via Depolarisation von exzitatorischen Zellen, über Inhibierung des Netzwerkes via Aktivierung von Interneuronen bis hin zur Modulation von synaptischer Integration reichen. In der Vergangenheit haben Studien sich auf die Identifizierung von Projektionen zum Hippocampus und MECs fokussiert, jedoch nicht zum Parasubiculum (PaS), eines der bedeutendsten Eingänge des MEC. In dieser Studie haben wir elektrophysiologisch Zellen im PaS charakterisiert und konnten herausstellen, dass Schicht I Zellen sich von anderen vermeintlichen Interneuronen in Schicht II unterscheiden. Das PaS, mit seinen im θ Rhythmus feuernden Zellen, hat die höchste Dichte von MS PV^+ Fasern im parahippocampalen Netzwerk, was es als besonderes Ziel für MS Projektionen herausstellt. Dennoch sind Projektionen vom MS

zum PaS nicht untersucht worden. Mit Hilfe von Channelrhodopsin (ChR2), einem lichtsensitivem Ionenkanal, welcher im MS von PV-Cre und ChAT-Cre Mäusen exprimiert wurde, konnte ich GABAerge und cholinerge MS Verbindungen zum PaS *in-vitro* detektieren und Zelltyp-speziefische Projektionen identifizieren. Ich konnte herausstellen, dass PV^+ MS Projektionen hauptsächlich Interneurone im PaS inhibieren. Insbesondere Schicht I Interneurone stellen ein neues kortikales Ziel von PV^+ MS Zellen dar. Im Gegensatz dazu werden Schicht I Interneurone des PaS durch cholinerge MS Projektionen depolarisiert wohingegen Zellen in tieferen Schichten depolarisiert oder hyperpolarisiert werden können. Um zu zeigen, dass man mit GABAergen Projektionen θ generieren kann, nahm ich das lokale Feldpotential (LFP) in Kopf-fixierten Mäusen auf und fand, dass man Oszillationen mit MS-Stimulation gleichschalten kann, jedoch eine Stimulation der Fasern im PaS nicht ausreichend ist. Das weist darauf hin, dass eine erhöhte PaS-Aktivität notwendig ist, um θ Oszillationen im PaS zu generieren. Zusammenfassend zeigt sich, dass eine Stimulation der PV^+ Zellen im MS ausreichend ist, um im PaS Oszillationen zu generieren. Disinhibierung im PaS ist, ähnlich wie auch im MEC und Hippocampus, ein wahrscheinlicher Mechanismus. Weiterhin könnten jedoch neue Ziele von cholinergen und GABAergen Fasern in Schicht I bei der θ Generierung involviert sein. Ob θ Oszillationen durch cholinerge Projektionen gleichgeschaltet werden kann muss jedoch noch durch weitere Studien gezeigt werden.

Contents

1

Introduction

The evolutionary goal of a species is to survive, which is achieved by adapting to environmental conditions, optimising strategies to live in the specific environment and reproduce (Darwin, 1859). Higher organisms, therefore, have developed structures which are able to help with optimising their behaviour on different levels. With multicellular organisms evolving 570 million years ago, more complex functions such as mechanosensation (touch, hearing), olfaction based on chemotaxis, and vision developed (Schlosser, 2018), helping them to learn about their environment. Hence, the encoding of memories evolved and similar mechanisms to achieve memory on the synaptic scale were observed in invertebrates and vertebrates (Glanzman, 2010). Information which is accumulated over the course of time – from being exposed to sensory stimuli – is stored across different areas of the brain or nervous system (Mesulam, 1998; Christophel et al., 2017) and can be encoded for longer by protein synthesis and structural changes in synapses and cells (Hydén and Lange, 1968; Bourne and Harris, 2012). One mechanism to induce such change is through organised cellular activity, resulting in an increase of calcium in dendrites and synapses. Hence, synaptic inputs which occur shortly before postsynaptic activity can increase calcium concentrations enough to induce spike time dependent plasticity (STDP) and protein synthesis to stabilise connections (Hebb, 1949; Dan and Poo, 2006). When different cells strengthen connections based on the same inputs, they become related and act together in the future. Such an association of cells is often referred to as *"cell-assembly"* (Hebb, 1949).

For a distribution network of memory to work, the coordination of areas and timing of cells is crucial for memory formation and can be achieved by oscillatory

activity (Bressler et al., 1993; Varela et al., 2001). These oscillations arise in the brain through changes induced by population activity, synaptic inputs with the resulting membrane potential changes and can be measured as local field potentials (LFP) (Herreras, 2016). One important higher level function, which does not represent solely processing of sensory inputs, is computation for spatial navigation. Navigation strategies can be observed in several species such as ants (Wehner, 2003), drosophila (Neuser et al., 2008; Kim and Dickinson, 2017), bees (Dacke and Srinivasan, 2007), pigeons (Bond et al., 1981; Olson and Maki, 1983), rodents (Morris et al., 1982), bats (Tsoar et al., 2011), and dolphins (Arranz et al., 2018) and is essential for finding food, a partner, or avoiding danger. Over the last decades, the endeavour to understand the *"cognitive map"* (Tolman, 1948) – how we animals use the abstract – or internally generated models of space – has driven research and revealed that several dimensions of space are represented on a cellular or network level in the brain (place, speed, grid, head-direction, vectors, and borders; for review see Poulter et al. (2018)). Coding spatial properties can be achieved by different mechanisms, allowing for a detailed representation of the environment. For instance, place cells fire at a higher rate in discrete positions of the environment which are referred to as place fields (O'Keefe and Dostrovsky, 1971; O'Keefe, 1976; O'Keefe and Conway, 1978). This principle of coding information (in this case, a location), via the number of action potentials over time, is known as rate code. However, this is not the only possible method of transferring information. An additional way an action potential can code space is via the phase code (O'Keefe and Recce, 1993; Skaggs et al., 1996; Mehta et al., 1997). The phase code is based on the position of a spike relative to the ongoing LFP and is thought to communicate information about an animal's position more efficiently than a rate code alone (Jensen and Lisman, 1996; Reifenstein et al., 2012). This has been found to play an important role in several areas of the brain (lateral septum (Tingley and Buzsáki, 2018), medial entorhinal cortex (Giocomo et al., 2007) and the hippocampus (Skaggs et al., 1996)). The major neuronal oscillatory frequency band in mammals involved in the spatial phase code is the θ band.

1.1 θ oscillations

Theta (θ) oscillations range from 4 to 12 Hz (Buzsáki, 2002) and were observed for the first time in the hippocampus and septum of rats and cats by Jung and Kornmüller (1938), as well as later by Green and Arduini (1954) in rabbits and monkeys. Exposure of rats to different stimuli led to different oscillatory responses, including oscillations in the θ range in the hippocampal area, and also in the medial septum. θ oscillations can also be found in humans, where they are associated with memory and spatial navigation (Arnolds et al., 1980; Sarnthein et al., 1998; O'Keefe and Burgess, 1999). Mechanistically, θ oscillations can be differentiated into two different types: atropine-sensitive, "slow" θ ($4-7$ Hz) associated with rest or anaesthesia, and atropine non-sensitive θ which are slightly faster ($7-12$ Hz) and occur during running and exploration (Kramis et al., 1975). This has led researchers to hypothesise that these oscillations are the product of two distinct networks and/or cell types.

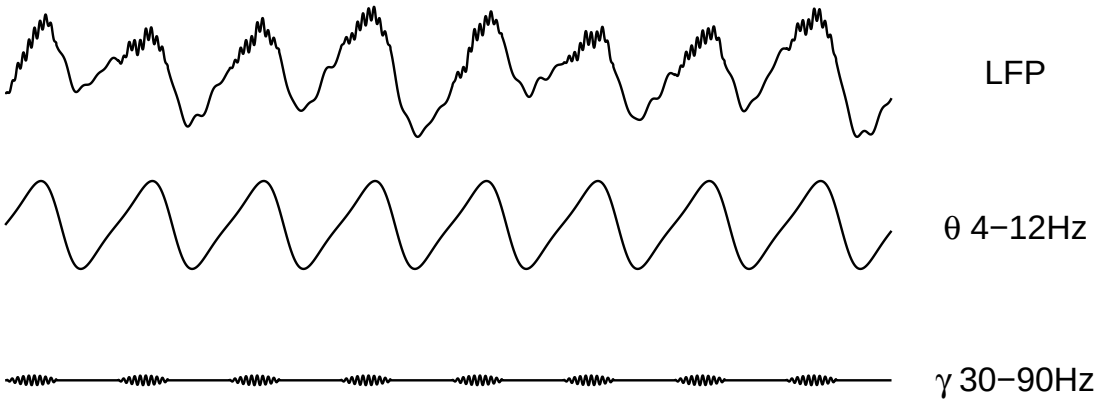

Figure 1: Schematic of θ oscillation with nested γ in LFP. *A scheme of the local field potential (LFP) (top) with the θ frequency band between 4-12Hz (middle) and nested γ oscillations (30-90Hz) at the peak of the θ cycle (bottom).*

An association of θ oscillations with spatial navigation was first reported by Vanderwolf (1969). Freely moving rats show synchronised hippocampal activity reflected in the LFP during exploration (Winson, 1974). Similarly, these oscillations can be found in mice and also humans: in humans they occur with lower frequency (Ekstrom et al., 2005; Watrous et al., 2013; Miller et al., 2018) and as burst activity whereas they are found to be constantly occurring in rodents during movement (Ekstrom et al., 2005; Watrous et al., 2013). Following the early observations in rodents, there

has been a consensus among investigators that oscillations are likely associated with navigation in behaving rodents (Vanderwolf, 1969; O'Keefe and Dostrovsky, 1971).

> * Vanderwolf has reported (and we agree) that the former behaviours are associated with θ activity in the hippocampal EEG, while, during the latter behaviours, the EEG shows irregular slow waves.
>
> — Footnote by J.O'Keefe & J.Dostrovsky regarding behaviours involving movement and rest, 1971

Cortical structures can be considered as *"current generators"* – regions which generate an LFP response through population activity or synaptic inputs – but as far as we know, they are not able to generate θ rhythm by themselves *in-vivo*. In contrast, the *"rhythm generator"* of θ is believed to be in deeper non-cortical regions such as the medial septum (Petsche et al., 1962) which projects to a range of cortical areas including the hippocampal formation. It is not completely proven whether some other areas have the potential to generate θ locally. Although there is no direct evidence for local rhythm generation *in-vivo*, evidence from *in-vitro* studies suggests that connectivity between glutamatergic cells and inhibitory interneurons in combination with membrane properties of cells could be sufficient to generate θ in the hippocampus and parasubiculum (Glasgow and Chapman, 2007; Goutagny et al., 2009). Local interneurons of the hippocampus and the cortex do play an important role in coordinating θ activity and are a primary target of septal projections (Freund and Antal, 1988; Stark et al., 2013; Gonzalez-Sulser et al., 2014). Even though the hippocampus has the capability to generate θ independently of inputs from the isocortex, synchronisation is coordinated by interacting with the parahippocampal network via a feedback loop through the entorhinal cortex (Bragin et al., 1995; Kocsis et al., 1999). Pyramidal cells of the hippocampus use θ cycles for the previously mentioned phase code to represent spatial information more accurately (O'Keefe and Recce, 1993; Skaggs et al., 1996).

In addition to spatial navigation, an increase of θ band coherence between the hippocampus and cortical structures can be observed during other memory tasks, where the increase in coherence is hypothesised to improve learning and memory formation by synchronising synaptic inputs (Huerta and Lisman, 1995; Markram et al., 1997; Bourne and Harris, 2012). A possible mechanism could be a coordinated

depolarisation of dendrites through time-locked synaptic inputs, which can lead to the strengthening of connections via STDP and establish cell-assemblies (Buzsáki, 1989; Huang and Kandel, 2005). Such a synchronisation has been shown to be crucial for working memory where θ oscillations are involved in synchronising activity on the cell level (Jensen and Tesche, 2002; Lee et al., 2005) and across different areas (Sarnthein et al., 1998; Liebe et al., 2012), and in spatial memory where an absence of θ will result in memory deficits (Winson, 1978).

A proposed mechanism of how θ oscillations guide memory formation is by modulating faster γ oscillations ($30 - 90\ Hz$) which are nested in θ cycles (Figure 1) during the encoding and memory retrieval phases. Since local firing was found to be elevated during γ (Soltesz and Deschenes, 1993; Bragin et al., 1995; Colgin et al., 2009), Huerta and Lisman (1995) proposed that, when timed at the peak, nested action potential bursts during θ cycles can result in enhanced long term potentiation and, thereby, stabilise connections. Furthermore, a phenomenon referred to as "replay" – the reactivation of cell assemblies actively coordinated during a previous task – was found to be strongly linked to phases of θ cycles, where an increase in phase locking during θ oscillations was associated with higher performance of working memory (Lee et al., 2005; Fuentemilla et al., 2010). An important implication of these findings is that disruption of θ can lead to a disruption in memory formation; interfering with θ generated in the medial septum by lesioning indeed impairs performance in spatial and working memory tasks (Poucet and Herrmann, 1990; Gerashchenko et al., 2001).

Today, more than 80 years after the first observation of θ, its exact purpose is still not entirely understood, nor are important interactions between different cortical and subcortical areas sufficiently known.

1.2 Medial Septum

The medial septum (MS) is a structure located in the forebrain (Figure 2) and, due to its rhythmic activity, is known to be a central θ generator (Petsche et al., 1962). Because of its widespread connectivity and the oscillatory properties of medial septal cells, it is important for entraining θ and synchronising activity in different areas of the brain (Green and Arduini, 1954; Brücke et al., 1959; Petsche et al., 1962;

Gogolák et al., 1968; Andersen et al., 1979; Rawlins et al., 1979). Depending on the brain state, the majority of cells in the MS show a pronounced rhythmic firing pattern linked to hippocampal θ (Serafin et al., 1996; Dragoi et al., 1999).

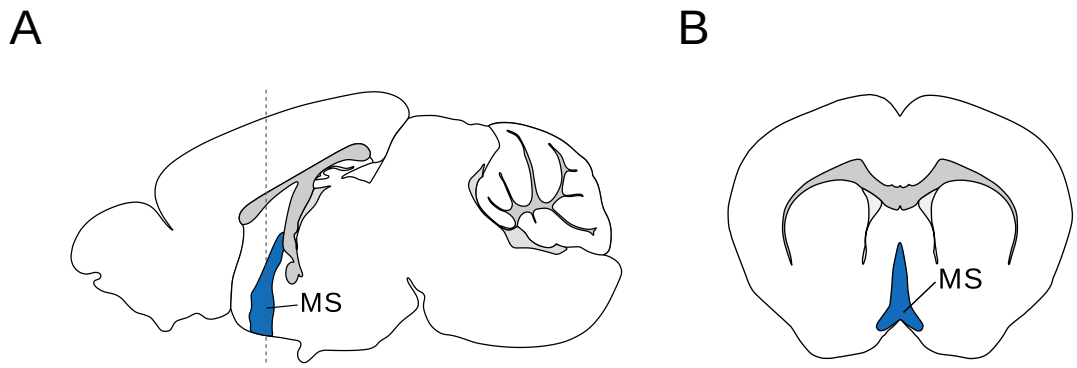

Figure 2: Schematic of medial septum. *Sagittal (A) and coronal (B) section of the mouse brain. Blue shows the location of the MS and dark grey fibre bundles. The dashed line in (A) indicates the position of the section of (B). Modified from Allen Brain Atlas (Sunkin et al., 2013).*

To understand differences between cells in the MS, a substantial amount of work has been put into further identifying diverse electrophysiological properties and different cellular markers in septal neurons (Serafin et al., 1996; Sotty et al., 2003; Lüttgen et al., 2004; Unal et al., 2015). Several important proteins expressed by septal cells, such as hyperpolarisation-activated cyclic nucleotide-gated non-selective cation (HCN) channels or serotonin receptors, can change oscillatory behaviour and be modulated by different network conditions, depending on the brain state (Gaspar et al., 1987; Aznar et al., 2003; Colom et al., 2005; Lüttgen et al., 2005; Varga et al., 2008; Koenig et al., 2011).

GABAergic cells in the septum are known to be associated with the hippocampal θ and fire in bursts at different parts of the θ cycle (Serafin et al., 1996), whereas cholinergic cells fire less rhythmically and exhibit slower firing rates (Pascale Simon et al., 2006). The MS is known to project to the hippocampal and parahippocampal formation, including such target areas as the MEC and the PaS (Raisman, 1966; Alonso and Köhler, 1984; Gaykema et al., 1990; Groen and Wyss, 1990). These projections appear to depend on the neurotransmitter identity and preferentially target specific cell types (Gonzalez-Sulser et al., 2014; Fuhrmann et al., 2015; Unal

et al., 2015; Fuchs et al., 2016; Desikan et al., 2018), leading to synchronicity and potential coordination of network activity across different brain regions. Interfering with this important synchronisation has decisive consequences for learning and memory (Winson, 1978; Chrobak et al., 1989; Mizumori et al., 1990). For example, it has been shown that deactivation of the MS leads to a reduction in exploratory behaviour and impairs working memory (Lee et al., 1988; Poucet and Herrmann, 1990; Brandon et al., 2011; Koenig et al., 2011), making it an integral part of the memory system. Underlining the importance of the MS in hippocampal θ is the onset of cell firing in the MS, which occurs shortly before the onset of hippocampal θ, suggesting that *in-vivo* the MS is a central part of θ rhythm generation (Bland et al., 1999).

In this study, I will focus on GABAergic and cholinergic projections of the MS since they represent the major projecting cell types of the MS (Amaral and Kurz, 1985; Unal et al., 2015). Both groups have been investigated in the past with a major focus on projections to the hippocampus or MEC. However, it should also be noted that the glutamatergic cells of the MS can project to other regions (Fuhrmann et al., 2015; Justus et al., 2017). Early evidence indicated that other regions of the parahippocampal area are also innervated by the MS and could play important roles in θ generation (Swanson and Cowan, 1979). Yet, MS interactions with other regions of the parahippocampal network are rarely investigated even though they heavily project to the medial entorhinal cortex (Canto et al., 2012). Thus, I hypothesise that anatomically confirmed projections target specific cell types in the parasubiculum to entrain θ in the parahippocampal formation.

1.2.1 GABAergic projections

The majority of the MS is made up of GABAergic cells (Freund, 1989) which can be divided into several sub-classes (Hangya et al., 2009) and are generally thought to fire rhythmically in θ bursts. Two major groups were identified by Joshi et al. (2017). One was referred to as "Teevra" cells, a parvalbumin positive (PV^+) cluster firing in strong bursts and targeting PV^+ and cholecystokinin positive (CCK^+) cells in the cornu ammonis 3 (CA3). However, Teevra cells were not found to project to the parahippocampal network, suggesting that they play a role in modulation of the

hippocampus (Joshi et al., 2017). "Komal" cells, a second group of PV^+ cells in the MS, fire preferentially at the peak of the θ phase, whereas Teevra cells are locked at the trough. A subset of Komal cells – referred to as "Orchid" cells – projects to the presubiculum and entorhinal cortex, but the majority of Komal projections have not yet been identified (Viney et al., 2018). Varga et al. (2008) showed that PV^+ cells expressing HCN channels are more likely to fire at the trough of hippocampal θ, as Teevra cells, and are more likely to exhibit bursty behaviour. Other reports suggesting the involvement of HCN come from observations by Xu et al. (2004), where injecting an HCN blocker into the MS lead to reduction of hippocampal θ, further underlining innate cell properties contributing to the oscillatory behaviour of the MS.

GABAergic low-rhythmic-firing neurons (LRN), on the other hand, were recently shown to project to several areas of the hippocampus, make local connections in the MS and receive inhibitory feedback during hippocampal sharp-waves (Salib et al., 2019). Salib et al. (2019) postulated that, indicated by molecular markers, PV^+ LRNs might be more involved in MS local connectivity opposed to MS PV^- LRNs which target the dentate gyrus (DG) and CA3.

We know from other studies that targets of PV^+ cells in the hippocampus or MEC are mainly interneurons which partially express PV themselves and, in the case of the MEC, are mainly located in layer II or III (Freund, 1989; Gonzalez-Sulser et al., 2014; Unal et al., 2015; Fuchs et al., 2016). This target specificity suggests local disinhibition as a common mechanism of PV^+ projections. Calbindin (CB) positive interneurons – a separate group of GABAergic MS neurons – have been shown to project to the MEC targeting low threshold interneurons in mice (Fuchs et al., 2016). However, it was also reported by Unal et al. (2015) that 15% of CB^+ cells in the rat MS express choline acetyltransferase (ChAT) – an enzyme to synthesise acetylcholine – suggesting that the same molecular markers might be expressed by distinct cell types with different neurotransmitters. Interestingly enough, to this day no cortical layer I interneurons have been reported to receive inputs from PV^+ septal projections, highlighting the focus of research on layer II and III of cortical areas. Recently, several studies have provided more evidence that strong PV^+ projections innervate the parasubiculum, indicating possible inhibition

of local networks (Unal et al., 2015; Tang et al., 2016).

However, it is not clear whether these fibres have functional connections and to what extent they preferentially target parasubicular cells as compared to the better-documented MEC, or if they elevate disinhibition. This is an important question which could have implications for communication along the parahippocampal axis (e.g. increased synchronicity) and θ generation.

1.2.2 Cholinergic projections

Cholinergic cells ($ChAT^+$) in the MS are thought to be slowly firing (Manseau et al., 2008) and project to the hippocampus and MEC (Lamour et al., 1984; Frotscher and Léránth, 1985; Unal et al., 2015; Desikan et al., 2018). Similar to the PV^+ cells in the MS, $ChAT^+$ cells project mainly to distinct areas. For example, only a few cells (less than 2%) will project to the CA1 and the MEC simultaneously (Unal et al., 2015). The majority of projection neurons, however, will specifically target one of the two areas. Cholinergic projections can work in different ways due to the properties of acetylcholine, which can slowly inhibit, slowly excite by binding muscarinic receptors or quickly excite a cell via nicotinic receptor binding. All these mechanisms have been shown to be present in cholinergic projections from the MS to the hippocampus or MEC.

In the entorhinal cortex, the majority of cells receiving nicotinic inputs were superficial layer I interneurons and layer II putative $5HT_3R^+$ cells (Desikan et al., 2018). Hyperpolarisation, due to probable activation of type II muscarinic receptors, was observed in pyramidal cells, stellate cells and their intermediates as well as putative PV^+ interneurons (Desikan et al., 2018). A similar pattern was observed in the lateral entorhinal cortex (LEC). It was also reported that cholinergic projections to the DG can inhibit granule cells by activating astrocytes which, in turn, will excite hilar interneurons and mossy cells through glutamate (Pabst et al., 2016). This suggests that an activation of cholinergic cells can result in complex interactions in the network. Indeed, when interfering with cholinergic septal cells using a chemogenetic approach to increase cell firing, θ frequency is reduced in the MEC but grid cell firing was not affected (Carpenter et al., 2017). In comparison, optogenetic activation of cholinergic MS cells leads to a reduced power, including in

the θ frequency band and a slight increase in coherence in the hippocampus, both of which also seem to be state dependent (Vandecasteele et al., 2014). Taken together, these experiments show that cholinergic projections can have different targets and consequences in the parahippocampal formation. Therefore, it is important to collect more cell-specific data on how cholinergic MS cells interact with elements of the parahippocampal network involved in θ generation.

1.3 Parasubiculum

The parasubiculum (PaS) is part of the parahippocampal formation (Figure 3), positioned at the posterior part of the brain (Boccara et al., 2015), and is found across different species (Ding, 2013). There is some disagreement as to whether it is a three-layered (Mulders et al., 1997; Burgalossi et al., 2011; Tang et al., 2016) or six-layered cortex (Funahashi and Stewart, 1997; Glasgow and Chapman, 2007; Boccara et al., 2010) and it is sometimes plainly divided into superficial and deep layers (Sammons et al., 2019). It sits adjacent to the MEC and presubiculum and, therefore, has an important position mediating inputs and outputs of the hippocampal formation (Swanson and Cowan, 1977, 1979; Köhler, 1985; Groen and Wyss, 1990). In particular, connections from the PaS to the MEC have been found to target layer II, mainly exciting their postsynaptic partner cells including cells from other layers (Caballero-Bleda and Witter, 1993; Canto et al., 2012).

It has been shown that the PaS not only has an important role in working memory, but also in spatial memory (Kesner and Giles, 1998; Liu et al., 2001, 2004). The relatively small size and orientation of the PaS rendered *in-vivo* recordings challenging, but they were recently made possible with the use of more recording sites and better targeting approaches. The resulting recordings underlined its role in the processing of spatial information and showed the presence of different spatially-linked functional cell types, including place cells (Taube, 1995), grid cells (Boccara et al., 2010; Ebbesen et al., 2016) and head direction cells (Kornienko et al., 2018). One of the prominent features of PaS cells is the presence of strong rhythmic firing at θ frequency exhibited by pyramidal cells (Ebbesen et al., 2016; Tang et al., 2016). These cells are known to express a protein called Wolframin ER Transmembrane Glycoprotein (WFS1), represent the largest proportion of cells in the PaS (Luuk et

al., 2008; Kitamura et al., 2014; Ray et al., 2014; Ramsden et al., 2015; Sammons et al., 2019) and have an intrinsic oscillatory behaviour which can be modulated by acetylcholine (Glasgow and Chapman, 2013; Salkoff et al., 2015; Sammons et al., 2019).

An increased interest in the PaS has gained traction in recent years, providing the first evidence of MS GABAergic projections to the PaS (Unal et al., 2015; Tang et al., 2016). This further emphasises the prime conditions for the PaS to play a role in the θ generation as part of the parahippocampal network. Therefore, it is important to understand the extent of MS projections to the PaS and the possible effect it has on θ modulation in the context of the parahippocampal formation.

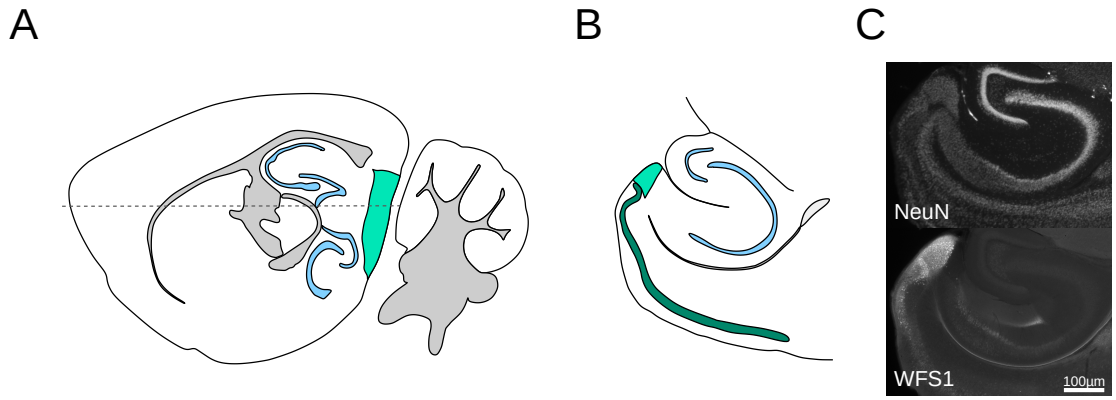

Figure 3: Schematic of parasubiculum. *A sagittal (A) and horizontal (B) section. Turquoise shows the location of the PaS, light grey represents ventricular space and dark grey fibre bundles. The dark green in (B) represents the pyramidal cell layer II of the medial entorhinal cortex. The cornu ammonis and the dentate gyrus are marked in light blue. (C) A horizontal section stained with NeuN, a selective neuronal marker to identify neurons (top). A high density of cells can be observed in the dentate gyrus and cornu ammonis 3. The bottom shows the corresponding WFS1 staining. WFS1$^+$ pyramidal cells can be seen in the PaS, MECII, and CA1 of the hippocampus. Note also stained fibres in the stratum lacunosum-moleculare, resulting from MEC LII projections.*

1.4 Aim of this study

In my thesis, I intend to characterise functional GABAergic and cholinergic MS projections to the PaS and identify their targets. Both types of projections have been shown to be important for θ entrainment and modulation in the MEC and hippocampus. However, up to this point it has been unclear which cell types in the PaS receive inputs from the MS and how they are modulated. Based on the literature

and anatomical studies, it has been assumed that the PaS is strongly innervated by MS GABAergic projections, which might entrain local θ oscillations. However, most of the functional studies available were performed in the MEC, which is strongly innervated by the PaS. Whether or not connections in the PaS are similar to the MEC is uncertain. Hence, it is important to understand how the PaS is modulated by MS projections in order to understand the consequences for the parahippocampal formation.

To address these questions, we analysed functional connections in PV-Cre and ChAT-Cre animals from the MS to different cell types of the PaS. To probe whether interneurons were preferentially targeted – as it was shown in the MEC – we recorded *in-vitro* cells across all the layers of the PaS and measured synaptic responses induced by optical stimulation. Using the same approach, we screened connections in ChAT-Cre animals to identify cholinergic inputs and their effects on different cell types. Once targets of GABAergic PV^+ MS projections were identified, we sought out to investigate θ entrainment in intact networks *in-vivo* using silicon probe recordings and optogenetic stimulation of the MS and projecting fibres.

2

Materials and methods

2.1 Animals

Animal husbandry and experimental procedures were conducted in accordance with European guidelines and with permission from local regulatory authorities (Berlin Landesamt für Gesundheit und Soziales, permits G0092/15 and G0150/17). The total number of animals used for this study were as follows: 32 transgenic PV-Cre mice (JAX: 008069) and 25 transgenic ChAT-Cre (MMRRC: 037336). Animals were housed on a 12 hours reversed day-night cycle with access to food and water *ad libitum*.

2.2 Surgical procedures

2.2.1 Stereotactic injections

For all surgical procedures, the mice were anaesthetised with isoflurane (1.5% vol/vol in oxygen, CP-Pharma, Burgdorf, Germany) and received carprofen (5 $\frac{mg}{kg}$) as analgesia in addition to subcutaneous application of lidocaine as local analgesia at the site of incision. Animals were placed into a stereotaxic frame where they were fixed and stabilised with ear bars. After disinfecting the place of incision with iodide (Betaisodana, Mundipharma, Frankfurt, Germany) a 1 cm incision was performed on the midline. The skin was fixed to the side so that the skull was easily accessible.

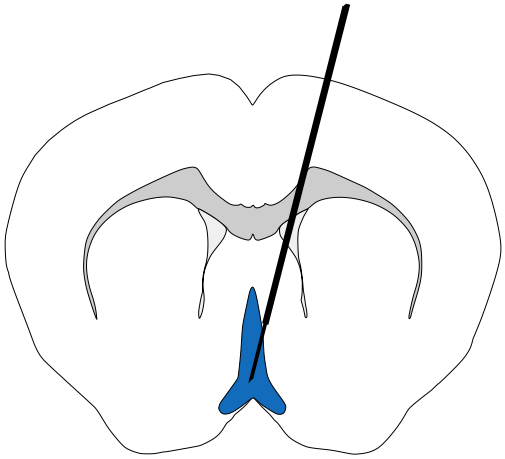

Figure 4: Injection site in medial septum. *Schematic of medial septum (blue) and the injection cannula (black). A* $10°$ *angle is used to avoid damage to superior sagittal sinus which is located on the midline on top of the brain surface (not shown).*

The skull was virtually levelled using a robot stereotaxic (Neurostar, Tübingen, Germany) and a craniotomy drilled at the position of entry (in mm from bregma: 0.7 anterior, 0.7 lateral). A NanoFil syringe (World Precision Instruments, Sarasota County, FL, US) with a 34-gauge needle with adeno-associated virus 1 (AAV1) containing the plasmid for the yellow fluorescent protein (YFP) and channelrhodopsin (*pAAV-EF1α-doublefloxed-hChR2(H134R)-EYFP-WPR* at $6.26 \cdot 10^{11}$ VG/ml) was placed with a $10°$ angle through the hole and slowly moved 3.8 mm downwards along the dorsoventral axis to the MS (Figure 4). The position was held for 5 min before 200 nl of the virus was injected at a rate of 40 nl/min. The needle was left for a further 5 min and then slowly withdrawn. The animal's temperature was maintained at 37 $°C$ during the whole procedure, its eyes were covered with eye-cream to provide moisture, and anaesthesia was checked regularly. The incision was closed and the animal was put back into its home cage to recover. Animals generally woke up in less than 15 min. Animals' body weight and general wellbeing were checked daily, and they were allowed to recover for at least 4 weeks.

2.2.2 Head fixation bar implant

Previously injected animals subject to *in-vivo* awake head-fixed recordings were given a headbar implant. Surgical procedures were similar to what was described in section 2.2.1. However, after the incision a craniotomy was made at a more

anterolateral position (in *mm* from bregma: 1.2 anterior, 1.2 lateral to the right) to place a screw for grounding. The screw was fixed without damaging the surface of the brain. The skull surface was then sealed using OptiBond™ Solo Plus (KerrHawe SA, Bioggio, Switzerland) and a gold pin attached to the screw was stabilised using CHARISMA® ABC A1 (Kulzer GmbH, Hanau, Germany). A headbar was placed over the skull, aligned to midline and fixed with Paladur® dental cement (Kulzer GmbH, Hanau, Germany). The animal was then released back to the home cage where it could recover for at least two days before habituation began.

2.3 *In-vitro* recordings

2.3.1 Slice preparation

To prepare acute slices, animals (n = 19 PV-Cre mice, n = 25 ChAT-Cre mice) were deeply anaesthetised under isoflurane and then decapitated. The brain was quickly removed and transferred to ice-cold ($\sim 4\ ^{\circ}C$) slicing solution (sucrose artificial cerebral spinal fluid – sACSF). sACSF contained (mM): 87 NaCl, 26 $NaHCO_3$, 10 Glucose, 50 Sucrose, 2.5 KCl, 1.25 NaH_2PO_4, 0.5 $CaCl_2$, 3 $MgCl_2 \cdot 6H_2O$. The forebrain was separated from the rest by making a coronal cut. The posterior part of the brain was separated with a sagittal cut between the two hemispheres. The two posterior hemispheres and the forebrain were placed on a vibrating blade microtome (VT1200S, Leica Biosystems, Wetzlar, Germany) to produce 400 μm horizontal and coronal slices (Figure 3 B) which were then transferred for storage to an interface chamber for up to 1-6 hours. Slices were superfused constantly with oxygenated ACSF (in mM: 119 NaCl, 26 $NaHCO_3$, 10 Glucose, 2.5 KCl, 1 NaH_2PO_4, 2.5 $CaCl_2$, 1.3 $MgCl_2 \cdot 6H_2O$). All solutions were saturated in oxygen using carbogen (95% O_2 and 5% CO_2). To verify channelrhodopsin (ChR2) expression fluorescence was checked in medial septal coronal sections under a fluorescence microscope (DM3000, Leica Biosystems, Wetzlar, Germany) prior to recordings.

2.3.2 Slice recordings

Slices were transferred from the interface storage to the recording chamber where they were constantly superfused (at 3.5 ml/min) with oxygenated ACSF and main-

tained at $32 - 34\ ^{\circ}C$. Cells were visually identified using an upright microscope (BX51W1, Olympus, Tokyo, Japan) and infrared differential interference contrast microscopy through a digital camera (XM10-IR, Olympus, Tokyo, Japan). To record in the whole-cell patch-clamp configuration, a borosilicate glass electrode (Harvard Apparatus, Holliston, Massachusetts, USA) was pulled on a DMZ-Universal-Electrode-Puller (Zeitz-Instruments, Martinsried, Germany) to $2.5-6\ M\Omega$ and filled with intracellular solution (in mM: 120 K-Gluconate, 10 HEPES, 10 KCl, 5 EGTA, 2 $MgSO_4 \cdot 7H_2O$, 3 MgATP, 1 NaGTP, 5 Phosphocreatine Na, 0.2% Biocytin). Data was recorded with a Multiclamp 700A/B amplifier (Molecular Devices, LLC., San Jose, CA, USA) and signals were filtered at 10 kHz, sampled at 20 kHz and then digitised. Data was digitised by a Digidata 1550 (Molecular Devices, LLC., San Jose, CA, USA) for use in pClamp. In recordings in IGOR Pro 6.12 (WaveMetrics, Inc., Portland , OR, USA) or WinWCP V5.3.7 (Dempster, 1997), a BNC-2090 interface board (PCI 6035E A/D Board, National Instruments, Austin, Texas, USA) or a USB-6229 BNC (National Instruments, Austin, Texas, USA) was used for digitisation. After opening, cells were held in voltage-clamp at $-60\ mV$ to measure series resistance and assess access. As a quality control, cells with more than 25 $M\Omega$ series resistance were excluded from analysis. Pipette capacitance compensation was applied to cells which were then switched to current-clamp configuration with bridge compensation to perform a characterisation of somatic properties (current steps of 40-100 pA).

2.3.2.1 Cell characterisation

The parameters we analysed were resting membrane potential (V_m), input resistance (R_{in}) determined by a linear fit through the input output curve, the membrane capacitance (C_m) by determining the time constant τ using an exponential fit during the hyper and depolarising steps, and the *sag ratio* i.e. the ratio between the steady state of a hyperpolarisation step and lowest deflection during the hyperpolarisation. The medium afterhyperpolarisation ($mAHP$) is a value reflecting the difference between the Vm and the voltage during a window of 200 ms after the depolarisation of the cell. The *rheobase* was estimated by a linear fit through the linear part of a spike input output curve and represents the current required to trigger a spike. To

determine the excitability, we estimated the *gain* by using the slope of the linear fit. The maximum spike count before cells saturated was used to estimate the maximum $firing\ frequency$ and for the *threshold* of action potentials the differential of the membrane potential was determined and the point of 5% of the maximum was used as threshold. The *positve* and *negative slope* were derived from the same differential as maximum and minimum, respectively, and a ratio of the two was calculated (*slope ratio*). The width of action potentials was determined by the full width half maximum ($FWHM$). The action potential height ($AP - height$) was calculated as the difference between the *threshold* and the maximum height of the action potential, whereas the after hyperpolarisation (AHP) represents the difference between the *threshold* and the maximum negative voltage deflection during a 2 ms window after the action potential onset. Further, the inter-spike-intervals were calculated as the difference between 2 action potentials (AP 1 and AP 2 - $ISI_{1/2}$, AP 2 and AP 3 - $ISI_{2/3}$, AP 9 and AP 10 - $ISI_{9/10}$) and the ISI_{min} reported as the minimum time delay between 2 spikes. As *adaptation* we used the ratio between the $ISI_{2/3}$ and $ISI_{9/10}$. If a cell did not produce the required number of spikes to calculate $ISI_{9/10}$, we used the ISI of the last action potentials. Parameters were extracted using a custom script written in IGOR Pro 6.12.

2.3.2.2 Cell connectivity

To assess septal connectivity to the PaS, channelrhodopsin expressing fibres in the PaS were activated by 10 ms pulses of blue light (470 nm) from a LED (CoolLED pE-2, Andover, UK) or a mercury lamp (with a TTL-controlled mechanical shutter from Uniblitz, Vincent Associates, NY, United States) coupled to the 60x objective. To elicit inhibitory (IPSPs) or excitatory postsynaptic potentials (EPSPs) and inhibitory (IPSCs) or excitatory postsynaptic currents (EPSCs), a range of light pulse frequencies (10, 20, 40 Hz) was used. Additionally, inputs hidden due to low driving force or simultaneously occurring synaptic inputs were unmasked by changing the holding potential of the cell from $-60\ mV$, to $-80\ mV$ and then to $-50\ mV$ after at least 10 trials, respectively. To detect inputs, the average of single trials was calculated and the peak detected based on 3σ differences from the baseline (100 ms) before stimulation onset. Subsequently, the amplitude was determined

for all stimulation points in the stimulation train by taking the maximum deflection. The baseline for every stimulation point was logged as 10 ms prior to onset. In a subset of recordings, monosynaptic inputs were validated by at first blocking with 1 μM tetrodotoxin (TTX, Tocris Bioscience, Bristol, UK) – a sodium channel blocker which abolishes action potentials – and then reinstating inputs by depolarising the terminals with 100 μM 4-Aminopyridine (4-AP, Tocris Bioscience, Bristol, UK) – a potassium channel blocker. Furthermore, receptor identity was identified by applying 1 μM $GABA_A$-receptor blocker Gabazine (SR 95531 hydrobromide, Tocris Bioscience, Bristol, UK), 10 μM NBQX (Tocris Bioscience, Bristol, UK) – an AMPA receptor antagonist –, 25 μM D-AP5 (Tocris Bioscience, Bristol, UK) – an NMDA receptor antagonist – or a cocktail made of 10 μM DHβE (Tocris Bioscience, Bristol, UK), 0.1 μM MLA (Tocris Bioscience, Bristol, UK) and 10 μM Mecamylamine hydrochloride (Tocris Bioscience, Bristol, UK) to block nicotinic receptor activation.

Liquid junction potential was not corrected for. Slices were fixed in 4% paraformaldehyde (PFA) overnight for immunohistochemistry stainings.

2.4 *In-vivo* recordings

2.4.1 Head-fixed awake immobile recordings

For head-fixed recordings in immobile mice, animals were habituated to the setup and trained to stand still in a small paper tunnel whilst being fixed to the headbar. Animals were trained for 5-7 days with increasing time duration (5 min, 10 min, 30 min, 1 h) until they were able to remain still for up to an hour. After training sessions, mice were rewarded with a droplet of sweetened condensed milk. After the training period, animals were anaesthetised as described in 2.2.1. A craniotomy was performed at 1 mm anterior and 1 mm lateral from bregma and another craniotomy at 2.5 mm lateral on the left and 0 mm anteroposterior from lambda. The probe targeting the MS was placed with an angle of 10° and lowered 4.3 mm from the brain surface. Two ISO-3x-tet-lin optrodes (NeuroNexus, Ann Arbor, MI, USA) with 32 channels – distributed over 3 shanks – each were used to record in the MS and PaS simultaneously and allowed for light stimulation of both regions. The optrode targeting the PaS was lowered perpendicular to the brain's surface at a distance of

2.5-3.5 mm. After the recording session Kwik-Cast (World Precision Instruments Ltd, Hertfordshire, UK) was applied to the craniotomies to protect the brain from drying out.

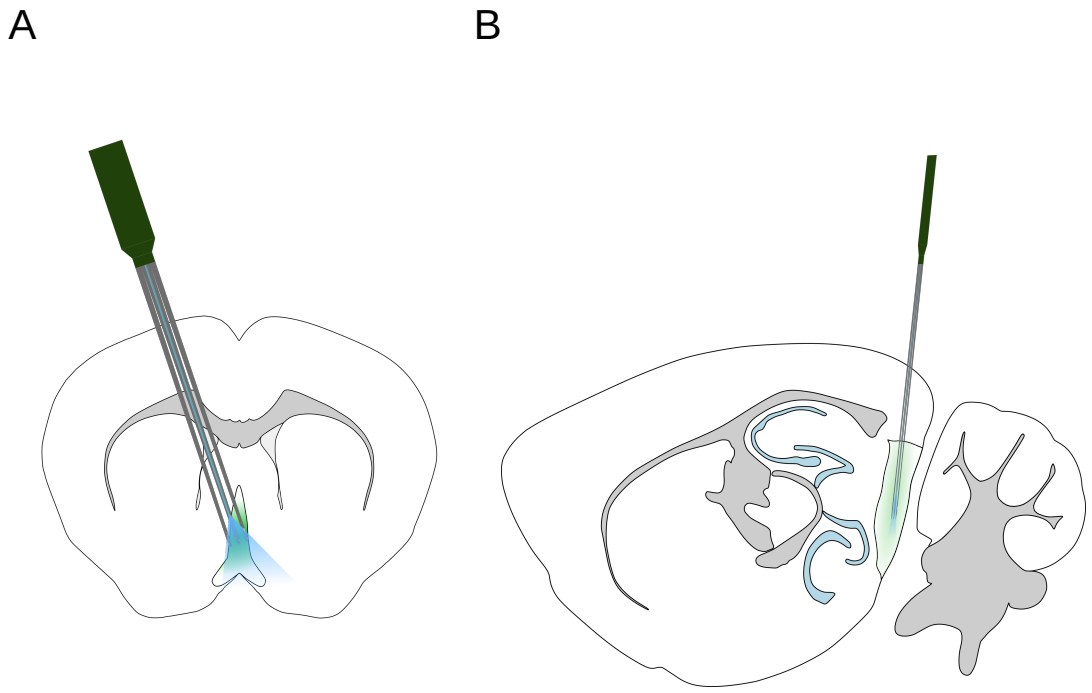

Figure 5: Schematic of probe placement in MS and PaS. *(A) Location of silicon probe in the anterior part to reach the MS. A fibre attached to the probe allows for local stimulation of ChR2 expressing cells (green) using blue LED light (blue cone). (B) Recording side in the PaS with silicon probe. Analogously to the MS, light stimulation can be achieved to activate projections from the MS (green) to the PaS on the fibre level using blue light (blue cone).*

2.5 Histological processing and immunohistochemistry

Animals from *in-vivo* recordings were perfused after the final recording session. Each mouse was deeply anaesthetised using urethane (2.5 $\frac{g}{kg}$ body weight) and transcardially perfused with phosphate-buffered saline (PBS) followed by 4% PFA. The fixed brain was removed and stored in 4% PFA at 4 $°C$ overnight. After post-fixation, brains were washed in PBS before they were dissected into two hemispheres and

a forebrain part. The three parts were blocked onto a vibrating blade microtome (Leica VT1000S, Leica Biosystems, Wetzlar, Germany) and sliced into 75 μm thick sagittal (hemispheres containing the PaS) and coronal (forebrain containing the MS) sections. 400 μm sections from *in-vitro* recordings were fixed in 4% PFA at 4 $°C$ overnight and then transferred to PBS. All slices were washed 3 times (10 min each) and subsequently incubated for 3 hours at room temperature in a blocking solution containing 5% goat serum (NGS, Biozol, Germany), 0.1% Triton-X (Sigma-Aldrich, USA) and PBS. Up to 3 primary antibodies were diluted in 2.5% NGS and incubated with the slices for 48 h at 4 $°C$. The Primary antibodies used in this study were Anti-NeuN (1:1000, ABN90P, Sigma-Aldrich, St. Louis, MO, United States, Sigma-Aldrich, St. Louis, Missouri, United States), Anti-Reelin (1:1000, MAB5364, Millipore, Burlington, MA, USA), Anti-WFS1 (1:1000, 11558-1-AP, Proteintech Group, Inc, Rosemont, IL, USA), Anti-GFP (1:1000, Chicken, Abcam, Cambridge, UK) and Anti-Parvalbumin (1:1000, PV235, Swant, Burgdorf, Switzerland). Following incubation, slices were washed 3 times in PBS (10 min each) before adding secondary antibodies (in PBS). The secondary antibodies used were goat anti-rabbit AlexaFluor-405, goat anti-rabbit AlexaFluor-647, goat anti-mouse AlexaFluor-555 or goat anti-guinea pig AlexaFluor-555, and goat anti-chicken AlexaFluor-488 (Invitrogen, Waltham, MA, USA). After 3 hours of incubation at room temperature, slices were washed 3 times in PBS (10 min each) and mounted on glass using VECTASHIELD® (Vector Laboratories, Burligame, CA, USA). Stained slices were imaged using a Leica TCS SP5 confocal microscope (Leica Biosystems, Wetzlar, Germany) and a fluorescence microscope (DM3000, Leica Biosystems, Wetzlar, Germany) for images requiring smaller magnification.

2.6 Acquisition and stimulation

Signals for *in-vivo* recordings were acquired with a sampling frequency of 20 kHz and digitised using RHD2132 amplifiers and a RHD2000 system (Intan Technologies, Los Angeles, CA, USA). The light stimulation was performed using an LED (wavelength: 473 nm, Plexon Inc., TX, USA) with Spike2 coupled to a Power1401-3A data acquisition interface (Cambridge Electronic Design Limited, Cambridge, UK). Custom scripts were used to drive pulse stimulations for 5 s at different frequencies

(1 Hz, 2 Hz, 4 Hz, 8 Hz, 16 Hz, 32 Hz). 1 Hz (2 ms pulse length) stimulation was used to identify channelrhodopsin expressing cells in the MS, whereas higher frequencies were used to drive network activity in the MS and the PaS. For pulse stimulations between 2 and 8 Hz, nested pulse bursts (5 times 5 ms long single pulse in 16.6 ms intervals) were used to imitate θ burst activity. Pulse frequencies at 16 and 32 Hz were achieved through sequences of single 10 ms long pulses.

2.7 *In-vivo* data analysis

For LFP analysis, data was filtered with a finite impulse response (FIR) low-pass filter (500 Hz) and then downsampled to 1000 Hz. Stimulation blocks were extracted as 15 s segments including 5 s before onset of stimulation and 5 s after the stimulation was finished. Filtering and decompositions were performed in `R version 4.0.3` (R Core Team, 2021) using a custom package (https://github.com/danielparthier/InVivoR). FIR filters were designed using the `signal` package (signal developers, 2014) and applied – via convolution – forward and backwards to the zero-padded signal.

$$\omega = \frac{2\pi f}{f_s} \tag{2.1}$$

$$a = \omega \frac{4\pi}{\sigma + \sqrt{2 + \sigma^2}} \tag{2.2}$$

$$\psi_{a,b}(t) = \frac{1}{\sqrt{a}}(\frac{t-b}{a}) \tag{2.3}$$

$$W(a,b) = \int_{-\infty}^{\infty} x(t)\psi^*_{a,b}(t)dt \tag{2.4}$$

Extracted segments were analysed in the time-frequency domain using wavelet decomposition at 320 different scales (a as shown in (2.2) with f $0.25 - 80$ Hz as angular frequency ω (2.1)). The morlet daughter wavelets were then constructed given the scales (2.3) with a σ of 6 and then convolved with the extracted time series segments (2.4). Units were automatically detected with Kilosort (Pachitariu et al., 2016) and manually curated using Phy (Rossant et al., 2016) and Klusters (Hazan et al., 2006). Spike autocorrelograms were computed by taking the difference between spike times for any given spike in a window of 1 s. Then units were checked

for a clean refractory period to exclude multi-unit activity. To extract the θ or δ phase and power from the LFP at the time point of a spike, the downsampled LFP was filtered using a band-pass FIR filter ($\theta: \ 4-12 \ Hz$, $\delta: \ 1-4 \ Hz$). The Hilbert transform was applied to the filtered signal and the phase and power at spike time points extracted. For the phase analysis of spikes, only spikes with a θ-δ power ratio of more than 2 were considered.

2.8 Statistical analysis

For comparison of groups, Bayesian hierarchical models were used to estimate the posterior distributions of parameters such as the mean, standard deviation and median. In the following section describing parameter estimation, the θ symbol will be used as any "parameter."

$$P(\theta|y) = \frac{P(y|\theta)P(\theta)}{P(y)} \tag{2.5}$$

The posterior probability ($P(\theta|y)$) represents the conditional probability of a parameter (θ) given the observed data (y) and the model specifications. The theorem (2.5) incorporates the prior knowledge – $P(\theta)$ –, the likelihood function representing the probability of the data given the parameter – $P(y|\theta)$ – and the marginal likelihood – $P(y)$ – as the probability of the data under the prior belief.

$$P(\theta|y) \propto P(\theta)P(y|\theta) \tag{2.6}$$

This can be simplified by dropping $P(y)$ – as shown in (2.6) – where the posterior distribution is proportional to the product of the prior and likelihood. Every parameter in a model will be estimated by this approach using the Hamiltonian Monte Carlo method implemented in `Stan` (Carpenter et al., 2015). To account for possible interactions between coefficients, they were estimated via a covariance matrix (Σ) implemented as Cholesky factorisation $\Sigma = LL^T$ where L is the positive definite lower triangular matrix.

Continuous data with positive outcomes was modelled using a log-normal or gamma error distribution, whereas unbounded data was estimated using the normal error distribution. For the $firing\ frequency$, the number of spikes per second were estimated directly using the negative binomial distribution. The probability of connections was estimated using a beta distribution for continuous probabilities.

$$Odds_p = \frac{p}{1-p} \tag{2.7}$$

$$LOR_{p_1,p_2} = \log \frac{Odds_{p_1}}{Odds_{p_1}} \tag{2.8}$$

$$ROPE = \pi/\sqrt{3} \cdot 0.1 \tag{2.9}$$

For all of the estimated parameters, 95% of the highest density intervals (HDI) were computed as credible intervals and compared to zero or, in case of the log odds ratio (LOR) (2.8), to the region of practical equivalence (ROPE – Kruschke (2015)) (2.9). In this study, I used HDI to compare groups and estimate differences between groups. Plots with population values show the median outcome with credible intervals (HDIs) covering 80%, 90% and 95% of the data. In the text, the median with 95% HDI is reported. All models were assessed for stability and validity with leave-one-out cross-validation using Pareto-smoothed importance sampling (Vehtari et al., 2017; Gabry et al., 2019).

I estimated the parameters of measurements using Bayesian hierarchical models (Gelman, 2006) to account for nested structures which generally occur in such an experimental design. It is crucial to account for variability between subjects or recording sites to avoid inflating type I errors i.e. false positives (Aarts et al., 2014). Two extreme situations can usually occur: *complete pooling* where, for example, all measurements are considered coming from one source – even though that might not be the case – and *no pooling* which assumes that every subject generates its own measurement and is completely isolated from other subjects (Gelman, 2006). However, this is hardly true for most experiments since cells which are recorded in one region might show correlated properties given that the expression of ChR2 can differ, measurements from one animal might be different to measurements from another animal. Hence, dependencies can be considered and accounted for and

partial pooling can be used where all lower levels originate from an upper level. Such a model leads to estimates being closer to the *pooled* model compared to the *no pooling* approach, but improves predictions for subject levels (Katahira, 2016). This weighting to an overall estimate is referred to as *shrinkage*.

In our *in-vivo* case, power measurements from the lowest level (single trial) will inform power estimates for the next level (session). This will in turn contribute to estimates for the animal and inform in the end estimates of our population parameter representing the measurement of interest – power. The "Bayesian" advantage is that prior information can be included to exclude impossible outcomes. Since we know that an amplifier will limit our maximum measurements and that previous recordings inform our knowledge of what magnitude to expect, we can incorporate such information to increase accuracy of estimates. Finally, estimates will be reported as a whole distribution allowing for quantification of uncertainty. For further review see (Schoot et al., 2021).

In the case of the present study, estimates should be understood as a summary and description of the outcomes rather than a binary decision between *"significant"* and *"not significant"*. Quantified uncertainty allows the reader to decide for themselves whether a reported effect is relevant. Therefore, I have decided to report absolute differences, ratios or log odds ratios with the associated uncertainty/certainty given the data. For most readers, this might take time to get used to, but it can be easier to interpret and less abstract, thus allowing the reader to see the data properly.

2.8.1 Cell property analysis

For cell properties, linear models were constructed by estimating the distribution parameters (the mean μ, standard deviation σ, shape α, rate β etc.) with appropriate link functions.

$$\nu_k = \beta_k + \beta_{k,s} + \beta_{k,ct} + \beta_{k,a} + \beta_{k,m} \tag{2.10}$$

The linear predictor – ν – can be calculated for a given parameter as the sum of β_k – the parameter before applying the link function – and the corresponding coefficients where s refers to the experimental setup, ct the cell type, a the animal and m the

mouse line.

$$\begin{aligned} \mu_k &= \nu_k \\ Normal(\mu_k, \sigma_k) & \end{aligned} \tag{2.11}$$

For models using the normal distribution – $Normal(\mu, \sigma)$ – the identity link was used (2.11). The normal error distribution was used for V_m, $AP-heigth$, $threshold$, AHP and the $mAHP$.

$$\begin{aligned} \ln \mu_k &= \nu_k \\ \beta_k &= \frac{\alpha_k}{\mu_k} \\ Gamma(\alpha_k, \beta_k) & \\ \mu &= \frac{\alpha}{\beta} \\ \sigma &= \sqrt{\frac{\alpha}{\beta^2}} \end{aligned} \tag{2.12}$$

Models with positive continuous outcomes were implemented as gamma distribution – $Gamma(\alpha, \beta)$ – using a log link function (2.12), where α represents the shape parameter and β the rate. This distribution was used to estimate the *positive*, and the *negative* – $-Gamma(\alpha_{neg.Slope}, \beta_{neg.Slope})$ – *slope*, the *latency*, $FWHM$, R_{in}, *rheobase*, *gain*, C_m and the *slope ratio*.

$$\begin{aligned} \ln \mu_k &= \nu_k \\ LogNormal(\mu_k, \sigma_k) & \end{aligned} \tag{2.13}$$

For models implemented as log-normal distribution – $Lognormal(\mu, \sigma)$ – an identity link function was used (2.13). Note that in a log-normal implementation, the mean of the distribution is calculated as $e^{\mu+\frac{\sigma^2}{2}}$, the median as e^{μ} and the standard deviation as $e^{\mu+\frac{1}{2}\sigma^2}\sqrt{e^{\sigma^2}-1}$. This distribution was applied to $ISIs$ and the spike *adaptation* ($\mu_{adaptation} = \mu_{ISI_{9/10}} - \mu_{ISI_{1/2}}$ where μ is on the log scale).

$$
\begin{aligned}
logit(\mu_k) &= \nu_k \\
\alpha_k &= \mu\phi \\
\beta_k &= (1-\mu)\phi \\
Beta(\alpha_k, \beta_k)
\end{aligned} \tag{2.14}
$$

The *sag ratio* was implemented as beta distribution – $beta(\alpha, \beta)$ – using a logit link function (2.14).

$$
\begin{aligned}
\ln \mu_k &= \nu_k \\
NegBinomial(\mu_k, \phi_k) & \\
\sigma &= \sqrt{\mu + \frac{\mu^2}{\phi}}
\end{aligned} \tag{2.15}
$$

As previously mentioned, the $firing\ frequency$ was estimated by directly estimating the action potential count in a 1 s window. A modified negative binomial – $NegBinomial(\mu, \phi)$ – with a log link (2.15) was used, which is parameterised so that the mean is μ and the standard deviation as shown in (2.15).

All dispersion parameters – such as σ, ϕ, or the shape parameter α in the gamma distribution – were estimated using a log link so that $ln\sigma = \nu_{disp}$, $ln\phi = \nu_{disp}$ or $ln\alpha = \nu_{disp}$. The exception is the log normal distribution where σ is required to be on the log-scale and therefore requires the use of an identity link without transformation.

2.8.2 Connectivity analysis

For connectivity, the probability of connections was estimated with a beta distribution as shown in (2.14) with $\nu_{connection} = X\beta_0 + X\beta_s + X\beta_a + X\beta_m$ where X represents the cell type model matrix.

2.8.3 *In-vivo* power density

I estimated the power density over different stimulation frequencies by taking the wavelet transform $|W(a,b)|$, applying a frequency correction ($|W(a,b)|_f \cdot f$) and computing the density for any given time point of the transform. The average density for each block (pre-stimulation, stimulation, post-stimulation) was then calculated at the stimulation frequency.

$$\ln \mu_{PowerDensity} = \beta_{max} - \beta_{max} e^{(-\beta_{Slope} StimulationFrequency)} \tag{2.16}$$

Using an asymptotic regression with β_{max} as maximum ceiling for ν and a floor of 0. The dependency of stimulation frequency was incorporated as β_{slope}. As explained in (2.10), β parameters were estimated as a hierarchical structure with *animal* (with nested *session* and *trial*), θ *burst stimulation*,*recording site* and the *stimulation site* as levels.

2.8.4 *In-vivo* phase lock

To estimate entrainment, ρ was estimated for every time point and frequency of the wavelet transform.

$$\theta(f,t) = atan2(\Im(W(a,b)), \Re(W(a,b))) \tag{2.17}$$

$$\rho_{f,t} = \sqrt{\left(\frac{1}{trial_N} \sum_{n=1}^{trial_N} sin\theta(f,t)\right)^2 + \left(\frac{1}{trial_N} \sum_{n=1}^{trial_N} cos\theta(f,t)\right)^2} \tag{2.18}$$

The imaginary parts and real parts of the wavelet transform were extracted to calculate the phase at any given point (2.17) to subsequently calculate ρ as the strength of phase lock over all trials in a session (2.18). For further analysis, the log odds ratio between ρ and $\rho_{random} = \frac{1}{\sqrt{trial_N}}$ was used.

$$\mu_{LOR} = \beta_{max} - (\beta_{max} - \beta_{min}) e^{(-\beta_{Slope} StimulationFrequency)} \tag{2.19}$$

Similarly to the previous asymptotic regression for the power density, LOR was estimated as described in (2.19) where, in addition to the maximum and the slope, a minimum was estimated (β_{min}). The LOR could then be compared to the ROPE.

3

Results

3.1 *In-vitro*

3.1.1 Cell characterisation

As we described in a previous study, cells in the PaS can be split into three major clusters which mainly correspond to a split into GABAergic and glutamatergic cells (Sammons et al., 2019). This was determined by recording cells in VGAT$^+$ (Vesicular Inhibitory Amino Acid Transporter) mice where we described electrophysiological properties of pyramidal cells, interneurons, and fast spiking interneurons. I sought out to collect a wide range of parameters and put them into context with previously published cell clusters. To get a good estimate for these parameters, it was required to get a large sample of cells. Hence, we recorded 214 neurons in the PaS (204 published in Sammons et al. (2019) and 10 additional cells) and quantified a total of 19 cell parameters, giving a rich overview of electrophysiological features. To determine optimal separation patterns between the 3 major clusters, I integrated the measured properties in the same hierarchical clustering approach as reported in Sammons et al. (2019). Briefly, the cell parameters were firstly scaled and centred by subtracting the mean and dividing by the standard deviation for each parameter. This was then followed by calculating the euclidean distance matrix which was used to cluster the cells based on Ward's method (Ward, 1963). As demonstrated by Sammons et al. (2019), by using this approach cells, in the PaS can be divided into 3 clusters which represent putative fast spiking interneurons (FS), a heterogeneous cluster with mainly regular interneurons (IN) and pyramidal cells,

which are often WFS1$^+$. Since there is no available information for parasubicular layer I interneurons, I was additionally interested in differentiating between layer I interneurons and other cells. Therefore, I further stratified the cells based on the location determined on confocal images or differential interference images at the recording setup. We tried to represent classes other than pyramidal cells equally well, which meant a targeted approach was necessary to increase the samples of the IN, FS and IN-L1 clusters. Therefore, we visually identified non-pyramidal cells based on the soma shape, but also according to the orientation and structure of the dendrites. Cell properties were measured in whole-cell current-clamp configuration using hyper- and depolarisation current steps (step size of $40pA$) (Figure 6A). Only 1 layer I cell was originally classified as belonging to the pyramidal cell cluster and 34 were determined to be in the IN cluster. This classification underlines the notion that the IN cluster is dominated by interneurons in the PaS. A substantial amount – 54% of the cells – were putative pyramidal cells (115), whereas a fraction were classified as interneurons (44 fast spiking basket cell-like interneurons (FS); 20 layer II interneurons (IN); 35 layer I interneurons (IN-L1)).

Here, we reported a description of electrophysiological properties of often overlooked layer I cells in the PaS for the first time. Overall, cells showed a similar resting potential (DS: $-69.75\ mV$ $[-80.45; -59.08]$, FS: $-69.92\ mV$ $[-79.91; -59.71]$, IN: $-69.55\ mV$ $[-79.69; -58.73]$, IN-L1: $-69.73\ mV$ $[-80.47; -58.82]$) with differences in the input resistance (R_{in}) showing lower resistance in FS cells and very high R_{in} measured in IN-L1 and IN cells (DS: 96.84 $M\Omega$ $[41.37; 169.98]$, FS: 55.78 $M\Omega$ $[23.49; 95.01]$, IN: 142.73 $M\Omega$ $[51.79; 257.35]$, IN-L1: 138.09 $M\Omega$ $[48.67; 253.78]$) compared to others. The membrane capacitance (C_m), a proxy for different properties of the cell such as size or conductance, was very low in IN-L1 cells which usually had visually a small soma and shorter dendrites than pyramidal cells or FS basket-like cells (DS: 134.62 pF $[51.12; 242.94]$, FS: 101.20 pF $[28.45; 196.49]$, IN: 71.35 pF $[19.29; 147.84]$, IN-L1: 50.24 pF $[10.83; 105.42]$). The strongest mean difference was measured between DS and IN-L1 cells (FS-DS: $-34.82\ pF$ $[-50.32; -18.20]$, IN-DS: $-65.19\ pF$ $[-83.19; -46.69]$, IN-FS: $-30.34\ pF$ $[-50.06; -9.46]$, IN-L1-DS: $-86.90\ pF$ $[-100.88; -72.64]$, IN-L1-FS: $-52.18\ pF$ $[-68.41; -35.97]$, IN-L1-IN: $-21.73\ pF$ $[-41.05; -3.67]$). This low C_m corresponded to the R_{in} except that,

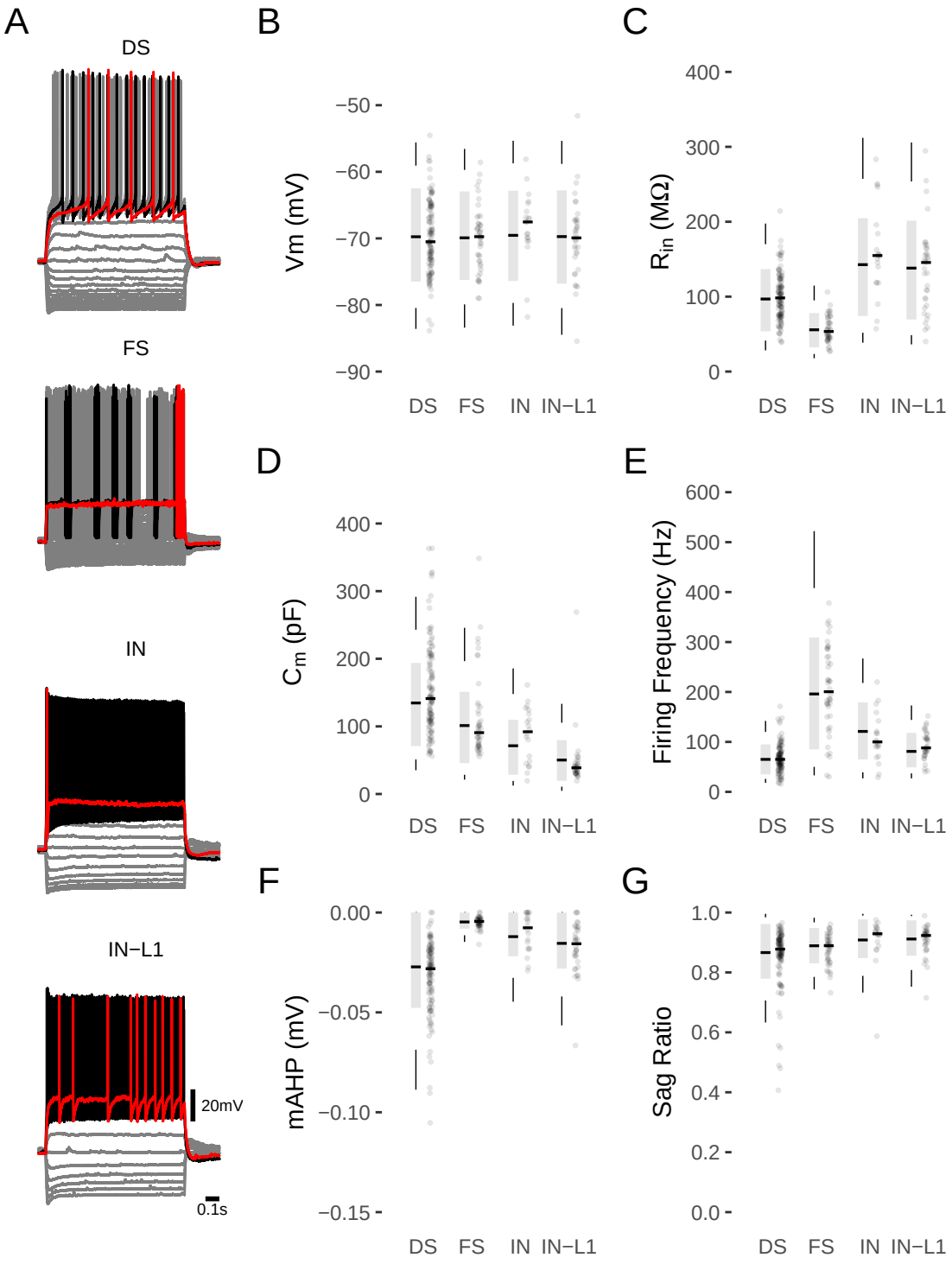

Figure 6: Cell characterisation. *Characterisation of cells in the PaS after current step injection (A) with the first spike coloured in red and the following in black. Other current injections are in grey. Scale bars reflect* 0.1 *s and* 20 *mV of amplitude. B-G show the measured cell properties of the* 214 *cells as point clouds with its median as line and the bar plot represents the population estimates given the cell type. For each boxplot the black horizontal line in the box indicates the median, the grey box reflects the* 80%*, the beginning of the whisker the* 90% *and the end of the whisker the* 95% *credible intervals.*

even compared to cells from the IN cluster, IN-L1 cells had a lower C_m (IN-L1-IN: $-21.73\ pF$ $[-41.05; -3.67]$). However, the combination of C_m and R_{in} did not result in the highest $firing\ frequency$ for IN-L1 cells (DS: 65.00 Hz $[26.00; 120.00]$, FS: 196.00 Hz $[50.00; 408.00]$, IN: 121.00 Hz $[39.00; 218.00]$, IN-L1: 81.00 Hz $[37.00; 144.00]$). In fact, the cell cluster we termed fast spiking interneurons – FS – showed the largest mean difference in $firing\ frequency$ (Figure 6E) compared to all other clusters and could reach frequencies 2-3 times higher than the other groups (FS-DS: 141.08 Hz $[105.75; 178.08]$, FS-IN: 84.32 Hz $[126.68; 48.18]$, FS-IN-L1: 124.80 Hz $[161.00; 89.50]$). In summary, all cells had a higher $firing\ frequency$ compared to putative glutamatergic pyramids (FS-DS: 141.08 Hz $[105.75; 178.08]$, IN-DS: 55.94 Hz $[32.92; 82.11]$, IN-L1-DS: 16.04 Hz $[5.03; 28.06]$). A similar relationship was observed when analysing the *sag ratio* (Figure 6G). The *sag ratio* is a measure of rebound afterhyperpolarisation (DS: 0.87 $[0.71; 0.98]$, FS: 0.89 $[0.79; 0.97]$, IN: 0.91 $[0.79; 0.99]$, IN-L1: 0.91 $[0.81; 0.99]$) and was higher in all interneuron classes compared to the DS cluster (FS-DS: 0.03 $[0.01; 0.05]$, IN-DS: 0.04 $[0.02; 0.07]$, IN-L1-DS: 0.05 $[0.03; 0.07]$). This finding suggests that rebounds after hyperpolarisations, known to be mediated by I_h, are more pronounced in glutamatergic cells than in interneurons. In contrast, we could not detect differences in the medium afterhyperpolarisation ($mAHP$) – the corresponding response after a finished longer depolarisation step (DS: $-0.03\ mV$ $[-0.07; 0.00]$, FS: $0.00\ mV$ $[-0.01; 0.00]$, IN: $-0.01\ mV$ $[-0.03; 0.00]$, IN-L1: $-0.02\ mV$ $[-0.04; 0.00]$).

To assess the excitability of cells, the *rheobase* – the current at which the first spike is triggered – (Figure 7H) was measured and quantified. DS cells and IN-L1 cells showed the lowest *rheobase* indicating a high excitability when depolarised (DS: 118.96 pA $[29.77; 243.87]$, FS: 384.96 pA $[98.42; 762.93]$, IN: 128.97 pA $[16.68; 309.81]$, IN-L1: 129.79 pA $[19.34; 308.75]$). This excitability was mainly achieved due to the high R_{in} and not a lower *threshold* in DS and IN-L1 cells. On the contrary, a lower *threshold* was measured in FS cells opposed to DS and IN-L1 cells (Figure 7B) underlining the potential importance of the R_{in} as the main mechanism for excitability in the two classes (DS: $-34.82\ mV$ $[-41.68; -28.29]$, FS: $-36.95\ mV$ $[-49.35; -25.75]$, IN: $-33.97\ mV$ $[-45.16; -22.21]$, IN-L1: $-33.20\ mV$ $[-46.45; -20.53]$). A neuron can have different stages of excitation which can be a re-

sult of fast spike initiation; high $firing\ frequency$ or sustained firing (see *adaptation* in Table 1). Considering the low *rheobase* of DS neurons in terms of spike initiation, DS cells were overall less excitable than the interneurons when looking at spiking output over different current injections. To quantify this overall excitability, I computed the *gain* for all the neurons (Figure 7I: DS: 0.29 $\frac{Spikes}{pA}$ $[0.06; 0.60]$, FS: 0.83 $\frac{Spikes}{pA}$ $[0.18; 1.79]$, IN: 0.56 $\frac{Spikes}{pA}$ $[0.13; 1.26]$, IN-L1: 0.58 $\frac{Spikes}{pA}$ $[0.12; 1.26]$). The *gain* represents the increase in spiking relative to the input current ($Spikes/pA$) and was substantially higher in interneurons compared to other cell types, with highest *gain* values in FS cells (FS-DS: 0.58 $\frac{Spikes}{pA}$ $[0.45; 0.70]$, IN-DS: 0.30 $\frac{Spikes}{pA}$ $[0.18; 0.43]$, IN-L1-DS: 0.32 $\frac{Spikes}{pA}$ $[0.22; 0.43]$, IN-FS: -0.28 $\frac{Spikes}{pA}$ $[-0.45; -0.10]$, IN-L1-FS: -0.26 $\frac{Spikes}{pA}$ $[-0.41; -0.10]$). This finding translates to a more efficient input-output relationship in interneurons compared to DS cells, allowing them to increase spiking activity quickly upon depolarisation. In addition to the initiation of spiking and the *gain*, neurons were stimulated as previously mentioned with a higher current step to induce the maximum $firing\ frequency$. Another different measure of excitability is the latency of a spike (Figure 7D) measured at the current injection step with the first occurrence of action potentials. This parameter refers to the time it takes for the first spike after the onset of current injection and reflects how instantaneous or filtered a potential input to a cell is relayed further downstream. Spike *latency* was, on average lower in all interneurons compared to DS cells (FS-DS: $-0.06\ s$ $[-0.08; -0.03]$, IN-DS: $-0.06\ s$ $[-0.09; -0.02]$, IN-L1-DS: $-0.06\ s$ $[-0.09; -0.03]$), indicating a fast response upon depolarisation. However, all cell types showed a wide range of possible latencies when spiking. Therefore, we termed the putative pyramidal cell cluster "delayed spiking cells" or "DS." This behaviour suggests an interesting property of DS cells whereby they require more time to integrate input current until the *threshold* is reached. As previously mentioned, the slower integration (τ) is further supported as a membrane property by a higher C_m in DS cells (FS-DS: $-34.82\ pF$ $[-50.32; -18.20]$, IN-DS: $-65.19\ pF$ $[-83.19; -46.69]$, IN-L1-DS: $-86.90\ pF$ $[-100.88; -72.64]$) where $\tau_m = R_m \cdot C_m$.

To address possible implications for cell outputs which can be due to action potential shape, I quantified the parameters describing the kinetics of APs (Figure 7A). Several parameters were included in the analysis such as the $FWHM$ (Figure 7F),

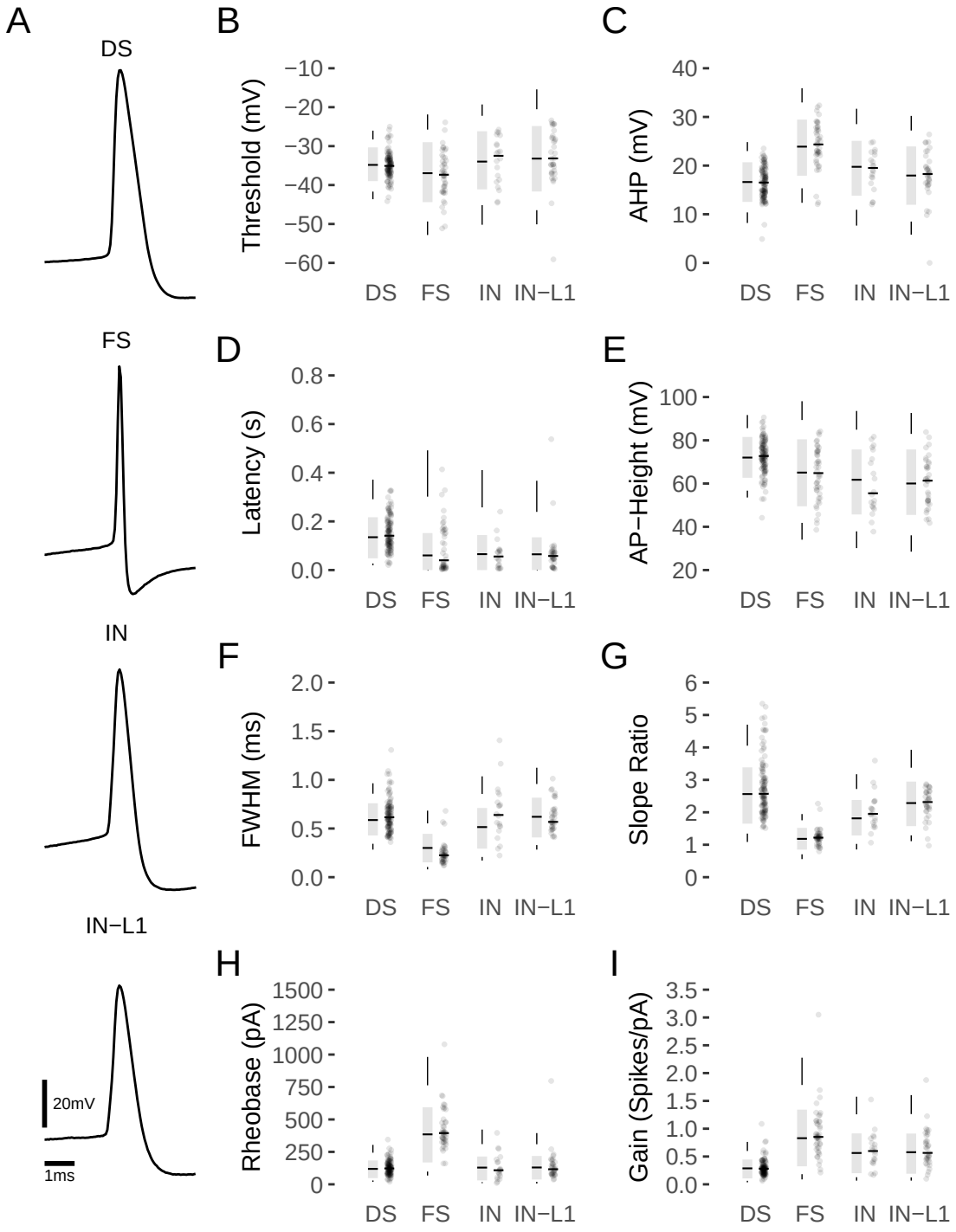

Figure 7: Action potential properties. *(A) Representative examples of action potentials of the four cell clusters with their properties (B-I). The point clouds in B-I represent measurements of the cells and the corresponding boxplots reflect the estimated cell type population properties. For each boxplot, the black horizontal line in the box indicate the median, the grey box reflects the* 80% *, the beginning of the whisker the* 90% *and the end of the whisker the* 95% *credible intervals.*

the rising and falling component of the action potential (*positive* and *negative slope* – see Table 1), and the resulting *sloperatio* (Figure 7G). These kinetic measures often showed a wider and slower action potential in DS cells opposed to faster interneuron kinetics ($FWHM$ – DS: 0.59 ms [0.34; 0.86], FS: 0.30 ms [0.10; 0.55], IN: 0.51 ms [0.21; 0.86], IN-L1: 0.62 ms [0.33; 0.96]; sag ratio – DS: 0.87 [0.71; 0.98], FS: 0.89 [0.79; 0.97], IN: 0.91 [0.79; 0.99], IN-L1: 0.91 [0.81; 0.99]). Other parameters of the action potential are the *action potential height* (DS: 72.00 mV [56.72; 85.61], FS: 65.06 mV [41.82; 89.37], IN: 61.75 mV [37.89; 84.89], IN-L1: 60.02 mV [36.06; 82.95]) which showed that on average interneurons had smaller APs than DS cells (FS-DS: -6.93 mV [$-10.72; -3.11$], IN-DS: -10.24 mV [$-15.93; -4.85$], IN-L1-DS: -12.12 mV [$-15.87; -8.18$], IN-FS: -3.31 mV [$-9.56; 2.83$], IN-L1-FS: -5.16 mV [$-10.35; -0.24$], IN-L1-IN: -1.80 mV [$-7.90; 4.14$]) and IN and IN-L1 cells had the smallest APs (Figure 7E). On the other hand, compared to DS or IN-L1 cells, FS and IN cells had a larger afterhyperpolarisation (AHP) directly following the action potential (FS-DS: 7.23 mV [5.72; 8.69], IN-DS: 3.11 mV [1.05; 5.17], IN-FS: -4.10 mV [$-6.53; -1.85$], IN-L1-FS: -5.87 mV [$-7.99; -3.92$]). FS cells showed an especially prominent AHP after the action potential (Figure 7C and Table 2). In contrast, DS cells and IN-L1 displayed minimal hyperpolarising overshoot. A full list of parameter estimates with all performed comparison can be found in Table 1 of the appendix (Table 2).

3.1.2 Cell connectivity

3.1.2.1 PV$^+$ projections to the PaS

To investigate whether GABAergic PV$^+$ MS cells project to the PaS and which targets they have, we recorded cells in whole-cell patch-clamp configuration *in-vitro* in PV-Cre. I injected Cre mice in the MS with a Cre-dependent AAV to drive channelrhodopsin expression. Hence, GABAergic PV$^+$ cells in the MS expressed channelrhodopsin and the yellow fluorescent protein (YFP), so that fibres could be found in the PaS (Figure 11A) after at least 4 weeks of expression. After the cell characterisation, we illuminated the septal terminals in the PaS using blue light and recorded inhibitory postsynaptic currents and potentials at different holding potentials (-50 mV, resting potential (Vm), -80 mV Figure 8). We stimulated

the cells over several trials (> 10) and averaged the signal to improve signal-to-noise for detection. In total, we tested 78 cells and received 23 responses, all of which were hyperpolarising inputs except for one input onto a DS cell. This exception showed an EPSP and could be abolished by NBQX. The 10 *ms* stimulation reliably resulted in a fast hyperpolarisation, which could be reversed when changing the holding potential (Figure 9A and B).

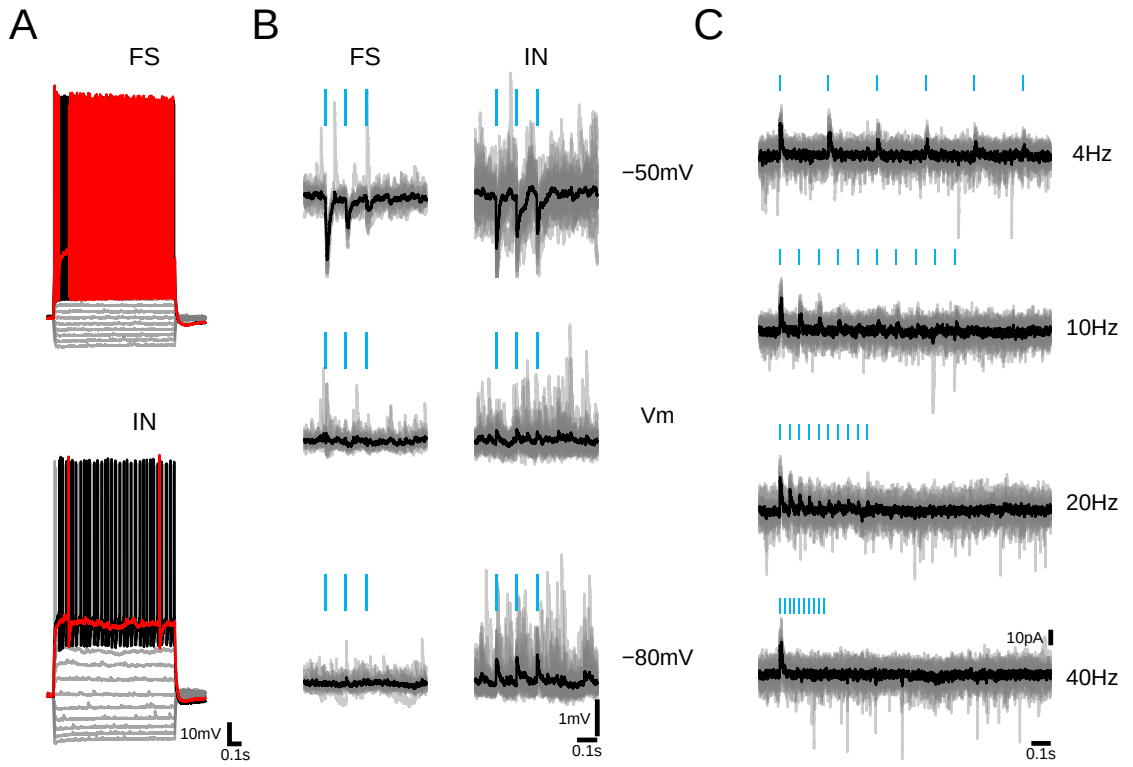

Figure 8: Light induced synaptic inputs by activation of PV$^+$ fibres. *Panel A shows a FS and an IN cell receiving GABAergic septal inputs. Panel B inhibitory postsynaptic potentials at different holding potentials during 10Hz stimulation elicited with 10ms light pulses. Blue lines indicate the timing and length of stimulation. Panel C shows a FS cell in voltage-clamp configuration held at -45 mV during 4 Hz, 10 Hz, 20 Hz, and 40 Hz stimulation with 10 ms light pulses.*

An important feature of synaptic connections is the strength of the connection which can be quantified as amplitude. A large negative deflection will likely be able to inhibit a cell when depolarised. To estimate the reversal potential and the amplitudes of synaptic inputs, I used a Bayesian hierarchical linear model. These models have the advantage that accounting for nested structures in the data (cells, animal, experimental setup) is simple and will result in more unbiased population parameter estimates. I reparameterised the regular linear regression ($y = m \cdot x + n$) to directly estimate the reversal potential ($y = m \cdot x - slope \cdot V_{rev}$) and added an informative prior

(some restricting soft bounds) with a mean of $-68\ mV$ taken from Gonzalez-Sulser et al. (2014) and 3 standard deviations.

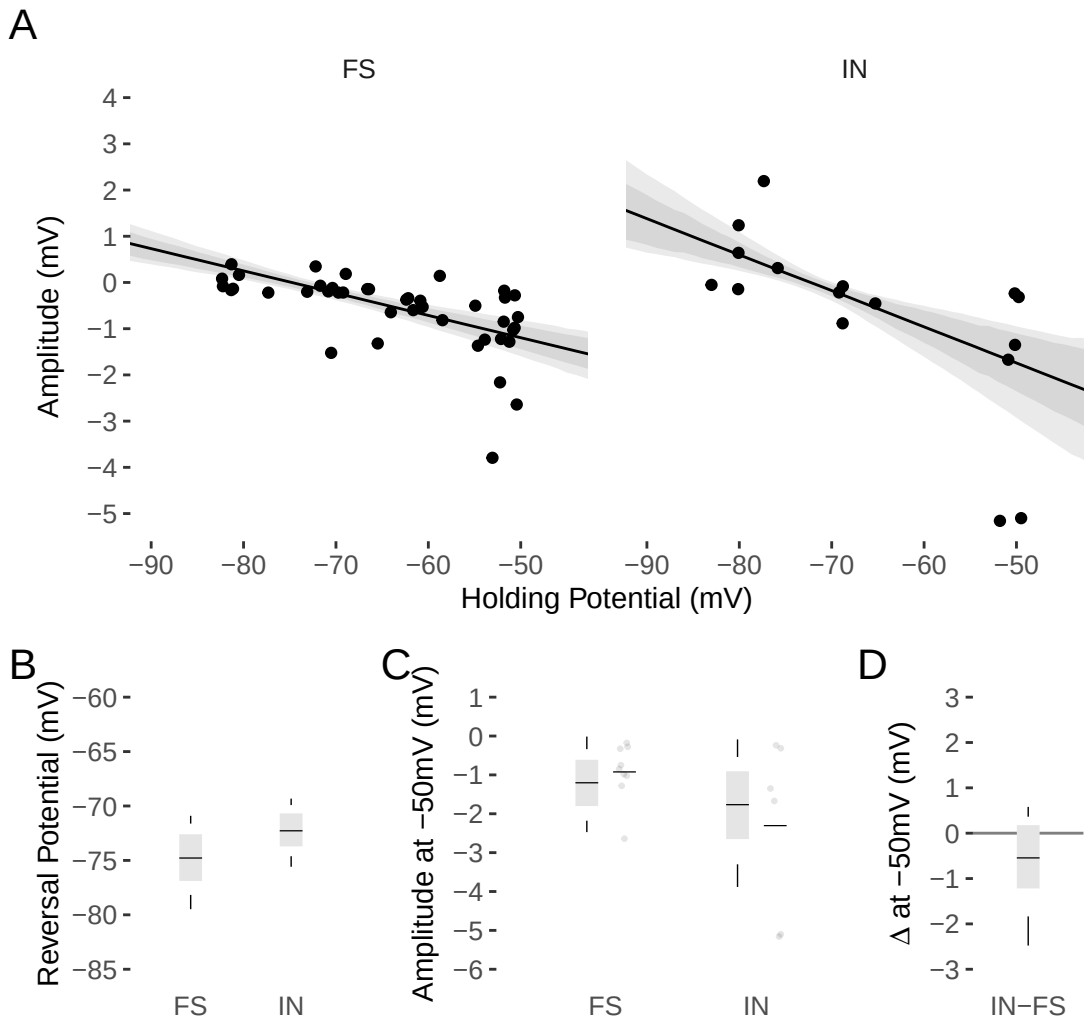

Figure 9: Reversal input amplitude. *Amplitudes of GABAergic medial septal inputs to FS and IN cells of the PaS given a holding potential of a cell (A). Single dots represent a single input and the line is the median estimated population mean conditional on the cell type. The grey shaded area shows the* 80% *and* 95% *highest density interval. (B) The estimated reversal potential for FS and IN cells. (C) A subset of inputs where the baseline was between* $-52\ mV$ *and* $-48\ mV$ *is shown next to the estimated input amplitude given the baseline is* $-50\ mV$*. The line in the point cloud represents the mean of the subset. (D) A comparison of the FS and IN responses reveal a tendency that IN inputs are larger but the zero-line is contained in the* 80% *credible interval.*

Since a total of only 5 interneurons from layer I and II were connected, I pooled them for further analysis. A comparison of the reversal potential showed that there was no detectable difference (FS: $-74.78\ mV$ $[-78.17; -71.62]$, IN: $-72.28\ mV$ $[-74.61; -69.92]$) between FS and IN/IN-L1 clusters and a calculation of the slope difference revealed that, even though there might be a trend for IN cells to receive

stronger inputs at any given holding potential, it did not significantly differ (IN-FS: $-0.03\ mV_{amp}/mV_{hold}$ $[-0.09; 0.01]$). This was underlined by only extracting the posterior distribution for $-50\ mV$ holding potential to investigate differences in strongly depolarised cells (Figure 9C and D). As seen in D, the difference in mean amplitude between cell types $-0.54\ mV$ $[-1.83; 0.36]$ again showed a trend for IN/IN-L1 cells to have slightly larger IPSPs. Considering that R_{in} and other passive membrane properties differ between the cell types (Table 2), it is possible that they could contribute to the variability between FS and IN/IN-L1 clusters.

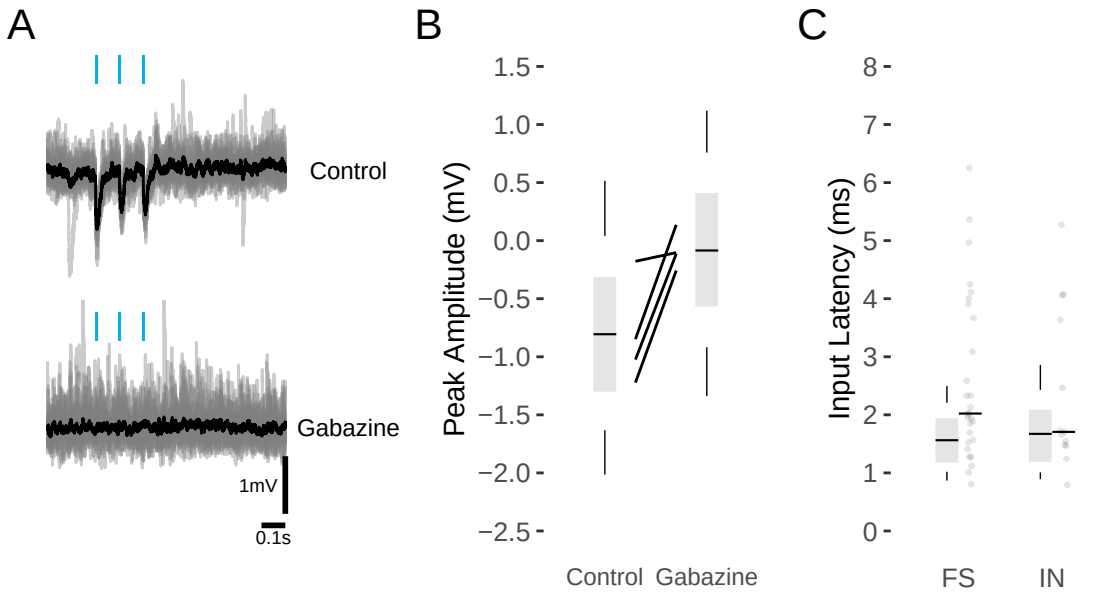

Figure 10: Gabazine washin and input latency. *(A) Traces of light induced IPSPs (top) show that after washin of Gabazine IPSPs are abolished (bottom). (B) Gabazine reduces amplitude of IPSPs to noise level (B). (C) The estimated input latencies (for instantaneous LED light stimulation) with the raw data points for the inputs (FS:* 55/16*; IN:* 24/5 *– Inputs/Cells).*

To establish the identity of GABAergic inputs, we washed in 1 μM Gabazine, a $GABA_A$ blocker in 4 recordings of FS cells. Indeed, we could show that the application of the drug abolished inputs (Figure 10A) and reduced the mean amplitude from $-0.81\ mV$ $[-1.17; -0.44]$ in the control to noise level (Gabazine: $-0.09\ mV$ $[-0.45; 0.30]$) as shown in Figure 10B. This indicates that septal PV^+ projections which elicit IPSPs are mediated by $GABA_A$-receptor activation. To check whether the responses were directly associated with the stimulation, I analysed the input latency. We did not observe slow responses indicating $GABA_B$ mediated hyperpolarisations. However, cells in the PaS as in many other areas have $GABA_B$ re-

ceptors and will hyperpolarise when washing in the $GABA_B$ agonist baclofen (data not shown). For analysis of the latency (Figure 10C), I performed a linear hierarchical model with log-normal error distribution which is often observed for timing events. The hierarchical structure allowed me to account for different aspects of the experimental design such as cell types and LED or shutter stimulation. The LED, based on a pure electric activation, will give an instantaneous maximum light power while the shutter will take longer to open completely. This introduces some artefacts which can be accounted for. I chose inputs measured in current-clamp with an amplitude of more than 0.2 mV and 3 times the baseline standard deviation to estimate the cell type specific onsets. As the *prior* for the mean I relied on data from Gonzalez-Sulser et al. (2014) where in the MEC a mean latency of 1.54 ms was observed. On top of the prior latency, I added a larger error (σ) to account for a large range of values (roughly $0 - 30$ ms). The results of this analysis show that FS cells and IN/IN-L1 cells show very similar latencies (FS: 1.56 ms $[1.02; 2.21]$, IN: 1.67 ms $[1.01; 2.43]$), but also revealed that a physical shutter can indeed more than double the onset times, showing the importance of a thorough analysis (FS: 3.92 ms $[2.26; 5.80]$, IN: 4.16 ms $[2.28; 6.65]$). The analysis encouragingly captured the variance and helped to determine that inputs are likely direct.

To understand the implication of the inhibition for the PaS as a network, I quantified the proportions of cells which receive inputs and calculated the connectivity as a fraction given the cell type. For the quantification of connectivity, I used a logistic regression with hierarchical structure which allowed me to estimate an overall septal connectivity to then further stratify and differentiate between PV^+ and $ChAT^+$ projections. Additionally, possible errors due to the nested structure of the experiments (cells, animal, and experimental setup) could be accounted for. A Bayesian approach is a great way to quantify binary data outcomes and was used to some degree in Desikan et al. (2018), where a *beta* distribution was used to estimate credible intervals for connectivity. In our case, we used the continuous *beta* distribution as well. However, I was also able to perform more calculations on the posterior connectivity distribution since I modelled the experiment with its experimental structure. As weakly informative *priors* for the mean connectivity, I used PV^+ connections data from Fuchs et al. (2016) and Gonzalez-Sulser et al. (2014)

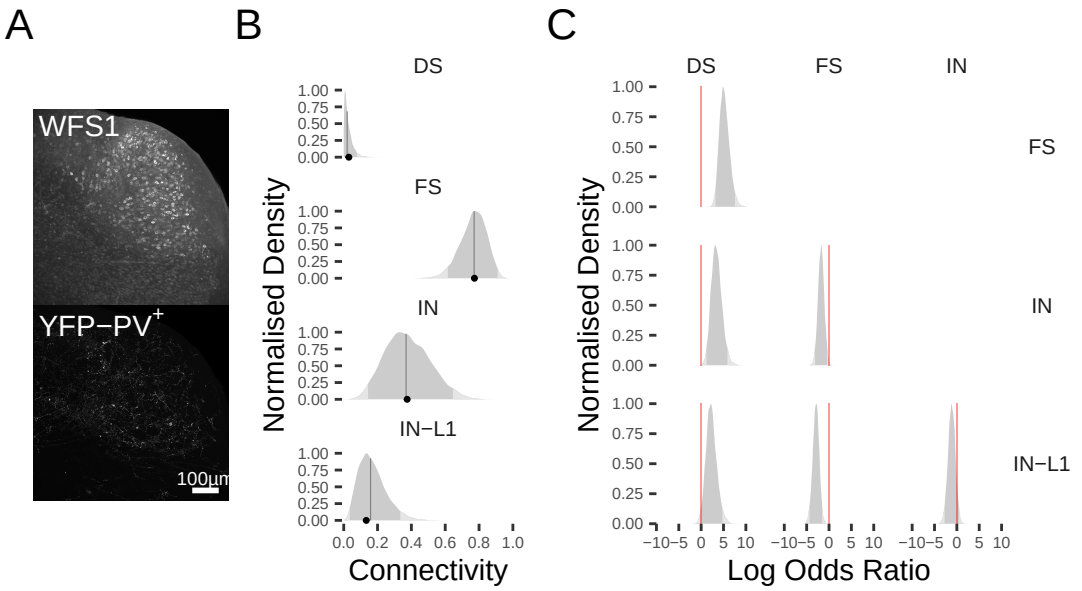

Figure 11: Connectivity of PV$^+$ MS cells to PaS. *(A) A horizontal section stained for WFS1 (top) and against YFP (bottom) which is expressed by PV$^+$ fibres coming from the MS. (B) The estimated connectivity as posterior distribution is shown in grey for different cell types (from top to bottom: DS, FS, IN IN-L1). The dark grey area represents the 95% credible interval of the posterior distribution and the light grey show the remaining tails. The vertical lines show the median of the posterior and the black dots at the bottom of each distribution the raw frequentist point estimates. (C) Probability distributions can be compared to each other by calculating the log odds ratio for any given comparison. The red line indicates the region of practical equivalence.*

and added wide enough errors to allow the data to inform the analysis. For DS cells only 1 of 33 cells responded to stimulation which could, however, be blocked by NBQX. This translates to a credible interval of 0.02 $[0.00; 0.08]$ (Figure 11B), indicating that there is little evidence in the data to assume a probability higher than 8% as an upper bound. In contrast, a high proportion of FS cells (17 of 22) received GABAergic inputs. They represent, by far, the most likely target of PV$^+$ MS projections to the PaS (0.77 $[0.62; 0.91]$). This high connectivity is in line with previous studies and other areas resulting in disinhibition of the network. Due to a smaller sample size (3 of 8), estimates for IN cells resulted in a wider credible interval with 0.37 $[0.14; 0.64]$. Surprisingly IN-L1 cells, which were previously not reported to receive PV$^+$ inputs from the septum, were inhibited through channelrhodopsin stimulation (2 of 15). This means that IN-L1 received GABAergic inputs in 0.16 $[0.04; 0.33]$ of the cases. To compare the connectivity of each cell type to each other, posterior distributions were used to calculate the log odds ratio (see equation (2.8) for LOR).

The log odds ratio has the advantage of being, firstly, symmetric, and secondly, a simpler interpretation when comparing probabilities, since it can be transformed to the odds ratio (OR) indicating how much more something is likely to happen over another event. Therefore, a LOR of 0 (OR of 1) would mean that both cell types have an equal chance of receiving PV^+ inputs. In Figure 11C, we can see that the strongest difference can be found between FS and DS cells with a LOR of 5.13 $[3.21; 7.55]$, meaning the odds of an FS being connected is almost 200 times higher than for DS cells. The 95% credible interval does not cross 0 nor does it enter the region of practical equivalence (for equation of ROPE see (2.9)) (Kruschke, 2015) as indicated by the red line.

The ROPE indicates which LOR values would likely represent equivalence between the compared groups. Similarly strong was the difference between IN-L1 cells and FS cells (-2.91 $[-4.36; -1.54]$), IN and DS cells (3.37 $[1.20; 5.86]$) and moderately strong between IN and FS cells (-1.76 $[-3.12; -0.44]$). The connection probability for DS to IN-L1 cells was comparable, as was the connection probability for IN to IN-L1 indicated by the credible interval of the LOR crossing the ROPE (Figure 11C). However, this indicates that interneurons are more likely to be inhibited than putative glutamatergic DS cells.

Given that fast $GABA_A$ responses would allow a high time accuracy due to their fast kinetics, PV^+ cells of the septum could be crucial for timed inhibition of PaS cells. To test for this possibility, I depolarised a small subset of cells which received GABAergic inputs so that they were slightly over the spiking threshold, resulting in continuous spiking of the cell (Figure 12A). The cell was inhibited over several trials (Figure 12B) and showed that spikes started reliably at similar times over different trials and fire periodically afterwards until inhibited again (Figure 12B and C). Considering this timing of spikes, we can represent every spike train for each single trial as a wave, where a spike represents the peak of the wave and the middle of the pause the trough. This reparameterisation of a spike train to a sinusoidal wave allows us to calculate the phase at any given time point (t) for every single trial. Since a phase can be represented on a unit circle with $x = \cos\theta$ and $y = \sin\theta$, we can calculate the average vector length ρ for every time point over all the trials for any given point in time (see equation (3.1)).

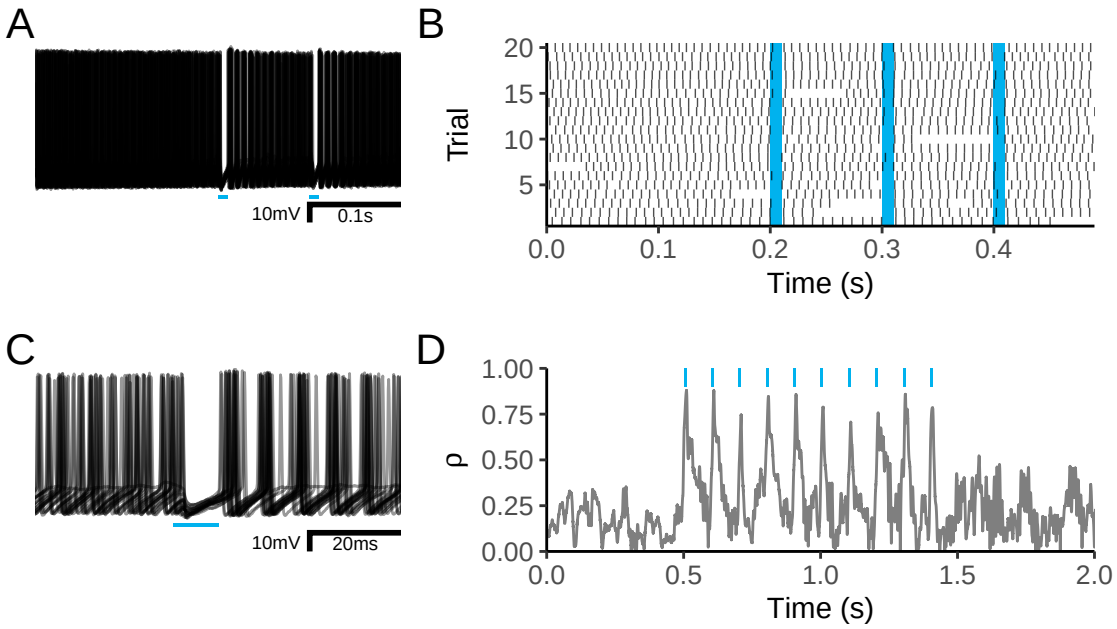

Figure 12: Spike phase reset in-vitro. *A depolarised spiking putative interneuron (A) is inhibited using 10 ms long light pulses at* 10 Hz*. The raster plot (B) shows spike times throughout 20 trials over a time of* 0.5 s*. C ,a closeup of (A), shows complete inhibition of spikes during stimulation times. D shows* ρ *a value for phase locking of spikes. The maximum value of* ρ *is* 1 *assuming perfect phase lock and the chance level* ρ_{random} 0.22*. Blue lines indicate the timing and length of stimulation in A-D.*

$$\rho_t = \sqrt{\left(\frac{1}{trial_N}\sum_{n=1}^{trial_N} sin\theta_t\right)^2 + \left(\frac{1}{trial_N}\sum_{n=1}^{trial_N} cos\theta_t\right)^2} \tag{3.1}$$

A ρ value of 1 indicates a perfect alignment whereas a value of 0 indicates none. In our case, a high value translates to a high alignment in spike timing (Figure 12D) over all the trials. An increase can be observed close to the stimulation onset and is carried on for some time before it is lost and ρ returns to a lower value, close to the expectation of a random distribution ($\rho_{random} = \frac{1}{\sqrt{trial_N}}$), as shown in Figure 12C. Overall, this illustrates that even when a cell is spiking, GABAergic inputs from the MS can be sufficient to inhibit the cell enough to lock firing for a brief time. This observation is crucial for efficient phase locking in an active network.

3.1.2.2 ChAT$^+$ projections to the PaS

The second major group of projections from the MS to other regions comes from ChAT$^+$ MS cells. Since there is no data on cholinergic septal projections to the PaS, we investigated functional connectivity. Similarly to the test of connectivity

in PV-Cre animals, we investigated projections from cholinergic MS cells to the PaS. Cholinergic projections are much more challenging to detect compared to glutamatergic or GABAergic inputs. The reason for this is, firstly, the often found smaller amplitude and, secondly, the heterogeneity of possible membrane responses (Figure 13D).

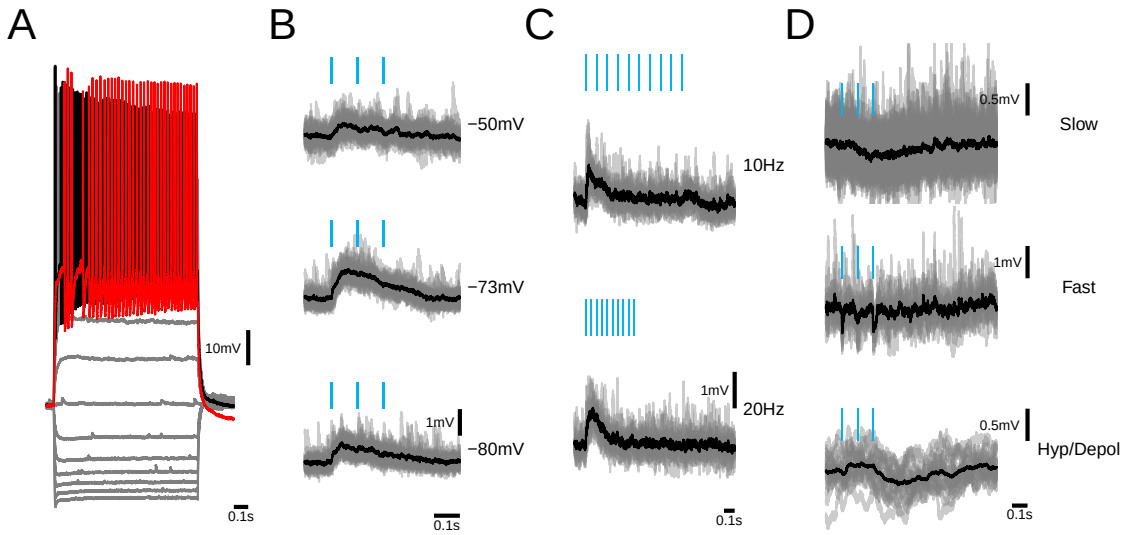

Figure 13: Light induced synaptic inputs by activation of ChAT$^+$ fibres. *(A) The current step characterisation of an IN-L1 cell which receives depolarising inputs with step triggering the first spike in red and the following step in black. Additional steps are kept in grey. (B) The inputs are slow and do not sustain continuous stimulation at higher frequencies (C). (D) Other types of responses can be observed in different cells: top – a slow hyperpolarisation; middle – a fast hyperpolarisation reminiscent of GABAergic inputs; bottom – a combination of depolarisation and slow hyperpolarisation. Light pulses are indicated by blue bars.*

GABAergic responses could also be observed in PaS cells (1 in 22 FS, 1 in 12 IN, and 1 in 82 DS) by stimulating ChAT$^+$ fibres which supports previous evidence by Desikan et al. (2018) that the medial septal ChAT$^+$ fibres can co-release GABA. However, compared to PV$^+$ projections, GABAergic inputs account only for a small proportion of the projection effect (3 in 136 cells). We found a total of 24 in 136 cells responded to stimulation of septal fibres. However, the responses were heterogeneous with 10/24 depolarising (FS: 1/22; IN-L1: 6/20; IN: 1/12; DS: 2/82), 12/24 hyperpolarising connections (FS: 7/22; IN-L1: 1/20; IN: 0/12; DS: 4/82), and a combination of a depolarisation followed by a hyperpolarisation 2/24 (FS: 0/22; IN-L1: 0/20; IN: 1/12; DS: 1/82). To estimate the amplitudes of cells, I used an approach similar to PV$^+$ fibres. However, since it was reported that depolarising choliner-

gic currents do not necessarily show a reversal, I used a *Gamma* error distribution for depolarising potentials (see equation (2.12)) and a normal error distribution for hyperpolarising potentials, which can exhibit reversal at negative potentials.

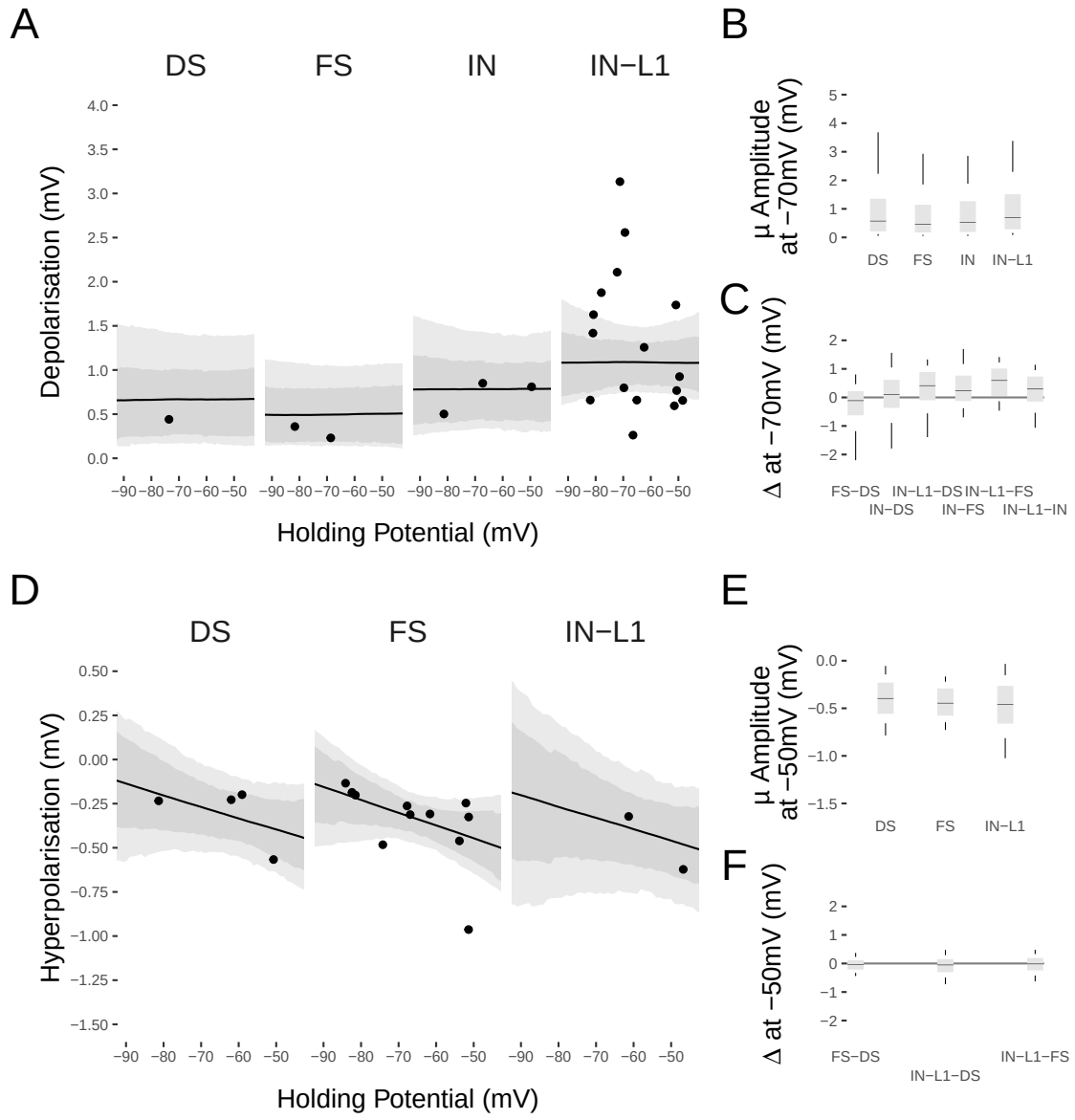

Figure 14: ChAT$^+$ input amplitude. *(A) ChAT$^+$ fibres stimulation induced input amplitude for depolarising cell inputs using different holding potentials. The grey shaded area shows the 80% and 95% highest density interval. (B) The estimated mean amplitude at -70 mV holding potential for cells being depolarised by ChAT$^+$ fibre stimulation. (C) Comparison of mean amplitude at -70 mV between different cell types depolarised by inputs. (D) ChAT$^+$ fibres stimulation induced input amplitude for hyperpolarising cell inputs using different holding potentials. (E) The estimated amplitude at -50 mV holding potential for cells being hyperpolarised by ChAT$^+$ fibre stimulation. (F) Comparison of mean amplitude at -50 mV between different cell types hyperpolarised by inputs.*

The *Gamma* distribution guarantees positive values and fits the data more appropriately than a normal error distribution, which overestimated the standard deviation.

As only little information for hyperpolarising reversals was available, I followed a standard regression with a regular intercept ($y = m \cdot x + n$). ChAT$^+$ input amplitudes between cell types did not differ in cells which were depolarised by cholinergic inputs (Figure 14C and D) and were similar at different holding potentials (Figure 14A) including for example $-70\ mV$ (DS: $0.66\ mV$ $[0.16; 1.39]$, FS: $0.48\ mV$ $[0.15; 1.03]$, IN: $0.78\ mV$ $[0.32; 1.45]$, IN-L1: $1.09\ mV$ $[0.73; 1.51]$). Hyperpolarisation occurred in the majority of FS cells but did not differ in amplitude from other cell types which were hyperpolarised by inputs (Figure 14D and F). Overall, the mean amplitude of hyperpolarisations was small in all cell types (Figure 14E, DS: $-0.40\ mV$ $[-0.64; -0.14]$, FS: $-0.45\ mV$ $[-0.64; -0.21]$, IN-L1: $-0.46\ mV$ $[-0.79; -0.13]$) but slower than GABAergic connections, from PV$^+$ connections, which could indicate different roles in inhibition.

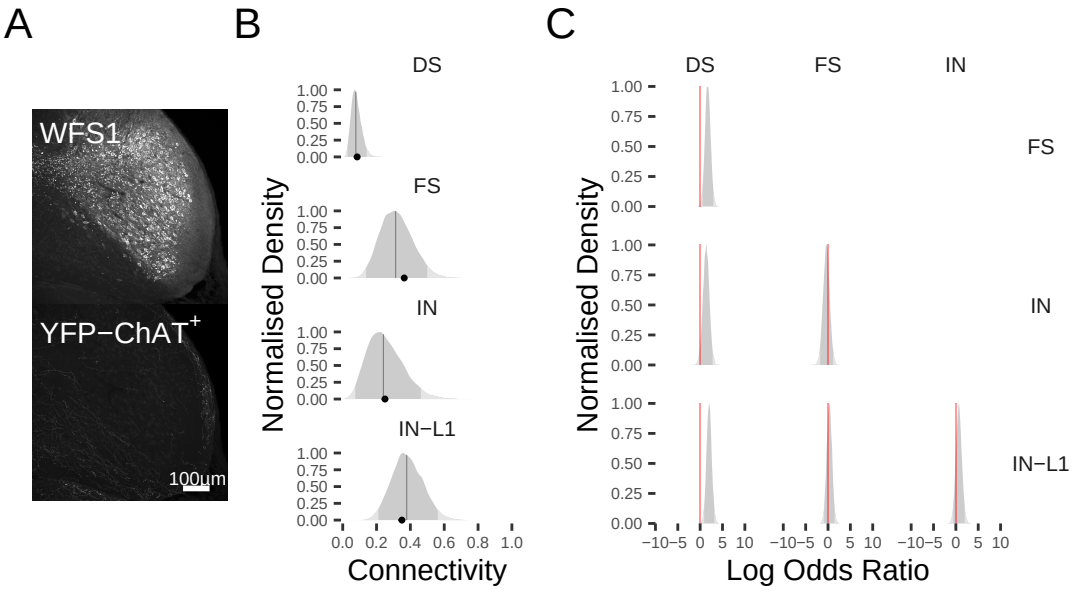

Figure 15: Connectivity of ChAT$^+$ MS cells to PaS. *(A) A horizontal section stained for WFS1 (top) and against YFP (bottom) which is expressed by ChAT$^+$ fibres coming from the MS. Note the preferential YFP staining in layer I (bottom) (B) The estimated connectivity as posterior distribution is shown in grey for different cell types (from top to bottom: DS, FS, IN IN-L1). The dark grey area represents the 95% credible interval of the posterior distribution and the light grey show the remaining tails. The vertical lines show the median of the posterior and the black dots at the bottom of each distribution the raw frequentist point estimates. (C) Probability distributions can be compared to each other by calculating the log odds ratio for any given comparison. The red line indicates the region of practical equivalence*

To quantify the overall connectivity of ChAT$^+$ fibres, we estimated the connectivity with the same model described in the previous section (3.1.2.1). The projections to

the PaS were less heterogeneously distributed than the fibres in PV-mice (Figure 11B) and showed dominant projections to the superficial layers (Figure 15A) with substantial connections to IN-L1 cells (7 of 20), resulting in an estimated connectivity of 0.38 $[0.21; 0.56]$. Similarly, IN were innervated by ChAT$^+$ projections (3 of 12) and showed a similar proportion of cells responding to light stimulation (0.24 $[0.07; 0.46]$). Contrastingly, FS cells were less likely to receive inputs from MS cholinergic cells compared to MS PV$^+$ projections (LOR for PV$^+$ vs. ChAT$^+$ connections to FS cells: 2.02 $[0.81; 3.29]$) but, with a connectivity of 0.31 $[0.14; 0.50]$, still had a tendency to be more strongly connected than DS cells (Connectivity of: 0.08 $[0.03; 0.14]$ and LOR of FS to DS: 1.70 $[0.54; 2.96]$). Even though IN-L1 cells only represent a very small proportion of the cells in the PaS, they were overrepresented in terms of cholinergic depolarising inputs. A drive of cholinergic cells in the MS will, therefore, lead to depolarised IN-L1 cells in the PaS. In contrast, projections to FS, while being comparatively as probable, will likely hyperpolarise FS cells. DS cells are one of the groups with the most mixed input types and the lowest connectivity.

3.2 *In-vivo*

Because of the strong GABAergic projections, targeting a large proportion of interneurons in the PaS which, in turn, inhibit other local cells in a timely manner, I sought out to investigate the consequences on the local network *in-vivo*. Compared to slices, the whole network is intact and can still interact on the dorsal-ventral axis. Therefore, I thought it crucial to measure whether the accurate and targeted inhibition we observed *in-vitro* will effectively entrain θ in the PaS. To test this hypothesis, I designed an experiment in head-fixed awake mice and recorded in the MS and the PaS simultaneously with two separate silicon probes which were both fitted with a glass fibre attached to an LED to illuminate both regions, respectively. The challenging part of these recordings is the location of each region. Both are fairly deep and cannot be directly accessed from above without implementing an angle. Once the target was reached, I waited for 15 minutes to allow the tissue to readjust and then started recording.

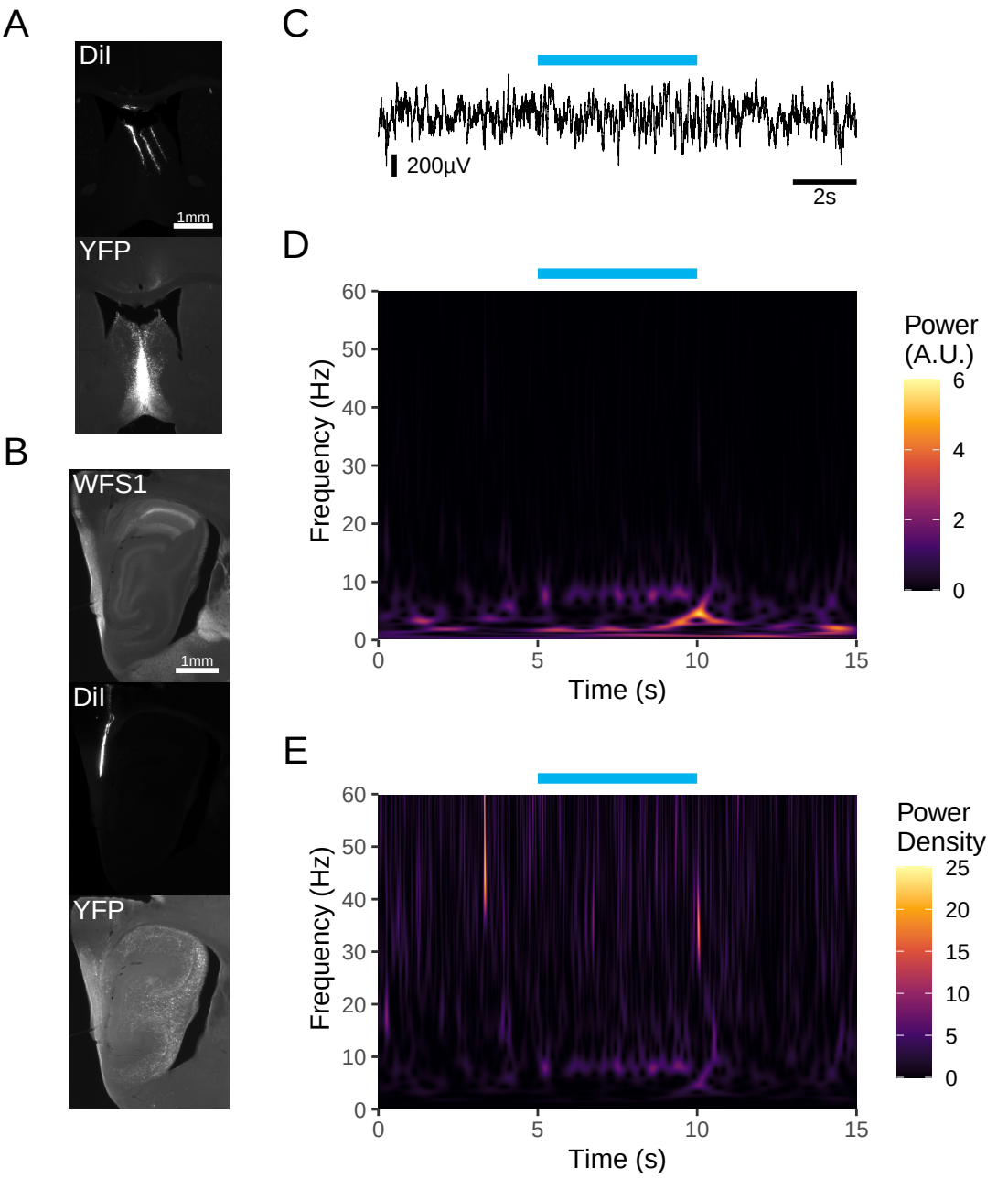

Figure 16: Overview of* in-vivo *recordings. *(A) shows a coronal section of the MS with the tracks of the silicon-probe (top) and YFP expression in the injection site of a PV-Cre animal. (B) A WFS1 labelled sagittal section of the PaS (top) with the visible track of the second silicon-probe (middle) ends in the PaS where the PV^+ fibres terminate (bottom). (C) A 15 s long single trial with a 5 s long 8 Hz pulse stimulation indicated with a blue line starting after 5 s. (D) The resulting power calculated from the wavelet transform of one trial. (E) The power density is derived from the same wavelet transform but uses a frequency normalisation (power · f).*

To reduce a potential deactivation of the ChR2 due to overstimulation, I switched between MS stimulation and fibre stimulation in the PaS. Since the MEC and the PaS are in close vicinity, recordings from both areas could be achieved in some

sessions (4/16), which offered a chance to directly compare the power and phase locking behaviour in the two structures. This is especially interesting due to the fact that they both get innervated by the MS, receive inputs via the hippocampal loop and project to each other. After establishing a baseline, I started to stimulate the MS and PaS with the LED respectively, using a pulse train stimulation at 2 Hz, 4 Hz, 8 Hz, 16 Hz, and 32 Hz to entrain the network. To identify ChR2-positive neurons in the MS, I applied 200-300 1 Hz 2 ms pulses. Since background activity during the recordings is dominated by lower frequencies and frequencies in the θ-band (Figure 16C and D), I repeated stimulation protocols in a pseudo random manner up to 20 times and applied a frequency normalisation ($power \cdot f$), which removes dominating low frequency activity (Figure 16E).

3.2.1 Power modulation in the parahippocampal network

The MS stimulation drastically increased the power density in the PaS and in the MEC (Figure 17). The increase was especially strong in the frequencies 8 Hz, 16 Hz, and 32 Hz and less pronounced during the 2 Hz and 4 Hz stimulation (Figure 17 and 19). In contrast to MS stimulation, stimulation of the fibres in the PaS and MEC did not change the power in any of the frequencies. This observation has crucial implications given that a failure to entrain the PaS or MEC using fibre stimulation could hint towards the higher importance of global MS interactions. To quantify the dependency on the frequency and location of the stimulation, I estimated the power using a hierarchical model of the *Gamma* family.

Since power is limited to only positive values and has a longer tail, a *Gamma* distribution (2.12) can capture the properties well. Furthermore, the model was set up to estimate correlations in the parameters and account for nested structures. Considering the non-linearity which can be observed in all conditions (see Figure 18), I had to consider including this behaviour in the estimation. The power independently of ChR2 stimulation does change with the frequency. Therefore, I decided to address this trend by using an asymptotic regression which defines power at 0 Hz to be 0 (see equation (2.16)). It simultaneously assumes that there is a ceiling and power is finite. By using the formula to estimate $\mu_{PowerDensity}$ with additional predictors such as the stimulation, we estimate the effect on $beta_{slope}$ or $beta_{max}$

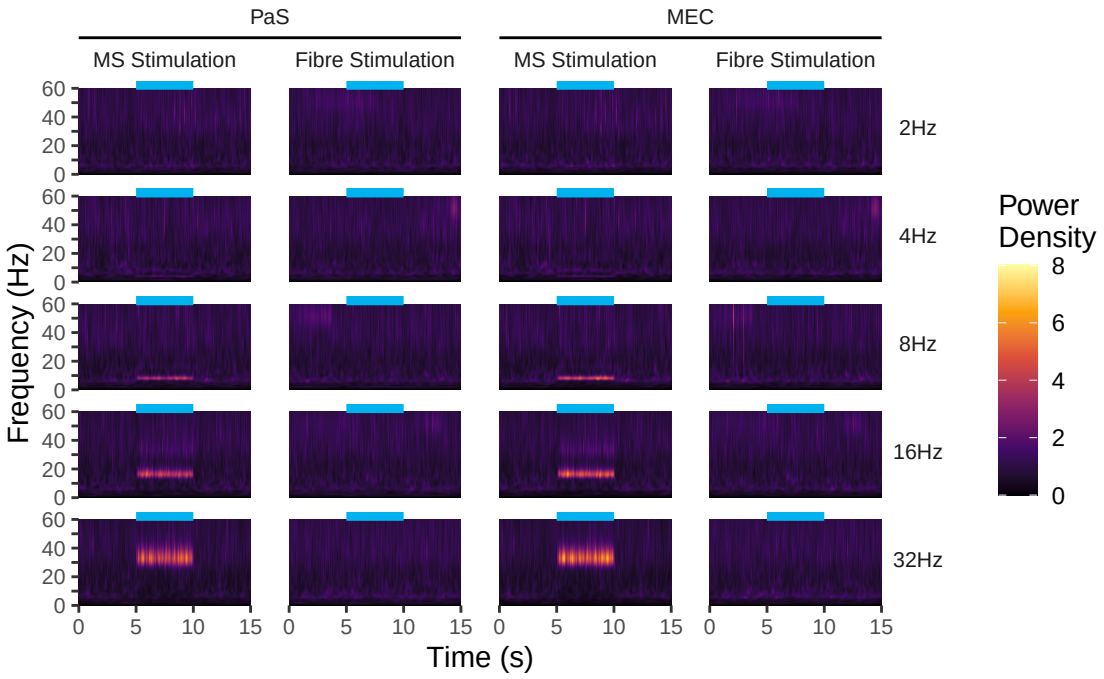

Figure 17: Power density in the PaS and MEC. *Power density of* 15 *s averaged over multiple trials. The y-axis shows the frequency (Hz) and the x-axis the time. Stimulation occurs from* 5 *s to* 10 *s (blue line). Major columns refer to the recording location (PaS or MEC) and minor columns to the stimulation location (MS or fibre stimulation). Each row shows a different stimulation frequency (*2 *Hz,* 4 *Hz,* 8 *Hz,* 16 *Hz,* 32 *Hz). Bright yellow indicates high power density and black low power density. An increase in power can be observed in stimulation blocks at the stimulation frequency when stimulating in the MS and is absent during fibre stimulation.*

indicating the ceiling for the power density. The asymptotic regression takes care of the limits which are defined by the network and how much power can be generated, and the *Gamma* error distribution with a log-link assures positive values close to 0. As expected, the analysis confirmed that the stimulation had an effect on the maximum power in trials where the MS was stimulated directly (PaS-Pre: 0.97 $[0.81; 1.15]$, MEC-Pre: 1.00 $[0.83; 1.18]$, PaS-Stim: 2.34 $[1.72; 3.05]$, MEC-Stim: 2.46 $[1.84; 3.20]$). However, a stimulation of only the fibres did not show such a change (PaS-Pre: 1.00 $[0.85; 1.18]$, MEC-Pre: 1.03 $[0.88; 1.21]$, PaS-Stim: 0.97 $[0.77; 1.20]$, MEC-Stim: 1.02 $[0.83; 1.24]$). In fact, when calculating the absolute difference between pre- and stimulation phases, the difference was centred around 0 (PaS: -0.03 $[-0.26; 0.19]$, MEC: -0.01 $[-0.24; 0.20]$). This indicates a complete failure of entrainment when only PV^+ fibres try to drive the LFP in the PaS or MEC. I then calculated the estimated fold change of power density given a frequency (Figure 20B). Since we estimated the complete posterior distribution of the

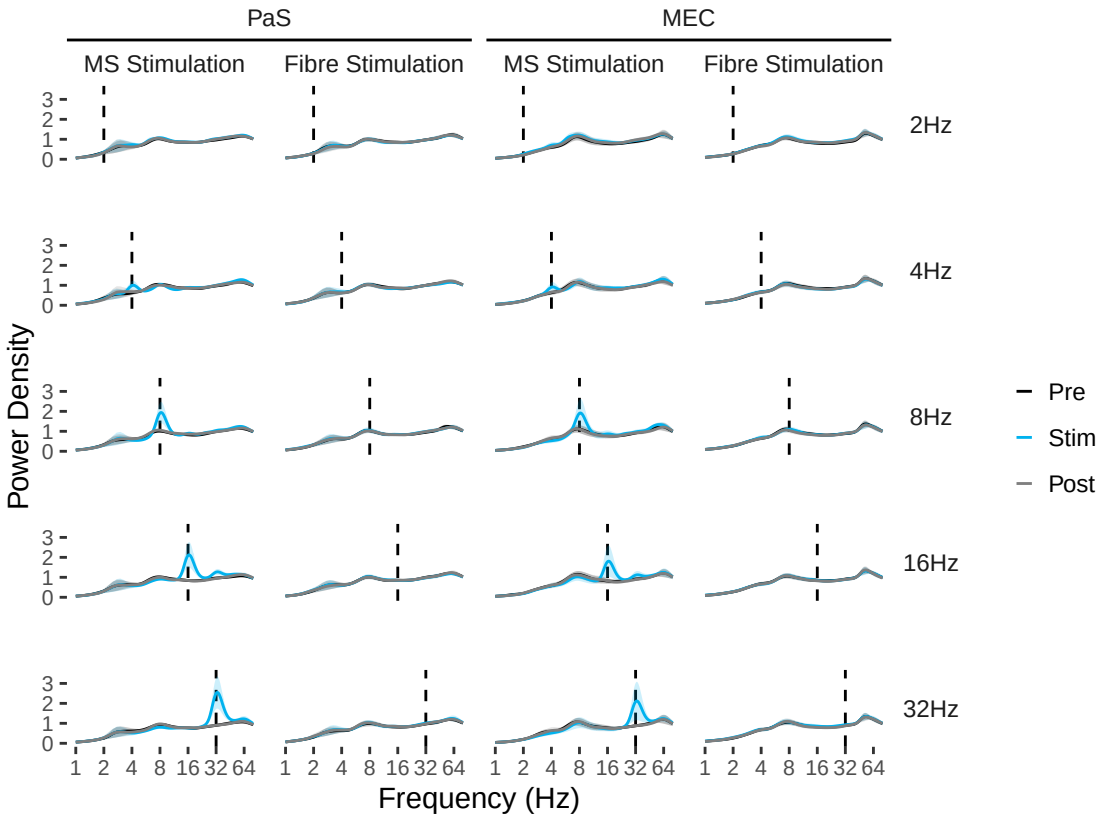

Figure 18: Power density spectrum in the PaS and MEC. *Power density spectrum during different stimulation frequencies (rows) extracted from the wavelet transform for time blocks before the stimulation (Pre - black line), during the stimulation (Stim - blue line) and directly after (Post - grey line). The dashed lines indicate the stimulation frequency whereas continuous lines show the mean power density and the SEM. The two left columns show responses in the PaS after septal stimulation (column 1) and stimulation of the fibres in the PaS (column 2). Analogous the two right columns show the response in the MEC. The frequency on the x-axis is log_2 transformed. PaS with MS stimulation: 9 session/4 animals; PaS with fibre stimulation: 9 session/4 animals; MEC with MS stimulation: 7 session/4 animals; MEC with fibre stimulation: 11 session/6 animals.*

power density for the pre-stimulation block and stimulation block, I could calculate the ratio ($PowerDensity_{Stim}/PowerDensity_{Pre}$) and compare the effect of the stimulation area (MS Stimulation and fibre stimulation) and frequency. A clear fold change in the MS stimulation paradigm could be observed early on (MEC at 3 Hz: 1.26 $[1.00; 1.57]$ and PaS at 4 Hz : 1.36 $[1.11; 1.67]$). This ratio will change with higher frequencies and can reach more than two times the power density of the pre-stimulation block with $32Hz$ stimulation (MEC: 2.36 $[1.81; 3.03]$, PaS: 2.30 $[1.73; 2.96]$). A higher change with higher frequencies could possibly be explained by the generally lower content of absolute power in higher frequencies (Figure 16D) and can, therefore, result in larger ratios. On the other hand, when looking at the

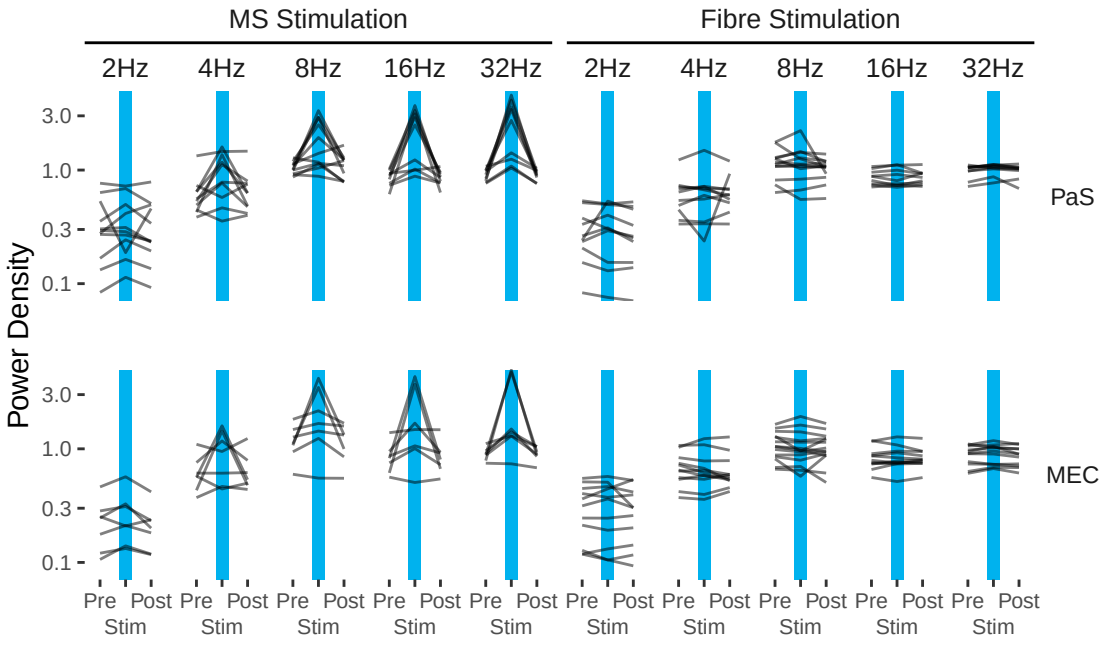

Figure 19: Power density is increased during MS stimulation. *Power density before (Pre), during (Stim), and after stimulation (Post) of the MS cells somatically (left) and fibre stimulation at the recording site (right). Increased power density during stimulation in the PaS (top) and the MEC (bottom) can be observed with MS stimulation but not using fibre stimulation. PaS with MS stimulation: 9 session/4 animals; PaS with fibre stimulation: 9 session/4 animals; MEC with MS stimulation: 7 session/4 animals; MEC with fibre stimulation: 11 session/6 animals.*

power density ratio between pre- and stimulation blocks during fibre stimulation, it is apparent that a stimulation effect on the power was absent (bottom Figure 20B). The credible intervals over all frequencies included the ratio 1 which means that the two blocks are likely not different. This can be observed in the PaS and the MEC, respectively, suggesting similar behaviour of the LFP and, possibly, similar mechanisms.

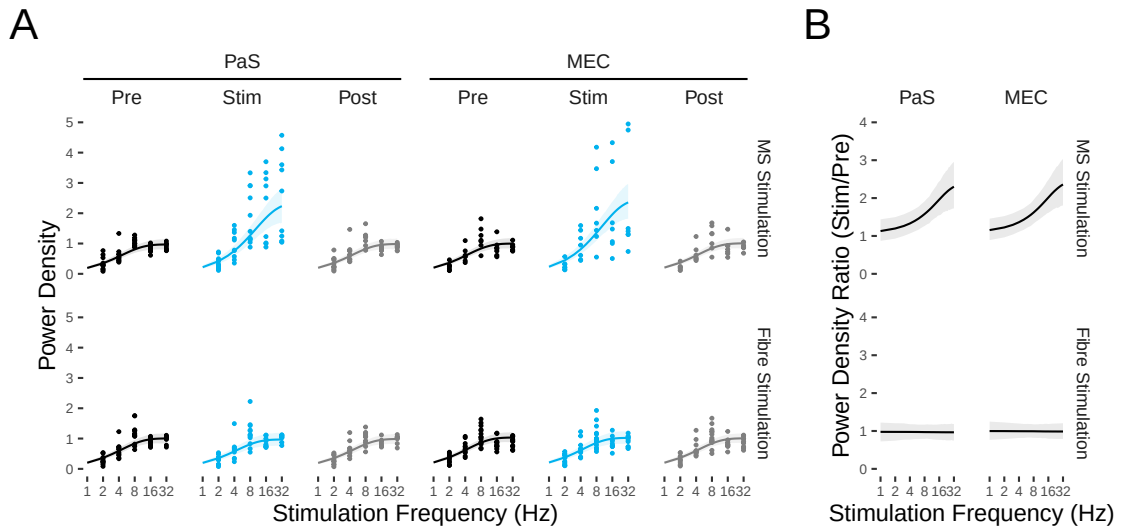

Figure 20: Power density on stimulation frequency. *(A) Power density during different stimulation frequencies. Black represents measurements before stimulation (Pre), blue during stimulation (Stim), and grey after stimulation (Post). The left half shows responses in the PaS and the right half in the MEC. The top row were measurements from MS stimulation and the bottom row from fibre stimulation in the PaS or MEC. Single dots are values from sessions. The line is the estimated mean population response with the 95% credible interval indicated as shaded area. The frequency on the x-axis is log_2 transformed. (B) The estimated ratio of the power density at the stimulation frequency during stimulation and pre-stimulation blocks. PaS with MS stimulation: 9 session/4 animals; PaS with fibre stimulation: 9 session/4 animals; MEC with MS stimulation: 7 session/4 animals; MEC with fibre stimulation: 11 session/6 animals.*

3.2.2 Phase lock in the parahippocampal network

Given that I observed an increase in power in the higher frequencies during MS stimulation but no differences when stimulating the fibres locally, the question arises as to whether fibres are more important to set the phase of the LFP than modulating the power. The phase represents the time component of periodic signals, whereas the power represents the strength and amplitude. For every single block I calculated the wavelet transform $W(a, b)$ for power calculations, as done before, but computed the phase using $atan2(\Im(W(a, b)), \Re(W(a, b)))$. Instead of averaging the power over trials, I calculated the ρ value for any given point in time and any frequency by treating the extracted phase of the wavelet transform as shown in equation (2.18). Thereby, I detected when phases were aligned over different trials. This can be done for all frequencies of the wavelet transform and is an effective way of quantifying phase lock using trial based data (Figure 21). The activation of the MS led to an increase of ρ during the stimulation period and dropped off rapidly after the

stimulation was finished.

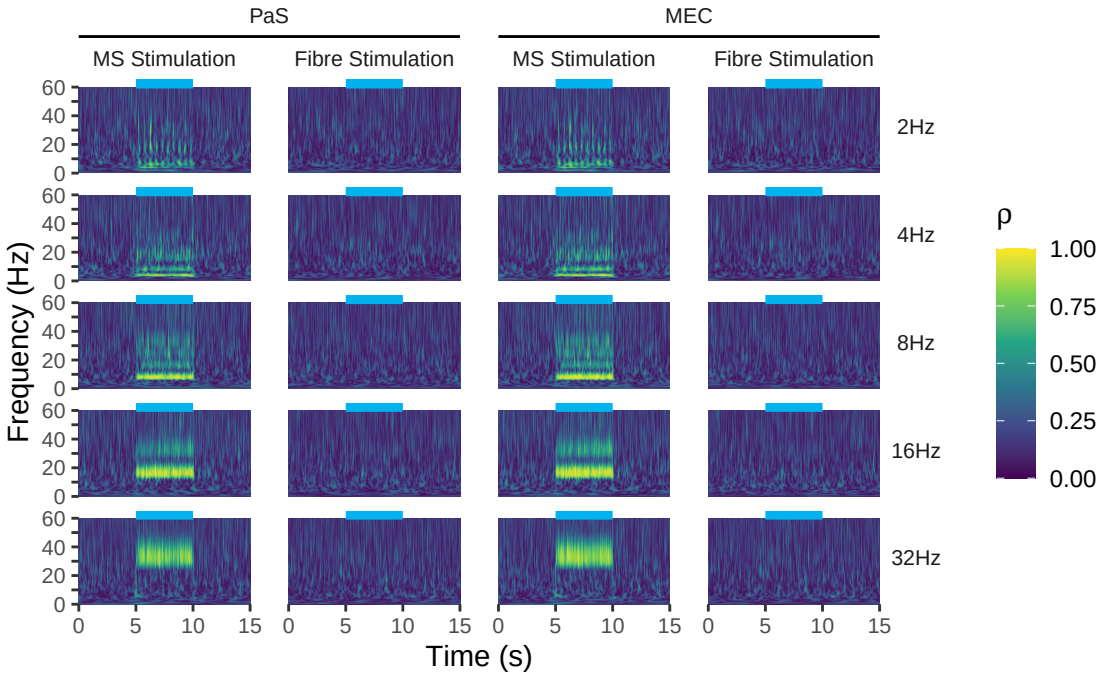

Figure 21: Phase lock in the PaS and MEC. *The phase lock was quantified as* ρ *where a value of* 1 *(yellow) indicates perfect phase alignment over repeated trials and* 0 *(dark blue) none. The random* ρ *given N trials is expected to be* $1/\sqrt{N_{trial}}$ *(MS stimulation:* 0.2*; fibre stimulation:* 0.183*). The y-axis shows the frequency (Hz) and the x-axis the time. Stimulation occurs from* 5 *s to* 10 *s (blue line). Major columns refer to the recording location (PaS or MEC) and minor columns to the stimulation location (MS or fibre stimulation). Each row shows a different stimulation frequency (*2 Hz, 4 Hz, 8 Hz, 16 Hz, 32 Hz*).*

I was able to detect that phases were aligned during MS stimulation at all stimulation frequencies and phase lock was even pronounced when using the 2 Hz stimulation. Due to the sensitivity of the ρ value, harmonics picked up by the wavelet transform are now more pronounced. Peaks of harmonics will appear as the multiple of the original signal and can be considered artefacts due to the fact that they most likely have no physiological relevance. The peak of the phase lock was centred around the stimulation frequency and seemed to change given the stimulation frequency. Similarly, a stimulation of the fibres in the PaS or the MEC did not appear to be sufficient to achieve phase lock (Figure 22). To quantify the strength of the phase lock in relation to pre-stimulus and-post stimulus times, I divided the simulation blocks into three parts as shown with the power. I then calculated the average ρ for any given frequency and stimulation block. As previously discussed, the ρ of a random distribution can be formalised as $\rho_{random} = \frac{1}{\sqrt{trial_N}}$ and, therefore, values

which are true phase lock should be significantly larger than our ρ_{random}, given our number of trials. We can think of ρ, similarly, as our connectivity, which was described by the *beta* distribution as a continuous value with same limits and similar interpretation. I calculated the log odds (equation (2.8)) ratio of ρ and ρ_{random} to eliminate false positives, which could occur due to a lack of trials. Hence, this approach allowed me to account for uncertainty in the estimate and transformed our values from a range of 0 and 1 to normally distributed data with possible values of $-\infty$ to ∞. Now a value of 0 means that there is no change in locking compared to ρ_{random}, negative values will describe the log reduction and positive values a log increase of phase lock.

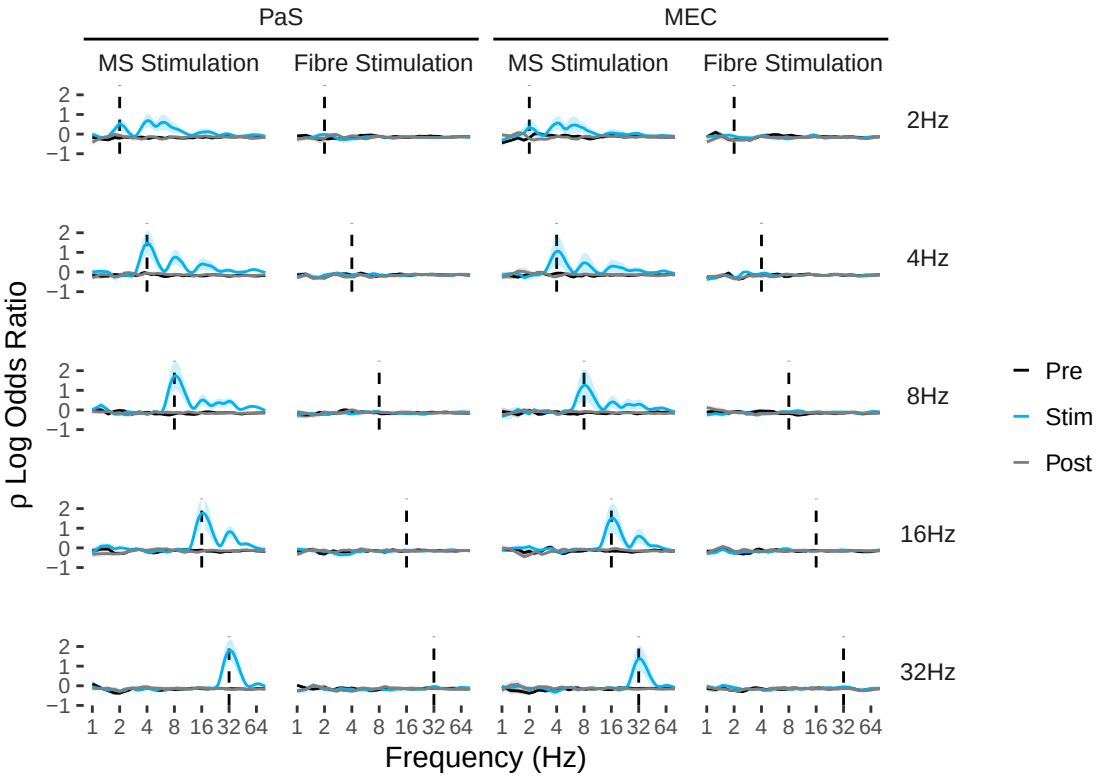

Figure 22: Phase lock spectrum in the PaS and MEC. *Log odds ratio of ρ and the expected random (ρ_{random}) during different stimulation frequencies (rows) extracted from the wavelet transform for time blocks before the stimulation (Pre - black line), during the stimulation (Stim - blue line) and directly after (Post - grey line). The dashed lines indicate the stimulation frequency, whereas the continuous lines show the mean ρ log odds ratio with its SEM. The log odds ratio represents a log fold change in phase lock compared to ρ_{random}. The two left columns show responses in the PaS after septal stimulation (column 1) and stimulation of the fibres in the PaS (column 2). Analogous the two right columns show the response in the MEC. The frequency on the x-axis is log_2 transformed. PaS with MS stimulation: 9 session/4 animals; PaS with fibre stimulation: 9 session/4 animals; MEC with MS stimulation: 7 session/4 animals; MEC with fibre stimulation: 11 session/6 animals.*

Equally to analysis of *in-vitro* connectivity data the region of practical equivalence (ROPE) for log odds ratios is $\pi/\sqrt{3} \cdot 0.1$ (≈ 0.183). Strong increases of phase lock can be seen at almost all stimulation frequencies, including their harmonics (Figure 22). The log-transform confirmed our suspicion that the fibre stimulation did not induce changes of locking.

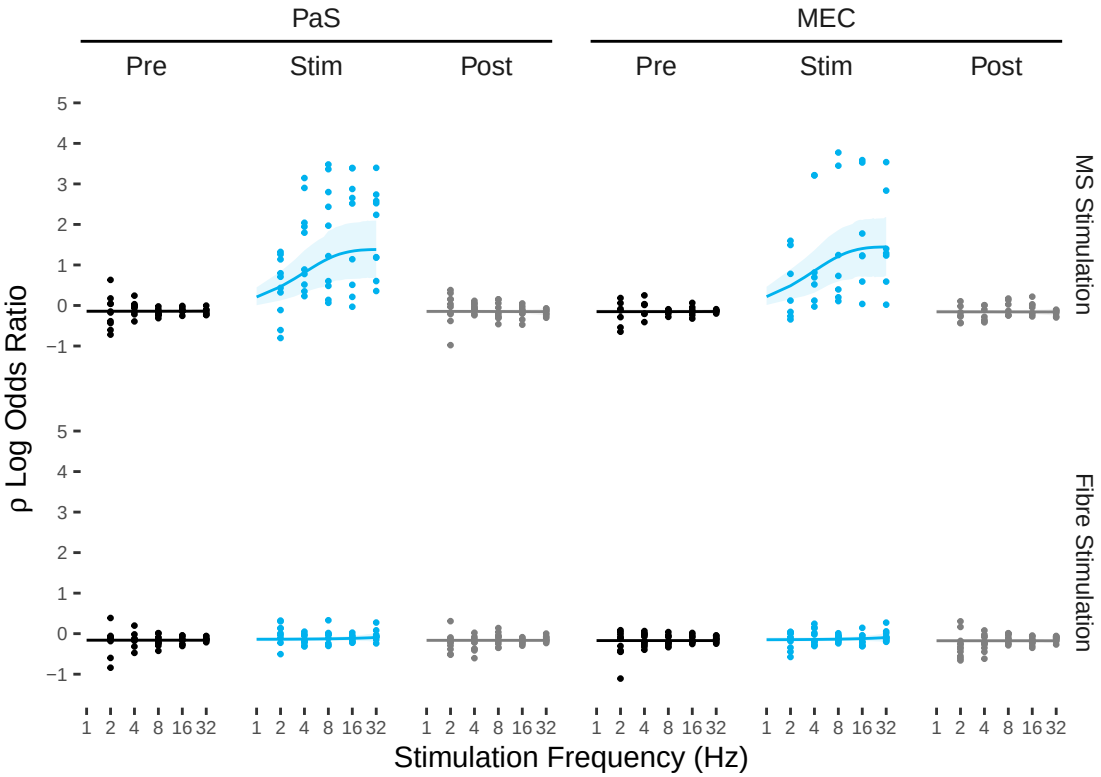

Figure 23: ρ log odds dependent on stimulation frequency. *Log odds ratio of ρ indicating phase lock during different stimulation frequencies. Black represents measurements before stimulation (Pre), blue during stimulation (Stim), and grey after stimulation (Post). The left half shows responses in the PaS and the right half in the MEC. The top row were measurements from MS stimulation and the bottom row from fibre stimulation in the PaS or MEC. Single dots are values from sessions. The line is the estimated mean population response with the 95% credible interval indicated as shaded area. The frequency on the x-axis is log_2 transformed. PaS with MS stimulation: 9 session/4 animals; PaS with fibre stimulation: 9 session/4 animals; MEC with MS stimulation: 7 session/4 animals; MEC with fibre stimulation: 11 session/6 animals.*

However, to validate and quantify whether there was a change, I used an asymptotic regression model with an hierarchical structure to account, not only for variance due to trials, animals, and sessions, but also recording locations, stimulation locations, and stimulation blocks (pre/stim/post) and type (burst) given a stimulation frequency. The estimated $\mu_{\rho_{LOR}}$ during pre and post blocks did not differ from each other or across stimulation frequencies, recording or stimulation locations (Figure

23). The asymptotic maximum of the LOR was significantly higher during MS stimulation trials in the PaS (1.38 $[0.68; 2.10]$) and the MEC (1.45 $[0.73; 2.18]$) and was outside the ROPE completely. In contrast, the stimulation of fibres led to no detectable change (PaS: -0.86 $[-4.28; 1.98]$ and MEC: -0.80 $[-4.13; 2.15]$). The pre-stimulus and post-stimulus blocks showed no change which could suggest that locking was not carried through for longer than the stimulation period. The stimulation frequency was shown to have an effect early on at 3 Hz PaS: 0.66 $[0.22; 1.13]$, MEC: 0.69 $[0.23; 1.15]$ and increased steadily until it reached an estimated $\mu_{\rho_{LOR}}$ of PaS: 1.38 $[0.68; 2.10]$, MEC: 1.45 $[0.73; 2.18]$ at 32 Hz.

3.2.3 PV$^+$ single units of the MS

Considering that the power and the phase was mainly driven by septal stimulation and not fibre stimulation, I wondered whether PV$^+$ cells in the MS were specially linked to the PaS or if other PV$^-$ cells were similarly set up. Due to the fact that the silicon probe in the MS was fitted with a light fibre, it was possible to give short 1 Hz 2 ms long pulses. These pulses were sufficient to drive somatic ChR2, depolarise the cell and make them spike (Figure 24A). I recorded 45 single units in the MS, 4 of which had to be excluded from the characterisation since they did not sufficiently spike during the 1 Hz stimulation (< 1000 APs). Based on 1 ms time bins a Z-score indicated the standardised difference in spiking and a 10 ms after stimulation onset window was used to evaluate the Z-score (Figure 24B).
Only cells which had a positive change of at least 8σ were classified as PV$^+$ cells. The high value was picked to account for low firing rates and sporadic spikes during the short 1 s window of stimulation. By using these criteria, I was able to identify 9 PV$^+$ cells in the MS.

To see if the identified cells corresponded to a homogeneous group of cells with similar functional properties, I calculated the spike autocorrelogram (Figure 25A). The fraction of cells, with simultaneously recorded LFP in the PaS, showed distinguishable burst properties and firing frequencies. Bursting cells can be identified by their sharp peaks close to the refractory period represented by the gap in the spike correlogram. Some of the cells also had oscillatory firing behaviour whilst others did not (Figure 25B).

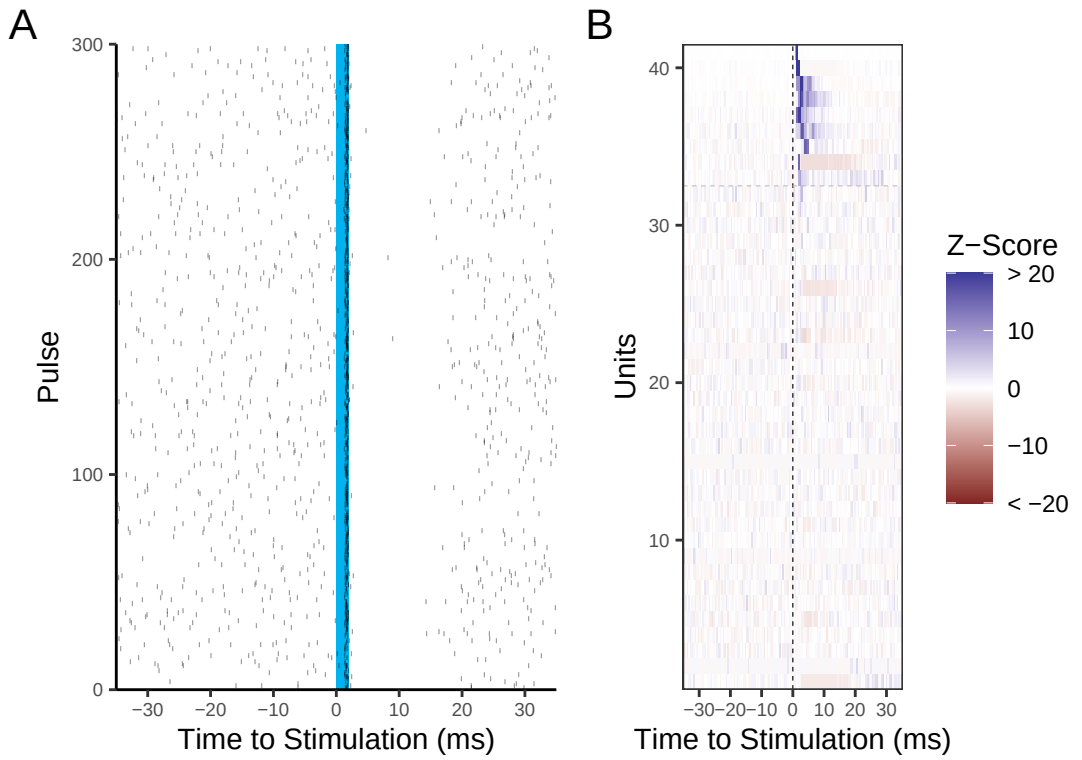

Figure 24: Identification of PV$^+$ MS cells. *(A) Single units were stimulated in the MS using a* 1 Hz 2 ms *long pulse of blue light (blue line). Spiking (short lines) was recorded over at least* 300 *trials so that regularly triggered spiking during the stimulation could be observed. (B) From spiking during the* 1 Hz *stimulation a Z-score could be derived from the spike count using* 1 ms *binning. Dark blue indicates a strong positive increase in firing and red a decrease. The Z-score is in* σ *from the mean over the whole* 1 s *time frame. Note the much stronger excitation (blue) compared to the inhibition after stimulation (red). The dashed vertical line shows the point of stimulation and the horizontal dashed line the units which had more than a* 8σ *increase during a 10 ms window. 41 Units from 14 session/7 animals.*

This can be seen by regular bumps in the autocorrelogram which can roughly be found at 0.2 s intervals (corresponding to $\sim$ 5 Hz i.e. θ rhythmic firing). When looking at the spike timing of PV$^+$ cells in relation to the PaS θ phase, cells did not show a clear coherent phase preference (Figure 25C and D) as a group. However, individual cells did fire at specific phases of the LFP, with some preferentially spiking at the peak (270°) and others at the trough 90° with different degrees of locking (Figure 25D). This data underlines that PV$^+$ in the MS are a heterogeneous group with distinct firing preferences.

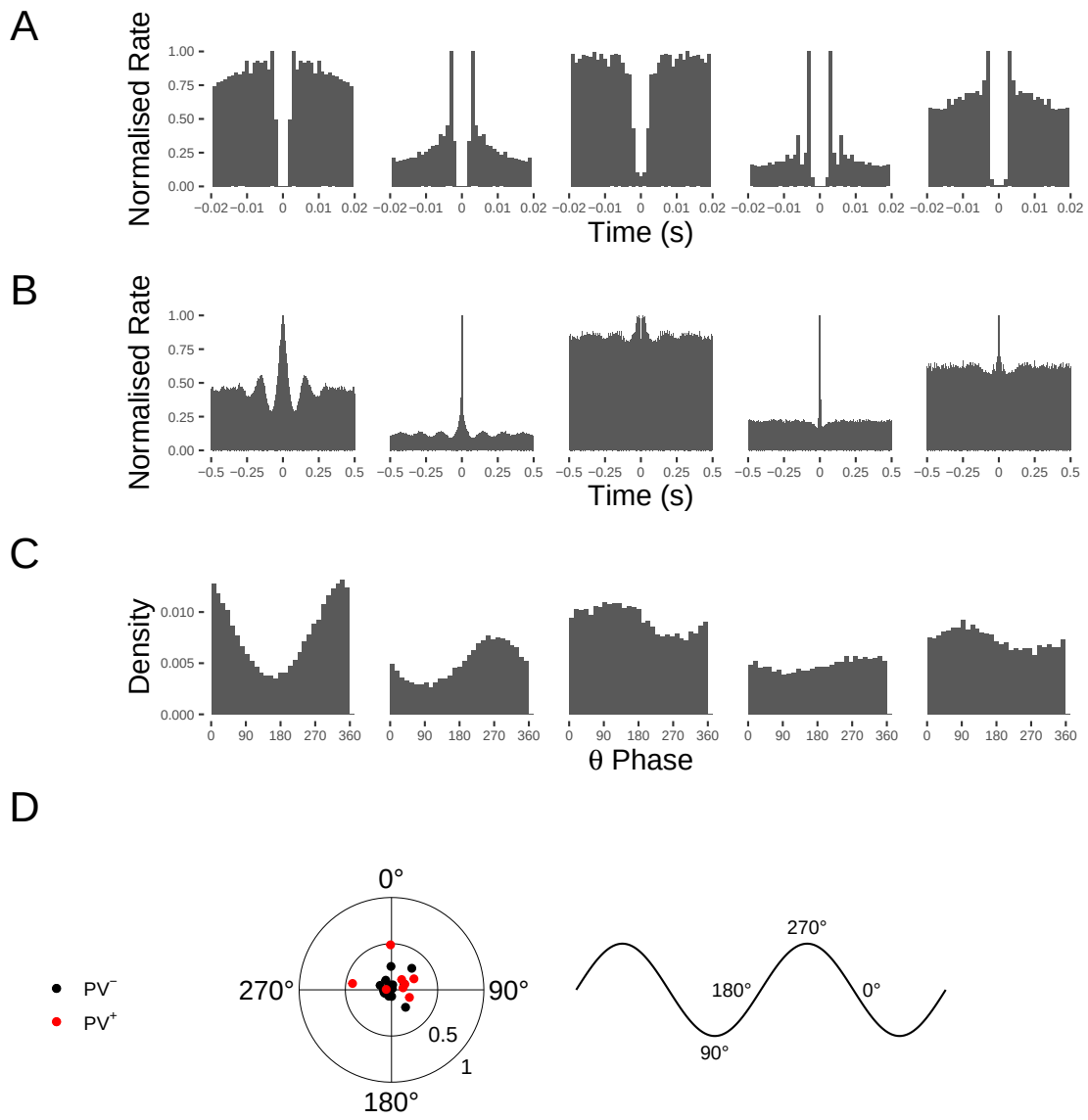

Figure 25: Diversity in PV$^+$ MS single units. *(A) Spike autocorrelogram for PV$^+$ single units in the MS show refractory period as gap and in two cells dominant bursting behaviour indicated by the large peaks at the centre. The rate was normalised to the maximum rate. Inter-spike timings are given in seconds. (B) A larger time window of the same cells indicates different oscillatory behaviours. (C) The corresponding PaS θ-phase preference for the units range from the trough of the θ-oscillation (90°) to the peak (270°). (D) An overview of θ phase lock to the MEC and PaS of PV$^+$ cells (red) and PV$^-$ cells (not activated by light, black). Circles indicate the strength of the phase vector (0.5,1).*

4

Discussion

For over 80 years scientists have been trying to explain the presence of θ oscillations in the brain (Berger, 1929; Jung and Kornmüller, 1938), attempting to identify potential locations responsible for generating such activity (Petsche et al., 1962). To date, we still do not completely understand the exact function of these oscillations (Buzsáki, 2002; Colgin, 2013; Müller and Remy, 2018). However, significant steps towards understanding interactions between areas and cells have been achieved and multiple targets identified to gain further insights into θ function and generation (Rawlins et al., 1979; Swanson and Cowan, 1979; Gaykema et al., 1990; Dragoi et al., 1999; Gonzalez-Sulser et al., 2014). Since one of the important regions for θ rhythm generation is the MS, I addressed the question of whether the PaS – a formerly, relatively unexplored member of the parahippocampal circuit region which exhibits strong θ oscillatory activity *in-vivo* (Ebbesen et al., 2016; Tang et al., 2016) and on a cellular level (Glasgow and Chapman, 2008) – receives projections from the MS. Due to the PaS contributing major excitatory inputs to the MEC, it is well-positioned to relay oscillatory excitation controlled through the MS.

I focused on two groups of septal cells which play an important role in θ generation in the hippocampus and MEC and are, thus, potentially crucial for the PaS. Hence, we recorded and classified cells in the PaS *in-vitro* to map connections from MS PV^+ and MS $ChAT^+$ cells. In addition to this descriptive account of cellular physiology and in order to establish the potential impact of septal connections in mediating the oscillatory activity, I then investigated network activity in head-fixed awake mice *in-vivo* and quantified the effects of modulating septal projections on the LFP. I estimated parameters of measurements using Bayesian hierarchical models

(Gelman, 2006) to account for nested structures which generally occur in such an experimental design. Additionally, this approach is less likely to negatively bias the reader and overcomes caveats associated with p-values commonly used in papers (Buchinsky and Chadha, 2017; Makowski et al., 2019).

4.1 Interneurons have distinct cell properties

Until recently, descriptions of PaS cells *in-vitro* in the literature were mainly based on morphology (Funahashi and Stewart, 1997). In our study, we classified cells in the parasubiculum on a larger scale using electrophysiological properties, immunohistochemistry and clustering approaches (Sammons et al., 2019). In the present study, I therefore employed the same tools including hierarchical clustering to generate three cell type clusters based on previous data. I then split layer I cells as a separate group and verified that they, indeed, had distinct cell properties. I found that, even when a targeted approach to record interneurons is used, a large proportion of cells is still part of the putative pyramidal cell cluster (Sammons et al., 2019). This group of cells makes up 80% of the PaS population and is the major contributor to the glutamatergic output of the PaS. However, an important observation I made is that of the distinction of regular slow firing interneurons in layer II of the PaS and interneurons in layer I. The two groups were previously characterised as one group (Sammons et al., 2019), however, IN-L1 cells emerged to be significantly different in major parameters such as $firing\ frequency$, $FWHM$, C_m and the *slopes* of the action potential (Figure 7). This suggests that action potential dynamics might be distinct from other interneurons and can potentially lead to different computational consequences. One possible advantage of these dynamics could be that a wider action potential can lead to an increase of presynaptic Ca^{2+} concentration, leading to a more reliable transmission (Geiger and Jonas, 2000). A relatively low $rheobase$ and an almost instantaneous initiation of firing upon stimulation could reliably relay information to downstream partners, which might make IN-L1 cells an important part of the local network (see for $rheobase$ and *latency* Table 1).

In contrast, FS cells showed a much higher maximum $firing\ frequency$, which is in line with the behaviour of PV^+ interneurons in the PaS, PrS and MEC (Nassar et al., 2015; Martínez et al., 2017; Sammons et al., 2019). FS cells generally had

to be more depolarised to initiate spiking, but could sustain a continuously high *firing rate*. Recently, it has been shown that the PaS is the area with the highest density of PV^+ cells in the whole mouse brain (Bjerke et al., 2021). This underlines the importance and potential influence of this cell type in the region. Due to the inhibition of the local network, which can be mediated by FS spiking cells and the high connectivity of PV^+ interneurons (Hangya et al., 2009; Stark et al., 2013; Roux et al., 2014; Fuchs et al., 2016) as found in the MEC and hippocampus, I hypothesised that FS cells could be preferential targets for disinhibition through PV^+ MS cells. This could potentially release a "brake" in the parahippocampal circuitry and drive θ oscillations.

4.2 PV^+ connections to the PaS

In addition to the classification of these cells *in-vitro*, I also employed an optogenetic approach to understand interactions between the MS and PaS. To do so, cells were recorded in whole-cell configuration in slices and ChR2 expressing fibres were activated using short light pulses. Measuring connections from the MS to PaS in PV-Cre mice, we could demonstrate that previously reported anatomical projections indeed make functional connections (Unal et al., 2015; Tang et al., 2016). Unal et al. (2015) found that the PV^+ fibre density was highest in the PaS, compared to the hippocampus or other parahippocampal regions, and made putative contacts to parasubicular PV^+ cells and CB^+ cells. CB was previously identified as having strong overlap with PV^+ neurons in the PaS and is mainly a marker for local GABAergic cells (Sammons et al., 2019).

We presented evidence that interneurons indeed constitute most of the functional connections confirming previous morphological evidence (Figure 11). Furthermore, we could show that the proportion of cells being inhibited by GABAergic inputs was the highest in FS interneurons, which most likely represents a large proportion of parasubicular PV^+ and CB^+ interneurons (Sammons et al., 2019). Other studies established an important role of FS cells in θ modulation in the MEC and hippocampus (Amilhon et al., 2015) and found PV^+ cells in the hippocampus and cortex to orchestrate spike timing during θ phases (Stark et al., 2013; Roux et al., 2014). The high connectivity of FS cells in the PaS is striking and in line with previ-

ous studies investigating septal projections to the MEC or hippocampus where PV^+ fibres preferentially target PV^+ fast spiking interneurons leading to disinhibition of the local network (Melzer et al., 2012; Gonzalez-Sulser et al., 2014; Fuchs et al., 2016). Based on recent local connectivity data of pyramidal cells and interneurons in the PaS (Sammons et al., 2021), it can be proposed that an inhibition of FS cells through the MS will also lead to a reduced inhibition of pyramidal cells in the PaS. The high connectivity and recurrent connection scheme between FS and pyramidal cells suggest that the PaS is well-positioned to generate oscillatory network activity. Given the high firing rate of FS cells, a reduction of FS spiking can lead to a release of strong local inhibition of the network. As I have shown, the inhibition of spiking and entraining of frequencies via septal fibre stimulation in interneurons suggests that local θ entrainment via interneurons could be possible and effective (Figure 12). Furthermore, our data shows that regular firing interneurons were also targets of septal PV^+ cells increasing disinhibition of the network and further allowing DS to be active. A similar proportion of cells was found to be inhibited in the MEC (Gonzalez-Sulser et al., 2014; Fuchs et al., 2016), further supporting the notion that PV^+ MS projections follow common targeting schemes in the cortex.

To our surprise, IN-L1 cells were inhibited by the activation of PV^+ fibres, a connection not reported in previous studies investigating MS PV^+ projections. Due to the position of IN-L1 cells in cortical circuits, this novel connection could have significant new implications for the network. It has been shown in the somato-sensory and visual cortex of rats and mice that layer I interneurons exhibit recurrent connections to pyramidal cells of layer II and III, broadly inhibit a vast majority of layer II and III interneurons and are highly interconnected (Oláh et al., 2007; Wozny and Williams, 2011; Jiang et al., 2015). This places them in a central position where they can inhibit a whole interneuron network while also modulating pyramidal cell activity. Whether or not we have similar connectivity schemes outside of known sensory cortices in the PaS or MEC remains unknown. This open question could provide important information about the workings of septal-parahippocampal interactions. Combining these results, I hypothesise that septal PV^+ cells contribute to an accurately timed inhibition of interneurons, which leads to an increase in DS firing while background activity – not synchronised inputs – might be reduced through

IN-L1 cells regulating the overall inhibition (Figure 26A). Overall, the increase in DS activity through disinhibition from septal PV^+ cells will increase excitatory output to the MEC (Canto et al., 2012) and relay information to entorhinal pyramidal cell clusters known for their spatial coding (Tang et al., 2016). Consequently, excitation from the PaS could drive grid-cells in the MEC and synchronise other behaviourally relevant cells across the parahippocampal network. It is not known whether or not the PaS receives distinct inputs from the MS which are integrated in the parahippocampal network independently of other regions. Studies investigating projection patterns using juxta-cellular recordings provided evidence that MS PV^+ orchid cells can simultaneously target MEC and PrS cells, although, none of the cells projected to the PaS (Viney et al., 2018). A failure to detect common projections could arise due to the limited number of cells which can be labelled using the juxta technique or suggest, given the high density of projections to the PaS, that the PaS is targeted by a different cell group which exclusively and with high divergence inhibits the PaS or other structures. Answering this question could lead to a better understanding of how MS inhibitory signals are integrated in the parahippocampal network and could elicit new questions for the future.

4.3 $ChAT^+$ connections to the PaS

Cholinergic projections to the parahippocampal network have been proposed to play an important role in learning and memory and are implicated in θ generation (Heys et al., 2012). One of the main regions to provide such cholinergic innervation is the MS (Záborszky et al., 2018) and lesioning specifically cholinergic MS neurons using a selective neurotoxin (IgG192-Saporin – SAP) will lead to the impairment of spatial working memory (Robinson et al., 1996; Walsh et al., 1996; Johnson et al., 2002). But it should be noted that lesions using SAP do not achieve a complete reduction of acetylcholine activity (Chang and Gold, 2004). Such strong effects motivated us to look into the targets of MS $ChAT^+$ projections to the PaS. To map connections, we used an optogenetic approach specifically targeting $ChAT^+$ fibres from MS cells and measured synaptic responses in the PaS *in-vitro*.

Strikingly, $ChAT^+$ connections mostly targeted superficial cells by depolarising them. This is in line with previous findings in the MEC (Desikan et al., 2018), where

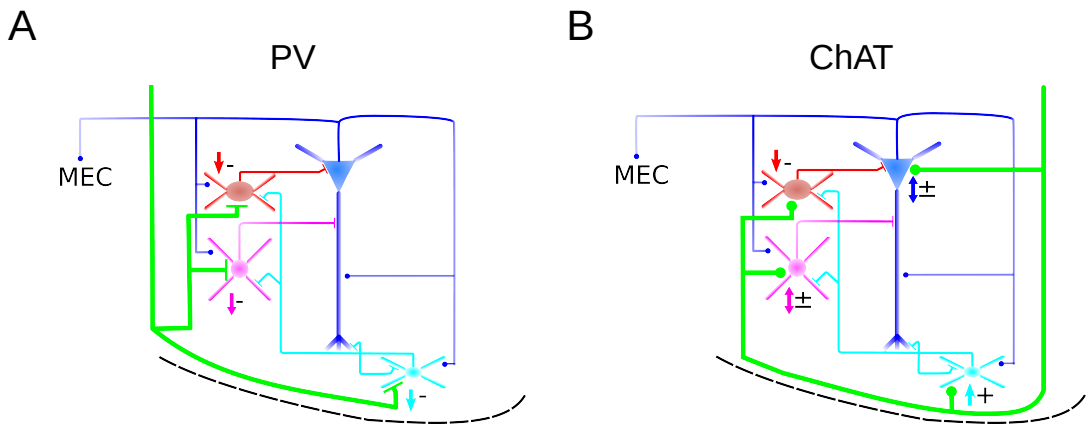

Figure 26: Schematic of PaS network for PV$^+$ and ChAT$^+$ inputs. *The connectivity scheme for inputs from the MS. Arrows indicate the effect of MS inputs onto cells. Red cells represent FS cells, pink IN cells, turquoise IN-L1 cells, and blue DS cells. Synapses are represented as circles for excitatory or cholinergic synapses and lines for inhibitory GABAergic synapses. Local IN-L1 connectivity is not yet confirmed in the PaS and is informed from studies in other cortical areas (Oláh et al., 2007; Wozny and Williams, 2011; Jiang et al., 2015). Septal fibres are presented in green and arrows indicate the MS input effect on the target cells (up +/down -/both ±). DS cells project to the MEC and have local recurrent connections. The black line at the bottom indicates the pial surface. Cells connecting to themselves do not necessarily represent autaptic connections to a single cell but cell type connections to the same cell type. (A) shows the scheme for PV$^+$ MS fibres and (B) the corresponding scheme for ChAT$^+$.*

the connectivity was similar and mainly showed depolarisations of IN-L1 cells as well (Figure 15). A common pattern could mean that cholinergic activation increases the activity of layer I interneurons in the parahippocampal network and mediates local inhibition. Slow depolarisations of IN-L1 cells could lead to increased activity and, in combination with GABAergic inhibition of IN-L1 through PV$^+$ fibres, synchronise spike timing. Given that the activity of cholinergic cells in the MS and acetylcholine release is related to movement and behaviour (Dudar et al., 1979; Nilsson et al., 1990), it could result in an increased involvement of superficial interneurons during such behaviours. This could be an important mechanism for network modulation which might also be found in the MEC in the future. The result of such a combined effect would provide evidence for an important link between layer I interneuron activation and behavioural states (Vandecasteele et al., 2014; Ma et al., 2020). A substantial proportion of layer I cells in the MEC have been shown to display $GABA_AR$ responses (Desikan et al., 2018). I did not observe such a fraction of hyperpolarisations in the ChAT$^+$ data. However, a larger sample of layer I cells could reveal similar proportions in the future. Generally, amplitudes of de- and

hyperpolarisations were small in all cell types (Figure 14A and D), but still large enough to indicate that cholinergic receptors were active. Hence, different muscarinic mechanisms which were not detected in this study could effect PaS network activity (Caruana and Chapman, 2004; Glasgow and Chapman, 2007, 2008).

In particular, FS cells were similarly likely to be connected responded in most of the cases by hyperpolarisation, suggesting a complementary mechanism to MS PV^+ mediated inhibition. Therefore, inhibition of FS cells in the PaS and MEC via MS $ChAT^+$ cells seems to follow similar rules to previously mentioned PV^+ projections. The inhibition through cholinergic fibres could reduce membrane potential of FS cells enough to enable PV^+ cells in the MS to more efficiently inhibit FS cells with an increased success rate. In comparison, 25% of the PaS IN clusters were affected through depolarisation, hyperpolarisation or both simultaneously. Cells of the IN cluster represent a heterogeneous population expressing somatostatin, reelin and calbindin. This could potentially explain diverse responses to $ChAT^+$ MS fibre stimulation (Sammons et al., 2019). In contrast to data from the MEC, I did not detect a high response rate for $ChAT^+$ fibres stimulation in pyramidal cells (Desikan et al., 2018). Whereas MEC pyramidal cells depolarise in 40% of the cases upon $ChAT^+$ fibre stimulation (Desikan et al., 2018), I could only detect a small fraction of 3 to 14% in DS cells. However, given the cell density of DS cells in the PaS, it could still reflect a substantial amount of affected cells with potentially large network effects. Previous studies have shown that the pronounced sag potentials of cells in the MEC are I_h mediated and can be modulated by carbachol an agonist for nicotinic and muscarinic receptors (Sparks and Chapman, 2014). Analogous to the MEC cells, PaS pyramidal cells have similar sag-properties which are mediated by I_h suggesting the possibility of similar mechanisms (Glasgow and Chapman, 2008). Considering that the probability of direct effects on hyper- or depolarisation in parasubicular DS cells after MS cholinergic stimulation was low, it is possible to envisage an effect which reduces I_h conductance and, therefore, subtly modulates the intrinsic properties of the cell (Alonso and Klink, 1993; Heys and Hasselmo, 2012; Pastoll et al., 2012) such as the intrinsic oscillatory frequency (Giocomo and Hasselmo, 2008). Reaching high enough acetylcholine concentrations using fibre stimulation, however, can be challenging *in-vitro* due to circulating ACSF. A potential result of such a

modulation can be observed in the MEC when activating a sustained release of acetylcholine from the MS by releasing acetylcholine from cholinergic fibres using a chemogenetic approach in freely behaving mice (Carpenter et al., 2017). An increase in acetylcholine will slightly decrease the θ frequency peak without changing the power. Cholinergic cells in the MS seem to be dependent on the behavioural state and an artificial activation will, for example, only lead to changes when the animal is anaesthetised or the network in an inactive state (Vandecasteele et al., 2014; Mamad et al., 2015). However, Vandecasteele et al. (2014) have shown that the activation of cholinergic cells during a low activity state, will not lead to an entrainment of θ in the hippocampus but rather increase power at the already occurring θ frequency band. In contrast, running animals will not show power changes using the same stimulation due to potentially increased cholinergic activity.

A different effect of an increase in acetylcholine in the PaS and MEC, is a reduction in amplitude of excitatory inputs combined with an increased facilitation allowing for enhanced temporal summation of inputs, which is especially efficient at γ-frequency (Glasgow et al., 2012; Sparks and Chapman, 2014). Such a mechanism could potentially prime PaS pyramidal cells for synaptic modification through increased acetylcholine concentration during MS mediated θ and, therefore, strengthen relevant synchronously occurring inputs to the MEC and PaS, as was previously shown in the hippocampus (Huerta and Lisman, 1995). Evidence to support the hypothesis that the MS could contribute to such an acetylcholine increase was presented by Hamam et al. (2007), who have shown that facilitation of inputs mediated by muscarinic receptors in the MEC is larger during movement as opposed to an immobile state. Additionally, Dudar et al. (1979) recorded an increase of hippocampal acetylcholine concentration during running phases and were able to abolish the increase by lesioning the septal area. Furthermore, a block of muscarinic receptors will lead to a reduced speed-θ relationship in the MEC and, more importantly, change the coupling of θ nested γ in the MEC and hippocampus (Hentschke et al., 2007; Newman et al., 2013). Given the strong excitatory output of the PaS to the MEC, improved temporal summation could occur during θ nested γ cycles and play an important role in memory formation (Huerta and Lisman, 1995).

Taken together, this suggests the importance of MS cholinergic projections, es-

pecially during behavioural states via the activation of layer I interneurons and disinhibition of the PaS through FS cells, but also a potential impact on memory formation and strengthening of connections through synaptic facilitation.

4.4 *In-vivo* MS PV$^+$ activation

4.4.1 MS stimulation drives LFP

Based on the target projection profile of MS PV$^+$ fibres to the PaS, I designed an experiment in awake mice to establish whether the LFP of the PaS can be modulated by MS intervention. Further, I wanted to investigate whether the different anatomical structure of the PaS, in comparison to the MEC, results in different LFP properties during fibre stimulation (Witter et al., 2014; Tang et al., 2016; Sammons et al., 2019). The density of pyramidal cells and the organised structure of pyramidal dendrites in the PaS suggests that LFP responses could be pronounced due to alignment (Herreras, 2016).

Stimulating septal cells in the MS directly led to a drastic increase in power at the stimulation frequency in the PaS (Figure 18). The power increase was also positively dependent on the stimulation, which meant that a higher stimulation frequency increased power more in relation to the baseline (Figure 20B). However, differences in power between MEC and PaS were not detected. This suggests that the dendritic organisation did not contribute significantly or that LFP signal was potentially equal due to volume conductance (Kajikawa and Schroeder, 2011). Future current source density analysis could address a possible volume conductance and lead to more insights into PaS-MEC interactions.

Similarly, phase locking was strong over a wide range of stimulation frequencies, suggesting that stimulation synchronised the network reliably (Figure 22). Even at the maximum tested 32 Hz stimulation, phase locking was high in the PaS and MEC. Recent findings in $Pvalb^{Cre}$ rats showed that direct cell stimulation can also lead to strong entrainment of the stimulation frequency in freely moving animals and even abolish naturally occurring θ (Lepperød et al., 2021). A stimulation of up to 32 Hz still produced reliable entrainment, as also shown by Lepperød et al. (2021). I, however, observe a reduction in natural occurring θ, which could be due

to very low power in θ frequencies during immobility (Figure 18) (Vanderwolf, 1969; McFarland et al., 1975). The MS stimulation led to a synchronisation of the local MS network but also likely synchronised activity in the hippocampus (Etter et al., 2019) which could provide excitation to the MEC and PaS (Groen and Wyss, 1990; Rowland et al., 2013; Zhang et al., 2013).

4.4.2 Fibre stimulation fails to drive LFP

Stimulating the fibre terminals in the PaS and MEC failed to induce changes compared to the MS stimulation alone. In contrast, other studies were able to produce LFP changes when stimulating terminals in the MEC of freely moving rats and mice (Lepperød et al., 2021; Schlesiger et al., 2021). In moving animals, PV^+ fibres of the MS seemed to be sufficient to drive LFP responses, even though with slightly weaker magnitude. This suggests that a higher baseline activity in the network is required and can, thus, be modulated by fibre stimulation alone. Hence, the difference between immobile animals and running animals can be described as an excitatory drive through movement.

The behavioural state of an animal for θ was shown to have significant consequences for the experimental paradigm (Vandecasteele et al., 2014; Mamad et al., 2015). A potential origin for excitatory drive was presented by Justus et al. (2017) who showed that during locomotion glutamatergic fibres of the MS projecting to the MEC are active and increase activity when the animal increases speed. Another study was able to initiate movement of the animal by stimulating the MS directly via glutamatergic cells, and could entrain the LFP response in the hippocampus (Fuhrmann et al., 2015). However, such an entrainment was abolished when a glutamate blocker was applied in the MS to shut down local transmission strengthening the evidence for the importance of GABAergic projecting neurons for θ long-range entrainment. It also underlines the important role for $VGluT2$ (glutamatergic) cells in the local MS circuit rather than increasing excitation in distant areas. Similar findings have been produced by Robinson et al. (2016) who could induce entrainment in $VGluT2-Cre$ mice only when stimulating MS cells locally and failed when stimulating the fibres. Septal glutamatergic cells were proposed to synchronise local activity in the MS and, therefore, drive GABAergic and cholinergic cell activation

targeting the hippocampus (Robinson et al., 2016), which in turn can provide excitation to the parahippocampal network. Activation of cholinergic cells in the MS increases power in the θ and γ band of anaesthetised mice (Vandecasteele et al., 2014) providing another alternative mechanism. As mentioned in the previous section, running could elevate the concentration of acetylcholine (Dudar et al., 1979), setting up the network for interneuron interventions which can entrain frequencies. In my case, a lack of local excitation in the PaS (Figure 16E) could mean that PV^+ fibre activation is not sufficient to induce LFP changes and, therefore, entrainment. In contrast, freely moving animals will exhibit increased activity through cholinergic activation, but also exhibit more activity of the MS during locomotion. Interestingly, Lepperød et al. (2021) shows that activation of PV^+ fibres will disrupt phase precession, suggesting the importance of PV^+ cells for setting spike timing in the MEC. However, Schlesiger et al. (2021) could not detect a change of phase precession by PV^+ fibre stimulation but, instead, found CB^+ cells of the septum to be most important for setting the phase of spiking in the MEC. Previously, septal CB^+ were found to target low threshold spiking interneurons with a high connectivity in the MEC, making them a distinct projection compared to PV^+ cells of the MS (Fuchs et al., 2016). However, there is evidence from the rat suggesting that CB^+ is not a marker selectively expressed in GABAergic cells of the MS (Unal et al., 2015). A substantial proportion of cells (15%) express ChAT suggesting that these cells could potentially belong to a population of cells capable of GABA/ACh co-release. Therefore, more experiments addressing discrepancies between rat and mouse, but also between interneuron cell types, might be required.

One concern of a direct septal stimulation is that PV^+ cells in the MS are not a homogeneous group, fire at different phases of the θ cycle and might not be θ modulated under physiological conditions (Borhegyi et al., 2004; Unal et al., 2015; Joshi et al., 2017). Indeed, some PV^+ cells of the MS express HCN channels, making them more prone to fire bursts or to being active during θ periods (Varga et al., 2008; Hangya et al., 2009). In this study, I have shown that optogenetically identified PV^+ MS cells show different phase preferences (Figure 25C and D) which could result in an out of phase activation during optical stimulation. A failure of θ entrainment in immobile mice and data from freely moving mice and rats suggests

that fibre stimulation under different state conditions is reliable and results in similar entrainment, supporting the notion of an overall significance for PV^+ projections (Lepperød et al., 2021; Schlesiger et al., 2021).

Up to this point, not enough data is available to establish excitatory drive from cholinergic projections of the MS to the PaS or MEC and how they might be able to modulate the network. Such data could prove useful, providing further insights into how the MS might set the network state and entrain θ in cortical areas.

4.5 Implications for memory

In the experiments shown here, I have demonstrated that local PaS interneurons were specifically targeted by GABAergic projections from the MS and that the activation of MS interneurons generated entrainment even in the slow γ frequency band. It was shown in a mouse model of alzheimer's disease that θ-γ coupling is explicitly impaired, resulting in deficits during spatial learning (Etter et al., 2019). An intervention using PV^+ cell stimulation in the MS, however, could rescue the deficits and improve learning to the level of wild-type mice. With the known loss of cholinergic cells in alzheimer's disease (Davies and Maloney, 1976), the fact that not only a behavioural improvement, but also the recovery of coupling between θ and γ was detected, underlines the potential involvement of synaptic summation achieved by synchronisation. With the identification of septal targets in the PaS and the resulting outputs to the MEC, I offer a potential mechanism by which this coupling could be achieved. A synchronisation of θ along the parahippocampal axis is accomplished by disinhibition and phase locking of interneuron activity, leading to an environment primed for STDP. FS interneurons present themselves as a primary target and can generate local θ-γ coupling in cortical areas (Cardin et al., 2009; Sohal et al., 2009). Hence, deficits in interneuron entrainment could impair memory formation. Cholinergic projections of the MS, on the other hand, might support such integration of information in the cortex via disinhibition of FS cells and increased overall inhibition driven by layer I interneurons. Such a reduction in local network activity allows for an increased focus on excitatory external inputs. Additionally, I hypothesise that cholinergic modulation of pyramidal cells in the PaS and MEC can further mediate synaptic integration and support memory formation (Caruana and

Chapman, 2004; Glasgow et al., 2012). This hypothesis is supported by data from the CA1 where previous activation of the MS led to a muscarinic dependent increase of long term potentiation (LTP) at the basal dendrites (Ovsepian et al., 2004). This can be observed in running rats but will be absent during immobility (Leung et al., 2003), underlining the importance of cholinergic cells during behavioural states (Vandecasteele et al., 2014; Mamad et al., 2015). Interactions between cholinergic MS cells and GABAergic MS cells are known to be especially important for higher memory load (Roland et al., 2014), suggesting that an orchestrated interaction of cholinergic modulation and excitation with GABAergic inhibition by cells of the MS could play a crucial role in memory function.

Another study by Jacob et al. (2017) revealed that a temporal inactivation of the MS using muscimol ($GABA_A$ agonist shutting down local activity) or lesions in the MEC will impair spatial learning and distance estimation. This was tested by rats learning to associate a reward zone at a fixed distance without visual cues. Further, it was shown that θ in the MEC was abolished during MS inactivation. They hypothesised that the MS and MEC are crucial in learning distances to a reward, which can be impaired by loss of MS or MEC function. This suggests that coding for the reward zone could be mediated by septal-parahippocampal interactions and synchronisation. Evidence supporting the importance of the MS for learning distance estimation were also found in humans where hippocampal θ bursts – correlated to the distance to an object – could be observed before navigating to a target location visited in the past, suggesting a connection to memory retrieval (Bush et al., 2017). The MEC and the parahippocampal formation are major cortical inputs to the hippocampus (Köhler, 1985; Witter et al., 1989), which are important for the temporal organisation of spiking (Schlesiger et al., 2015). Therefore, setting the phase between hippocampus and MEC via the PaS by MS neurons might allow for memory formation through an increased probability of simultaneous inputs (Dickson and Curtis, 2002; Adoff et al., 2021). Addressing whether modulation of MS cells could actively change distance estimation and learning of associations between reward and locations will play a crucial role in understanding the importance of the MS and PaS in spatial memory.

4.6 Limitations of the study and outlook

Despite the insights gained into θ generation and parahippocampal circuits, there were some limitations to these experiments which should be addressed in the future. As previously discussed, recording the LFP in immobile animals in a resting state will result in less activity in the parahippocampal formation. While such an approach gives complete control over MS projections without interference of simultaneous activation of different proportion of septal cells, I was able to show that modulation of parahippocampal network activity by inhibition likely requires a basic level of parahippocampal activity. Similar findings were reported for experiments investigating cholinergic septal projections (Vandecasteele et al., 2014; Mamad et al., 2015), where behavioural states can mask potential functions. Therefore, it might be important to investigate MS GABAergic projections in other behavioural states by designing tasks in freely moving animals or in head-fixed animals in virtual reality (VR). This would allow for the same animal to be recorded during movement and immobile periods, capturing the contribution of behaviours.

Another limitation concerns channelrhodopsin which, depending on the variant, will show differences in reliability during different stimulation frequencies (Lin, 2011). Here, we used a variant (*hChR2(H134R)*) – which for our purposes of stimulation in the θ band – was sufficient but might be less reliable at frequencies over 25 Hz (Lin et al., 2009). Therefore, to further investigate a potential θ-γ coupling with optogenetic tools, faster variants should be considered. Additionally, a modulation through the activation of septal projections might not be sufficient to understand function (Carpenter et al., 2017). Hence, new inhibitory tools could be used to address shortcomings from activation using reversible deactivation of synaptic release (Bernal Sierra et al., 2018).

Similarly, some limitations occur for the *in-vitro* experiments, such as potential masking of muscarinic effects during whole-cell recordings due to wash out. Small changes could be amplified by using different intracellular solutions containing caesium and holding the cell at positive potentials. This would allow for improved detection of a hyperpolarisation via muscarinic receptors and could unmask hidden depolarisations occurring simultaneously with hyperpolarisations.

With new insights from this study, new questions can be addressed. Future ex-

periments should address the role of the MS and PaS interactions in the context of spatial memory (Poucet and Herrmann, 1990; Kesner and Giles, 1998; Liu et al., 2001; Pang et al., 2010). A task based on Jacob et al. (2017) was used in a VR setting (Tennant et al., 2018) and could be utilised to investigate the role of GABAergic projections during distance estimation. Such an approach could address whether GABAergic long-range projections can synchronise activity in the PaS and MEC in order to learn reward locations, or their involvement in path integration (Etienne and Jeffery, 2004). Path integration describes a strategy to estimate distances by integrating over the distances already travelled. This computation is thought to require different inputs such as self motion detection, including speed or acceleration and direction. Speed can control θ power (McFarland et al., 1975) and acceleration was recently shown to be affected by the θ frequency (Kropff et al., 2021). Tennant et al. (2018) has shown that, on a treadmill, animals will use motor information even when provided visual cues, suggesting a preferred method of integration. The MS, as already shown by Jacob et al. (2017), is well-positioned to relay movement information (King et al., 1998; Zhou et al., 1999), whereas the PaS, with a high density of GABAergic fibres from the MS as major output to the MEC, could significantly contribute to computation.

4.7 Conclusion

In the present study, I have demonstrated that PV^+ and $ChAT^+$ septal projection patterns to the PaS are similar to MS projections to the MEC, suggesting that projection patterns are mainly conserved throughout the parahippocampal network. They can exhibit nuanced differences such as involvement of layer I cells – a distinct group of interneurons – in inhibitory regulation of the network, or reduced activation of pyramidal cells through acetylcholine. We have provided further evidence that GABAergic MS cells play a major role in organising oscillatory activity in the θ and γ band in the PaS and MEC, but rely on an excitatory drive from up-stream regions to entrain local circuits via disinhibition. Whether the excitatory state of the network can be accomplished by the MS itself through cholinergic modulation during behavioural states or if inputs from the hippocampus are required, remains to be shown. By revealing new targets and the required network state interactions in

the MS-parahippocampal axis, we have provided further insights into understanding parahippocampal synchronisation and organisation. These insights provide the basis for new ideas for future projects, which could lead to a better understanding of parahippocampal computation and memory.

References

Aarts E, Verhage M, Veenvliet JV, Dolan CV, Sluis S van der (2014) A solution to dependency: Using multilevel analysis to accommodate nested data. Nature Neuroscience 17:491–496.

Adoff MD, Climer JR, Davoudi H, Marvin JS, Looger LL, Dombeck DA (2021) The functional organization of excitatory synaptic input to place cells. Nature Communications 12:3558.

Alonso A, Klink R (1993) Differential electroresponsiveness of stellate and pyramidal-like cells of medial entorhinal cortex layer II. J Neurophysiol 70:128–143.

Alonso A, Köhler C (1984) A study of the reciprocal connections between the septum and the entorhinal area using anterograde and retrograde axonal transport methods in the rat brain. Journal of Comparative Neurology 225:327–343.

Amaral DG, Kurz J (1985) An analysis of the origins of the cholinergic and non-cholinergic septal projections to the hippocampal formation of the rat. Journal of Comparative Neurology 240:37–59.

Amilhon B, Huh CYL, Manseau F, Ducharme G, Nichol H, Adamantidis A, Williams S (2015) Parvalbumin Interneurons of Hippocampus Tune Population Activity at Theta Frequency. Neuron 86:1277–1289.

Andersen P, Bland HB, Myhrer T, Schwartzkroin PA (1979) Septo-hippocampal pathway necessary for dentate theta production. Brain Research 165:13–22.

Arnolds DEAT, Lopes Da Silva FH, Aitink JW, Kamp A, Boeijinga P (1980) The spectral properties of hippocampal EEG related to behaviour in man. Electroencephalography and Clinical Neurophysiology 50:324–328.

Arranz P, Benoit-Bird KJ, Southall BL, Calambokidis J, Friedlaender AS, Tyack PL (2018) Risso's dolphins plan foraging dives. The Journal of Experimental Biology 221:jeb165209.

Aznar S, Qian Z, Shah R, Rahbek B, Knudsen GM (2003) The 5-HT1A serotonin receptor is located on calbindin- and parvalbumin-containing neurons in the rat

brain. Brain Research 959:58–67.

Berger H (1929) Über das Elektrenkephalogramm des Menschen. Archiv für Psychiatrie und Nervenkrankheiten 87:527–570.

Bernal Sierra YA, Rost BR, Pofahl M, Fernandes AM, Kopton RA, Moser S, Holtkamp D, Masala N, Beed P, Tukker JJ, Oldani S, Bönigk W, Kohl P, Baier H, Schneider-Warme F, Hegemann P, Beck H, Seifert R, Schmitz D (2018) Potassium channel-based optogenetic silencing. Nature Communications 9:4611.

Bjerke IE, Yates SC, Laja A, Witter MP, Puchades MA, Bjaalie JG, Leergaard TB (2021) Densities and numbers of calbindin and parvalbumin positive neurons across the rat and mouse brain. iScience 24:101906.

Bland BH, Oddie SD, Colom LV (1999) Mechanisms of Neural Synchrony in the Septohippocampal Pathways Underlying Hippocampal Theta Generation. Journal of Neuroscience 19:3223–3237.

Boccara CN, Kjonigsen LJ, Hammer IM, Bjaalie JG, Leergaard TB, Witter MP (2015) A three-plane architectonic atlas of the rat hippocampal region. Hippocampus 25:838–857.

Boccara C, Sargolini F, Thoresen V, Solstad T, Witter M, Moser E, Moser M-B (2010) Grid cells in pre- and parasubiculum. Nat Neurosci 13:nn.2602.

Bond AB, Cook RG, Lamb MR (1981) Spatial memory and the performance of rats and pigeons in the radial-arm maze. Animal Learning & Behavior 9:575–580.

Borhegyi Z, Varga V, Szilágyi N, Fabo D, Freund TFF (2004) Phase segregation of medial septal GABAergic neurons during hippocampal theta activity. J Neurosci 24:8470–8479.

Bourne JN, Harris KM (2012) Nanoscale analysis of structural synaptic plasticity. Current Opinion in Neurobiology 22:372–382.

Bragin A, Jando G, Nadasdy Z, Hetke J, Wise K, Buzsaki G (1995) Gamma (40-100 Hz) oscillation in the hippocampus of the behaving rat. Journal of Neuroscience 15:47–60.

Brandon MP, Bogaard AR, Libby CP, Connerney MA, Gupta K, Hasselmo ME (2011) Reduction of Theta Rhythm Dissociates Grid Cell Spatial Periodicity from Directional Tuning. Science 332:595–599.

Bressler SL, Coppola R, Nakamura R (1993) Episodic multiregional cortical coherence at multiple frequencies during visual task performance. Nature 366:153–156.

Brücke F, Petsche H, Pillat B, Deisenhammer E (1959) Die Beeinflussung der „Hippocampus-arousal-Reaktion“ beim Kaninchen durch elektrische Reizung im

Septum. Pflüger's Archiv für die gesamte Physiologie des Menschen und der Tiere 269:319–338.

Buchinsky FJ, Chadha NK (2017) To P or Not to P: Backing Bayesian Statistics. Otolaryngology–Head and Neck Surgery 157:915–918.

Burgalossi A, Herfst L, Moritz von H, Förste H, Haskic K, Schmidt M, Brecht M (2011) Microcircuits of Functionally Identified Neurons in the Rat Medial Entorhinal Cortex. Neuron 70:773–786.

Bush D, Bisby JA, Bird CM, Gollwitzer S, Rodionov R, Diehl B, McEvoy AW, Walker MC, Burgess N (2017) Human hippocampal theta power indicates movement onset and distance travelled. Proceedings of the National Academy of Sciences 114:12297–12302.

Buzsáki G (1989) Two-stage model of memory trace formation: A role for "noisy" brain states. Neuroscience 31:551–570.

Buzsáki G (2002) Theta Oscillations in the Hippocampus. Neuron 33:325–340.

Caballero-Bleda M, Witter MP (1993) Regional and laminar organization of projections from the presubiculum and parasubiculum to the entorhinal cortex: An anterograde tracing study in the rat. Journal of Comparative Neurology 328:115–129.

Canto C, Koganezawa N, Beed P, Moser E, Witter M (2012) All Layers of Medial Entorhinal Cortex Receive Presubicular and Parasubicular Inputs. J Neurosci 32:17620–17631.

Cardin JA, Carlén M, Meletis K, Knoblich U, Zhang F, Deisseroth K, Tsai L-H, Moore CI (2009) Driving fast-spiking cells induces gamma rhythm and controls sensory responses. Nature 459:663–667.

Carpenter B, Hoffman MD, Brubaker M, Lee D, Li P, Betancourt M (2015) The Stan Math Library: Reverse-Mode Automatic Differentiation in C++. arXiv:150907164 [cs].

Carpenter F, Burgess N, Barry C (2017) Modulating medial septal cholinergic activity reduces medial entorhinal theta frequency without affecting speed or grid coding. Sci Reports 7:14573.

Caruana D, Chapman C (2004) Stimulation of the Parasubiculum Modulates Entorhinal Cortex Responses to Piriform Cortex Inputs In Vivo. J Neurophysiol 92:1226–1235.

Chang Q, Gold PE (2004) Impaired and spared cholinergic functions in the hippocampus after lesions of the medial septum/vertical limb of the diagonal band with 192

IgG-saporin. Hippocampus 14:170–179.

Christophel TB, Klink PC, Spitzer B, Roelfsema PR, Haynes J-D (2017) The Distributed Nature of Working Memory. Trends in Cognitive Sciences 21:111–124.

Chrobak JJ, Stackman RW, Walsh TJ (1989) Intraseptal administration of muscimol produces dose-dependent memory impairments in the rat. Behavioral and Neural Biology 52:357–369.

Colgin LL (2013) Mechanisms and Functions of Theta Rhythms. Annual Review of Neuroscience 36:295–312.

Colgin LL, Denninger T, Fyhn M, Hafting T, Bonnevie T, Jensen O, Moser M-B, Moser EI (2009) Frequency of gamma oscillations routes flow of information in the hippocampus. Nature 462:353–357.

Colom L, Castaneda M, Reyna T, Hernandez S, Garrido-sanabria E (2005) Characterization of medial septal glutamatergic neurons and their projection to the hippocampus. Synapse 58:151–164.

Dacke M, Srinivasan MV (2007) Honeybee navigation: Distance estimation in the third dimension. Journal of Experimental Biology 210:845–853.

Dan Y, Poo M-M (2006) Spike Timing-Dependent Plasticity: From Synapse to Perception. Physiological Reviews 86:1033–1048.

Darwin C 1809-1882 (1859) On the origin of species by means of natural selection, or preservation of favoured races in the struggle for life. London : John Murray, 1859.

Davies P, Maloney AJ (1976) Selective loss of central cholinergic neurons in Alzheimer's disease. Lancet (London, England) 2:1403.

Dempster J (1997) A new version of the Strathclyde Electrophysiology software package running within the Microsoft Windows environment. Journal of Physiology 504:P57–P57.

Desikan S, Koser DE, Neitz A, Monyer H (2018) Target selectivity of septal cholinergic neurons in the medial and lateral entorhinal cortex. Proc Natl Acad Sci USA 115:E2644–E2652.

Dickson CT, Curtis M de (2002) Enhancement of temporal and spatial synchronization of entorhinal gamma activity by phase reset. Hippocampus 12:447–456.

Ding S-LL (2013) Comparative anatomy of the prosubiculum, subiculum, presubiculum, postsubiculum, and parasubiculum in human, monkey, and rodent. 521:4145–4162.

Dragoi G, Carpi D, Recce M, Csicsvari J, Buzsáki G (1999) Interactions between

hippocampus and medial septum during sharp waves and theta oscillation in the behaving rat. J Neurosci Official J Soc Neurosci 19:6191–6199.

Dudar JD, Whishaw IQ, Szerb JC (1979) Release of acetylcholine from the hippocampus of freely moving rats during sensory stimulation and running. Neuropharmacology 18:673–678.

Ebbesen CL, Reifenstein ET, Tang Q, Burgalossi A, Ray S, Schreiber S, Kempter R, Brecht M (2016) Cell Type-Specific Differences in Spike Timing and Spike Shape in the Rat Parasubiculum and Superficial Medial Entorhinal Cortex. Cell Reports 16:1005–1015.

Ekstrom AD, Caplan JB, Ho E, Shattuck K, Fried I, Kahana MJ (2005) Human hippocampal theta activity during virtual navigation. Hippocampus 15:881–889.

Etienne AS, Jeffery KJ (2004) Path integration in mammals. Hippocampus 14:180–192.

Etter G, Veldt S van der, Manseau F, Zarrinkoub I, Trillaud-Doppia E, Williams S (2019) Optogenetic gamma stimulation rescues memory impairments in an Alzheimer's disease mouse model. Nature Communications 10:5322.

Freund TF (1989) GABAergic septohippocampal neurons contain parvalbumin. Brain Research 478.

Freund TF, Antal M (1988) GABA-containing neurons in the septum control inhibitory interneurons in the hippocampus. Nature 336:170–173.

Frotscher M, Léránth C (1985) Cholinergic innervation of the rat hippocampus as revealed by choline acetyltransferase immunocytochemistry: A combined light and electron microscopic study. Journal of Comparative Neurology 239:237–246.

Fuchs EC, Neitz A, Pinna R, Melzer S, Caputi A, Monyer H (2016) Local and Distant Input Controlling Excitation in Layer II of the Medial Entorhinal Cortex. Neuron 89:194–208.

Fuentemilla L, Penny WD, Cashdollar N, Bunzeck N, Düzel E (2010) Theta-Coupled Periodic Replay in Working Memory. Current Biology 20:606–612.

Fuhrmann F, Justus D, Sosulina L, Kaneko H, Beutel T, Friedrichs D, Schoch S, Schwarz MK, Fuhrmann M, Remy S (2015) Locomotion, Theta Oscillations, and the Speed-Correlated Firing of Hippocampal Neurons Are Controlled by a Medial Septal Glutamatergic Circuit. Neuron 86:1253–1264.

Funahashi M, Stewart M (1997) Presubicular and parasubicular cortical neurons of the rat: Electrophysiological and morphological properties. Hippocampus 7:117–129.

Gabry J, Simpson D, Vehtari A, Betancourt M, Gelman A (2019) Visualization in Bayesian workflow. Journal of the Royal Statistical Society: Series A (Statistics in Society) 182:389–402.

Gaspar P, Berger B, Lesur A, Borsotti JP, Febvret A (1987) Somatostatin 28 and neuropeptide Y innervation in the septal area and related cortical and subcortical structures of the human brain. Distribution, relationships and evidence for differential coexistence. Neuroscience 22:49–73.

Gaykema RPA, Luiten PGM, Nyakas C, Traber J (1990) Cortical projection patterns of the medial septum-diagonal band complex. Journal of Comparative Neurology 293:103–124.

Geiger JRP, Jonas P (2000) Dynamic Control of Presynaptic Ca2+ Inflow by Fast-Inactivating K+ Channels in Hippocampal Mossy Fiber Boutons. Neuron 28:927–939.

Gelman A (2006) Multilevel (Hierarchical) Modeling: What It Can and Cannot Do. Technometrics 48:432–435.

Gerashchenko D, Salin-Pascual R, Shiromani PJ (2001) Effects of hypocretin–saporin injections into the medial septum on sleep and hippocampal theta. Brain Research 913:106–115.

Giocomo LM, Hasselmo ME (2008) Time Constants of h Current in Layer II Stellate Cells Differ along the Dorsal to Ventral Axis of Medial Entorhinal Cortex. Journal of Neuroscience 28:9414–9425.

Giocomo LM, Zilli EA, Fransén E, Hasselmo ME (2007) Temporal Frequency of Subthreshold Oscillations Scales with Entorhinal Grid Cell Field Spacing. Science 315:1719–1722.

Glanzman DL (2010) Common Mechanisms of Synaptic Plasticity in Vertebrates and Invertebrates. Current Biology 20:R31–R36.

Glasgow SD, Chapman CA (2007) Local Generation of Theta-Frequency EEG Activity in the Parasubiculum. Journal of Neurophysiology 97:3868–3879.

Glasgow SD, Chapman CA (2008) Conductances Mediating Intrinsic Theta-Frequency Membrane Potential Oscillations in Layer II Parasubicular Neurons. Journal of Neurophysiology 100:2746–2756.

Glasgow SD, Chapman CA (2013) Muscarinic Depolarization of Layer II Neurons of the Parasubiculum. PLOS ONE 8:e58901.

Glasgow SD, Glovaci I, Karpowicz LS, Chapman CA (2012) Cholinergic suppression of excitatory synaptic transmission in layers II/III of the parasubiculum. Neuro-

science 201:1–11.

Gogolák G, Stumpf Ch, Petsche H, Šterc J (1968) The firing pattern of septal neurons and the form of the hippocampal theta wave. Brain Research 7:201–207.

Gonzalez-Sulser A, Parthier D, Candela A, McClure C, Pastoll H, Garden D, Sürmeli G, Nolan MF (2014) GABAergic projections from the medial septum selectively inhibit interneurons in the medial entorhinal cortex. J Neurosci 34:16739–16743.

Goutagny R, Jackson J, Williams S (2009) Self-generated theta oscillations in the hippocampus. Nat Neurosci 12:1491–1493.

Green JD, Arduini AA (1954) Hippocampal electrical activity in arousal. Journal of Neurophysiology 17:533–557.

Groen T van, Wyss J (1990) The connections of presubiculum and parasubiculum in the rat. Brain Res 518:227–243.

Hamam BN, Sinai M, Poirier G, Chapman CA (2007) Cholinergic suppression of excitatory synaptic responses in layer II of the medial entorhinal cortex. Hippocampus 17:103–113.

Hangya B, Borhegyi Z, Szilágyi N, Freund TF, Varga V (2009) GABAergic Neurons of the Medial Septum Lead the Hippocampal Network during Theta Activity. Journal of Neuroscience 29:8094–8102.

Hazan L, Zugaro M, Buzsáki G (2006) Klusters, NeuroScope, NDManager: A free software suite for neurophysiological data processing and visualization. Journal of Neuroscience Methods 155:207–216.

Hebb DO (1949) The organization of behavior; a neuropsychological theory. Oxford, England: Wiley.

Hentschke H, Perkins MG, Pearce RA, Banks MI (2007) Muscarinic blockade weakens interaction of gamma with theta rhythms in mouse hippocampus. European Journal of Neuroscience 26:1642–1656.

Herreras O (2016) Local Field Potentials: Myths and Misunderstandings. Frontiers in Neural Circuits 10:101.

Heys JG, Hasselmo ME (2012) Neuromodulation of Ih in Layer II Medial Entorhinal Cortex Stellate Cells: A Voltage-Clamp Study. Journal of Neuroscience 32:9066–9072.

Heys JG, Schultheiss NW, Shay CF, Tsuno Y, Hasselmo ME (2012) Effects of acetylcholine on neuronal properties in entorhinal cortex. Front Behav Neurosci 6:32.

Huang Y-Y, Kandel ER (2005) Theta stimulation up-regulates the synaptic strength of the pathway from CA1 to subiculum region of hippocampus. Proceedings of

the National Academy of Sciences 102:232–237.

Huerta PT, Lisman JE (1995) Bidirectional synaptic plasticity induced by a single burst during cholinergic theta oscillation in CA1 in vitro. Neuron 15:1053–1063.

Hydén H, Lange PW (1968) Protein Synthesis in the Hippocampal Pyramidal Cells of Rats during a Behavioral Test. Science 159:1370–1373.

Jacob P-YY, Marta G-S, Facchini J, Poucet B, Save E, Sargolini F (2017) Medial entorhinal cortex and medial septum contribute to self-motion-based linear distance estimation. Brain Struct Funct 222:2727–2742.

Jensen O, Lisman JE (1996) Hippocampal CA3 region predicts memory sequences: Accounting for the phase precession of place cells. Learning & Memory 3:279–287.

Jensen O, Tesche CD (2002) Frontal theta activity in humans increases with memory load in a working memory task. European Journal of Neuroscience 15:1395–1399.

Jiang X, Shen S, Cadwell CR, Berens P, Sinz F, Ecker AS, Patel S, Tolias AS (2015) Principles of connectivity among morphologically defined cell types in adult neocortex. Science.

Johnson DA, Zambon NJ, Gibbs RB (2002) Selective lesion of cholinergic neurons in the medial septum by 192 IgG-saporin impairs learning in a delayed matching to position T-maze paradigm. Brain Research 943:132–141.

Joshi A, Salib M, Viney TJ, Dupret D, Somogyi P (2017) Behavior-Dependent Activity and Synaptic Organization of Septo-hippocampal GABAergic Neurons Selectively Targeting the Hippocampal CA3 Area. Neuron 96:1342–1357.e5.

Jung R, Kornmüller AE (1938) A method of recording localized electrical potentials in subcortical regions of the brain. Archiv für Psychiatrie und Nervenkrankheiten 109:1–30.

Justus D, Dalügge D, Bothe S, Fuhrmann F, Hannes C, Kaneko H, Friedrichs D, Sosulina L, Schwarz I, Elliott DA, Schoch S, Bradke F, Schwarz MK, Remy S (2017) Glutamatergic synaptic integration of locomotion speed via septoentorhinal projections. Nature Neuroscience 20:16–19.

Kajikawa Y, Schroeder CE (2011) How Local Is the Local Field Potential? Neuron 72:847–858.

Katahira K (2016) How hierarchical models improve point estimates of model parameters at the individual level. Journal of Mathematical Psychology 73:37–58.

Kesner R, Giles R (1998) Neural circuit analysis of spatial working memory: Role of pre- and parasubiculum, medial and lateral entorhinal cortex. Hippocampus 8:416–423.

Kim IS, Dickinson MH (2017) Idiothetic Path Integration in the Fruit Fly Drosophila melanogaster. Current Biology 27:2227–2238.e3.

King C, Recce M, O'Keefe J (1998) The rhythmicity of cells of the medial septum/diagonal band of Broca in the awake freely moving rat: Relationships with behaviour and hippocampal theta. European Journal of Neuroscience 10:464–477.

Kitamura T, Pignatelli M, Suh J, Kohara K, Yoshiki A, Abe K, Tonegawa S (2014) Island Cells Control Temporal Association Memory. Science 343:896–901.

Kocsis B, Bragin A, Buzsáki G (1999) Interdependence of Multiple Theta Generators in the Hippocampus: A Partial Coherence Analysis. Journal of Neuroscience 19:6200–6212.

Koenig J, Lecourtier L, Cosquer B, Pereira PM, Cassel J-C (2011) Spatial memory alterations by activation of septal 5HT1A receptors: No implication of cholinergic septohippocampal neurons. Psychopharmacology 214:437–454.

Köhler C (1985) Intrinsic projections of the retrohippocampal region in the rat brain. I. The subicular complex. J Comp Neurol 236:504–522.

Kornienko O, Latuske P, Bassler M, Kohler L, Allen K (2018) Non-rhythmic head-direction cells in the parahippocampal region are not constrained by attractor network dynamics Frank MJ, Burgess N, Peyrache A, O'Mara SM, Jeffery KJ, eds. eLife 7:e35949.

Kramis R, Vanderwolf CH, Bland BH (1975) Two types of hippocampal rhythmical slow activity in both the rabbit and the rat: Relations to behavior and effects of atropine, diethyl ether, urethane, and pentobarbital. Experimental Neurology 49:58–85.

Kropff E, Carmichael JE, Moser EI, Moser M-B (2021) Frequency of theta rhythm is controlled by acceleration, but not speed, in running rats. Neuron 109:1029–1039.e8.

Kruschke JK (2015) Doing Bayesian data analysis: A tutorial with R, JAGS, and Stan, Edition 2. Boston: Academic Press.

Lamour Y, Dutar P, Jobert A (1984) Septo-hippocampal and other medial septum-diagonal band neurons: Electrophysiological and pharmacological properties. Brain Research 309:217–226.

Lee EHY, Lin YP, Yin TH (1988) Effects of lateral and medial septal lesions on various activity and reactivity measures in rats. Physiology & Behavior 42:97–102.

Lee H, Simpson GV, Logothetis NK, Rainer G (2005) Phase Locking of Single Neuron Activity to Theta Oscillations during Working Memory in Monkey Extrastriate

Visual Cortex. Neuron 45:147–156.

Lepperød ME, Christensen AC, Lensjø KK, Buccino AP, Yu J, Fyhn M, Hafting T (2021) Optogenetic pacing of medial septum parvalbumin-positive cells disrupts temporal but not spatial firing in grid cells. Science Advances 7:eabd5684.

Leung LS, Shen B, Rajakumar N, Ma J (2003) Cholinergic Activity Enhances Hippocampal Long-Term Potentiation in CA1 during Walking in Rats. Journal of Neuroscience 23:9297–9304.

Liebe S, Hoerzer GM, Logothetis NK, Rainer G (2012) Theta coupling between V4 and prefrontal cortex predicts visual short-term memory performance. Nature Neuroscience 15:456–462.

Lin JY (2011) A user's guide to channelrhodopsin variants: Features, limitations and future developments. Experimental Physiology 96:19–25.

Lin JY, Lin MZ, Steinbach P, Tsien RY (2009) Characterization of Engineered Channelrhodopsin Variants with Improved Properties and Kinetics. Biophysical Journal 96:1803–1814.

Liu P, Jarrard LE, Bilkey DK (2001) Excitotoxic lesions of the pre- and parasubiculum disrupt object recognition and spatial memory processes. Behavioral Neuroscience 115:112–124.

Liu P, Jarrard LE, Bilkey DK (2004) Excitotoxic lesions of the pre- and parasubiculum disrupt the place fields of hippocampal pyramidal cells. Hippocampus 14:107–116.

Lüttgen M, Ögren SO, Meister B (2004) Chemical identity of 5-HT2A receptor immunoreactive neurons of the rat septal complex and dorsal hippocampus. Brain Research 1010:156–165.

Lüttgen M, Ögren SO, Meister B (2005) 5-HT1A receptor mRNA and immunoreactivity in the rat medial septum/diagonal band of Broca—relationships to GABAergic and cholinergic neurons. Journal of Chemical Neuroanatomy 29:93–111.

Luuk H, Koks S, Plaas M, Hannibal J, Rehfeld J, Vasar E (2008) Distribution of Wfs1 protein in the central nervous system of the mouse and its relation to clinical symptoms of the Wolfram syndrome. J Comp Neurol 509:642–660.

Ma X, Zhang Y, Wang L, Li N, Barkai E, Zhang X, Lin L, Xu J (2020) The Firing of Theta State-Related Septal Cholinergic Neurons Disrupt Hippocampal Ripple Oscillations via Muscarinic Receptors. Journal of Neuroscience 40:3591–3603.

Makowski D, Ben-Shachar MS, Chen SHA, Lüdecke D (2019) Indices of Effect Existence and Significance in the Bayesian Framework. Frontiers in Psychology 10:2767.

Mamad O, McNamara H, Reilly R, Tsanov M (2015) Medial septum regulates the hippocampal spatial representation. Frontiers in Behavioral Neuroscience 9:166.

Manseau F, Goutagny R, Danik M, Williams S (2008) The Hippocamposeptal Pathway Generates Rhythmic Firing of GABAergic Neurons in the Medial Septum and Diagonal Bands: An Investigation Using a Complete Septohippocampal Preparation In Vitro. The Journal of Neuroscience 28:4096–4107.

Markram H, Lübke J, Frotscher M, Sakmann B (1997) Regulation of Synaptic Efficacy by Coincidence of Postsynaptic APs and EPSPs. Science 275:213–215.

Martínez JJ, Rahsepar B, White JA (2017) Anatomical and Electrophysiological Clustering of Superficial Medial Entorhinal Cortex Interneurons. eNeuro 4.

McFarland WL, Teitelbaum H, Hedges EK (1975) Relationship between hippocampal theta activity and running speed in the rat. Journal of Comparative and Physiological Psychology 88:324–328.

Mehta MR, Barnes CA, McNaughton BL (1997) Experience-dependent, asymmetric expansion of hippocampal place fields. Proceedings of the National Academy of Sciences of the United States of America 94:8918–8921.

Melzer S, Michael M, Caputi A, Eliava M, Fuchs E, Whittington M, Monyer H (2012) Long-Range–Projecting GABAergic Neurons Modulate Inhibition in Hippocampus and Entorhinal Cortex. Science 335:1506–1510.

Mesulam MM (1998) From sensation to cognition. Brain 121:1013–1052.

Miller J et al. (2018) Lateralized hippocampal oscillations underlie distinct aspects of human spatial memory and navigation. Nature Communications 9:2423.

Mizumori SJY, Perez GM, Alvarado MC, Barnes CA, McNaughton BL (1990) Reversible inactivation of the medial septum differentially affects two forms of learning in rats. Brain Research 528:12–20.

Morris RGM, Garrud P, Rawlins JNP, O'Keefe J (1982) Place navigation impaired in rats with hippocampal lesions. Nature 297:681–683.

Mulders WHaM, West MJ, Slomianka L (1997) Neuron numbers in the presubiculum, parasubiculum, and entorhinal area of the rat. Journal of Comparative Neurology 385:83–94.

Müller C, Remy S (2018) Septo–hippocampal interaction. Cell and Tissue Research 373:565–575.

Nassar M, Simonnet J, Lofredi R, Cohen I, Savary E, Yanagawa Y, Miles R, Fricker D (2015) Diversity and overlap of parvalbumin and somatostatin expressing interneurons in mouse presubiculum. Front Neural Circuit 9:20.

Neuser K, Triphan T, Mronz M, Poeck B, Strauss R (2008) Analysis of a spatial orientation memory in Drosophila. Nature 453:1244–1247.

Newman EL, Gillet SN, Climer JR, Hasselmo ME (2013) Cholinergic Blockade Reduces Theta-Gamma Phase Amplitude Coupling and Speed Modulation of Theta Frequency Consistent with Behavioral Effects on Encoding. Journal of Neuroscience 33:19635–19646.

Nilsson OG, Kalén P, Rosengren E, Björklund A (1990) Acetylcholine release in the rat hippocampus as studied by microdialysis is dependent on axonal impulse flow and increases during behavioural activation. Neuroscience 36:325–338.

O'Keefe J (1976) Place units in the hippocampus of the freely moving rat. Experimental Neurology 51:78–109.

O'Keefe J, Conway DH (1978) Hippocampal place units in the freely moving rat: Why they fire where they fire. Experimental Brain Research 31:573–590.

O'Keefe J, Dostrovsky J (1971) The hippocampus as a spatial map. Preliminary evidence from unit activity in the freely-moving rat. Brain Research 34:171–175.

O'Keefe J, Recce ML (1993) Phase relationship between hippocampal place units and the EEG theta rhythm. Hippocampus 3:317–330.

O'Keefe, Burgess (1999) Theta activity, virtual navigation and the human hippocampus. Trends in cognitive sciences 3:403–406.

Oláh S, Komlósi G, Szabadics J, Varga C, Tóth É, Barzó P, Tamás G (2007) Output of Neurogliaform Cells to Various Neuron Types in the Human and Rat Cerebral Cortex. Frontiers in Neural Circuits 1:4.

Olson DJ, Maki WS (1983) Characteristics of spatial memory in pigeons. Journal of Experimental Psychology: Animal Behavior Processes 9:266–280.

Ovsepian SV, Anwyl R, Rowan MJ (2004) Endogenous acetylcholine lowers the threshold for long-term potentiation induction in the CA1 area through muscarinic receptor activation: In vivo study. European Journal of Neuroscience 20:1267–1275.

Pabst M, Braganza O, Dannenberg H, Hu W, Pothmann L, Rosen J, Mody I, Loo K van, Deisseroth K, Becker AJ, Schoch S, Beck H (2016) Astrocyte Intermediaries of Septal Cholinergic Modulation in the Hippocampus. Neuron 90:853–865.

Pachitariu M, Steinmetz NA, Kadir SN, Carandini M, Harris KD (2016) Fast and accurate spike sorting of high-channel count probes with KiloSort. In: Advances in Neural Information Processing Systems (Lee D, Sugiyama M, Luxburg U, Guyon I, Garnett R, eds). Curran Associates, Inc.

Pang KCH, Jiao X, Sinha S, Beck KD, Servatius RJ (2010) Damage of GABAergic neurons in the medial septum impairs spatial working memory and extinction of active avoidance: Effects on proactive interference. Hippocampus 21:n/a–n/a.

Pascale Simon A, Poindessous-Jazat F, Dutar P, Epelbaum J, Bassant M-H (2006) Firing Properties of Anatomically Identified Neurons in the Medial Septum of Anesthetized and Unanesthetized Restrained Rats. The Journal of Neuroscience 26:9038–9046.

Pastoll H, Ramsden HL, Nolan MF (2012) Intrinsic electrophysiological properties of entorhinal cortex stellate cells and their contribution to grid cell firing fields. Front Neural Circuit 6:17.

Petsche H, Stumpf Ch, Gogolak G (1962) The significance of the rabbit's septum as a relay station between the midbrain and the hippocampus I. The control of hippocampus arousal activity by the septum cells. Electroencephalography and Clinical Neurophysiology 14:202–211.

Poucet B, Herrmann T (1990) Septum and medial frontal cortex contribution to spatial problem-solving. Behavioural Brain Research 37:269–280.

Poulter S, Hartley T, Lever C (2018) The Neurobiology of Mammalian Navigation. Current Biology 28:R1023–R1042.

R Core Team (2021) R: A language and environment for statistical computing. Vienna, Austria: R Foundation for Statistical Computing.

Raisman G (1966) The connexions of the septum. Brain: A Journal of Neurology 89:317–348.

Ramsden HL, Sürmeli G, G M Steven, Nolan MF (2015) Laminar and Dorsoventral Molecular Organization of the Medial Entorhinal Cortex Revealed by Large-scale Anatomical Analysis of Gene Expression. Plos Comput Biol 11:e1004032.

Rawlins JNP, Feldon J, Gray JA (1979) Septo-hippocampal connections and the hippocampal theta rhythm. Experimental Brain Research 37:49–63.

Ray S, Naumann R, Burgalossi A, Tang Q, Schmidt H, Brecht M (2014) Grid-layout and theta-modulation of layer 2 pyramidal neurons in medial entorhinal cortex. Science 343:891–896.

Reifenstein ET, Kempter R, Schreiber S, Stemmler MB, Herz AVM (2012) Grid cells in rat entorhinal cortex encode physical space with independent firing fields and phase precession at the single-trial level. Proceedings of the National Academy of Sciences 109:6301–6306.

Robinson JK, Wenk GL, Wiley RG, Lappi DA, Crawley JN (1996) 192IgG-Saporin im-

munotoxin and ibotenic acid lesions of nucleus basalis and medial septum produce comparable deficits on delayed nonmatching to position in rats. Psychobiology 24:179–186.

Robinson J, Manseau F, Ducharme G, Amilhon B, Vigneault E, Mestikawy SE, Williams S (2016) Optogenetic Activation of Septal Glutamatergic Neurons Drive Hippocampal Theta Rhythms. Journal of Neuroscience 36:3016–3023.

Roland JJ, Stewart AL, Janke KL, Gielow MR, Kostek JA, Savage LM, Servatius RJ, Pang KCH (2014) Medial Septum-Diagonal Band of Broca (MSDB) GABAergic Regulation of Hippocampal Acetylcholine Efflux Is Dependent on Cognitive Demands. Journal of Neuroscience 34:506–514.

Rossant C, Kadir SN, Goodman DFM, Schulman J, Hunter MLD, Saleem AB, Grosmark A, Belluscio M, Denfield GH, Ecker AS, Tolias AS, Solomon S, Buzsáki G, Carandini M, Harris KD (2016) Spike sorting for large, dense electrode arrays. Nature Neuroscience 19:634–641.

Roux L, Stark E, Sjulson L, Buzsáki G (2014) In vivo optogenetic identification and manipulation of GABAergic interneuron subtypes. Current Opinion in Neurobiology 26:88–95.

Rowland D, Weible A, Wickersham I, Wu H, Mayford M, Witter M, Kentros C (2013) Transgenically Targeted Rabies Virus Demonstrates a Major Monosynaptic Projection from Hippocampal Area CA2 to Medial Entorhinal Layer II Neurons. J Neurosci 33:14889–14898.

Salib M, Joshi A, Katona L, Howarth M, Micklem B, Somogyi P, Viney TJ (2019) GABAergic medial septal neurons with low-rhythmic firing innervating the dentate gyrus and hippocampal area CA3. The Journal of neuroscience : the official journal of the Society for Neuroscience 39:4527–4549.

Salkoff DB, Zagha E, Yuzgec O, McCormick DA (2015) Synaptic Mechanisms of Tight Spike Synchrony at Gamma Frequency in Cerebral Cortex. Journal of Neuroscience 35:10236–10251.

Sammons RP, Parthier D, Stumpf A, Schmitz D (2019) Electrophysiological and Molecular Characterization of the Parasubiculum. The Journal of Neuroscience: The Official Journal of the Society for Neuroscience 39:8860–8876.

Sammons RP, Tzilivaki A, Schmitz D (2021) Local Microcircuitry of PaS Shows Distinct and Common Features of Excitatory and Inhibitory Connectivity. Cerebral Cortex (New York, NY: 1991):bhab195.

Sarnthein J, Petsche H, Rappelsberger P, Shaw GL, Stein A von (1998) Synchroniza-

tion between prefrontal and posterior association cortex during human working memory. Proceedings of the National Academy of Sciences 95:7092–7096.

Schlesiger M, Cannova C, Boublil B, Hales J, Mankin E, Brandon M, Leutgeb J, Leibold C, Leutgeb S (2015) The medial entorhinal cortex is necessary for temporal organization of hippocampal neuronal activity. Nat Neurosci 18:nn.4056.

Schlesiger MI, Ruff T, MacLaren DAA, Barriuso-Ortega I, Saidov KM, Yen T-Y, Monyer H (2021) Two septal-entorhinal GABAergic projections differentially control coding properties of spatially tuned neurons in the medial entorhinal cortex. Cell Reports 34:108801.

Schlosser G (2018) A Short History of Nearly Every Sense—The Evolutionary History of Vertebrate Sensory Cell Types. Integrative and Comparative Biology 58:301–316.

Schoot R van de, Depaoli S, King R, Kramer B, Märtens K, Tadesse MG, Vannucci M, Gelman A, Veen D, Willemsen J, Yau C (2021) Bayesian statistics and modelling. Nature Reviews Methods Primers 1:1–26.

Serafin M, Williams S, Khateb A, Fort P, Mühlethaler M (1996) Rhythmic firing of medial septum non-cholinergic neurons. Neuroscience 75:671–675.

signal developers (2014) Signal: Signal processing.

Skaggs WE, McNaughton BL, Wilson MA, Barnes CA (1996) Theta phase precession in hippocampal neuronal populations and the compression of temporal sequences. Hippocampus 6:149–172.

Sohal VS, Zhang F, Yizhar O, Deisseroth K (2009) Parvalbumin neurons and gamma rhythms enhance cortical circuit performance. Nature 459:698–702.

Soltesz I, Deschenes M (1993) Low- and high-frequency membrane potential oscillations during theta activity in CA1 and CA3 pyramidal neurons of the rat hippocampus under ketamine-xylazine anesthesia. Journal of Neurophysiology 70:97–116.

Sotty F, Danik M, Manseau F, Laplante F, Quirion R, Williams S (2003) Distinct electrophysiological properties of glutamatergic, cholinergic and GABAergic rat septohippocampal neurons: Novel implications for hippocampal rhythmicity. The Journal of Physiology 551:927–943.

Sparks DW, Chapman CA (2014) Contribution of Ih to the relative facilitation of synaptic responses induced by carbachol in the entorhinal cortex during repetitive stimulation of the parasubiculum. Neuroscience 278:81–92.

Stark E, Eichler R, Roux L, Fujisawa S, Rotstein HG, Buzsáki G (2013) Inhibition-

Induced Theta Resonance in Cortical Circuits. Neuron 80:1263–1276.

Sunkin SM, Ng L, Lau C, Dolbeare T, Gilbert TL, Thompson CL, Hawrylycz M, Dang C (2013) Allen Brain Atlas: An integrated spatio-temporal portal for exploring the central nervous system. Nucleic Acids Research 41:D996–D1008.

Swanson LW, Cowan WM (1977) An autoradiographic study of the organization of the efferet connections of the hippocampal formation in the rat. Journal of Comparative Neurology 172:49–84.

Swanson LW, Cowan WM (1979) The connections of the septal region in the rat. Journal of Comparative Neurology 186:621–655.

Tang Q, Burgalossi A, Ebbesen CL, Sanguinetti-Scheck JI, Schmidt H, Tukker JJ, Naumann R, Ray S, Preston-Ferrer P, Schmitz D, Brecht M (2016) Functional Architecture of the Rat Parasubiculum. Journal of Neuroscience 36:2289–2301.

Taube JS (1995) Place cells recorded in the parasubiculum of freely moving rats. Hippocampus 5:569–583.

Tennant SA, Fischer L, Garden DLF, Gerlei KZ, Martinez-Gonzalez C, McClure C, Wood ER, Nolan MF (2018) Stellate Cells in the Medial Entorhinal Cortex Are Required for Spatial Learning. Cell Reports 22:1313–1324.

Tingley D, Buzsáki G (2018) Transformation of a Spatial Map across the Hippocampal-Lateral Septal Circuit. Neuron 98:1229–1242.e5.

Tolman EC (1948) Cognitive maps in rats and men. Psychological Review 55:189–208.

Tsoar A, Nathan R, Bartan Y, Vyssotski A, Dell'Omo G, Ulanovsky N (2011) Large-scale navigational map in a mammal. Proceedings of the National Academy of Sciences 108:E718–E724.

Unal G, Joshi A, Viney TJ, Kis V, Somogyi P (2015) Synaptic Targets of Medial Septal Projections in the Hippocampus and Extrahippocampal Cortices of the Mouse. J Neurosci 35:15812–15826.

Vandecasteele M, Varga V, Berényi A, Papp E, Barthó P, Venance L, Freund TFF, Buzsáki G (2014) Optogenetic activation of septal cholinergic neurons suppresses sharp wave ripples and enhances theta oscillations in the hippocampus. Proc Natl Acad Sci USA 111:13535–13540.

Vanderwolf CH (1969) Hippocampal electrical activity and voluntary movement in the rat. Electroencephalography and Clinical Neurophysiology 26:407–418.

Varela F, Lachaux J-P, Rodriguez E, Martinerie J (2001) The brainweb: Phase synchronization and large-scale integration. Nature Reviews Neuroscience 2:229–239.

Varga V, Hangya B, Kránitz K, Ludányi A, Zemankovics R, Katona I, Shigemoto R,

Freund TF, Borhegyi Z (2008) The presence of pacemaker HCN channels identifies theta rhythmic GABAergic neurons in the medial septum. The Journal of Physiology 586:3893–3915.

Vehtari A, Gelman A, Gabry J (2017) Practical Bayesian model evaluation using leave-one-out cross-validation and WAIC. Statistics and Computing 27:1413–1432.

Viney TJ, Salib M, Joshi A, Unal G, Berry N, Somogyi P (2018) Shared rhythmic subcortical GABAergic input to the entorhinal cortex and presubiculum. Elife 7:e34395.

Walsh TJ, Herzog CD, Gandhi C, Stackman RW, Wiley RG (1996) Injection of IgG 192-saporin into the medial septum produces cholinergic hypofunction and dose-dependent working memory deficits. Brain Research 726:69–79.

Ward JH (1963) Hierarchical Grouping to Optimize an Objective Function. Journal of the American Statistical Association 58:236–244.

Watrous AJ, Lee DJ, Izadi A, Gurkoff GG, Shahlaie K, Ekstrom AD (2013) A comparative study of human and rat hippocampal low-frequency oscillations during spatial navigation: Comparison of Human and Rodent Theta. Hippocampus 23:656–661.

Wehner R (2003) Desert ant navigation: How miniature brains solve complex tasks. Journal of Comparative Physiology A: Sensory, Neural, and Behavioral Physiology 189:579–588.

Winson J (1974) Patterns of hippocampal theta rhythm in the freely moving rat. Electroencephalography and Clinical Neurophysiology 36:291–301.

Winson J (1978) Loss of hippocampal theta rhythm results in spatial memory deficit in the rat. Science (New York, NY) 201:160–163.

Witter MP, Canto CB, Couey JJ, Koganezawa N, C O Kally (2014) Architecture of spatial circuits in the hippocampal region. Philos Trans R Soc Lond, B, Biol Sci 369:20120515.

Witter MP, Hoesen GV, Amaral DG (1989) Topographical organization of the entorhinal projection to the dentate gyrus of the monkey. Journal of Neuroscience 9:216–228.

Wozny C, Williams SR (2011) Specificity of Synaptic Connectivity between Layer 1 Inhibitory Interneurons and Layer 2/3 Pyramidal Neurons in the Rat Neocortex. Cerebral Cortex 21:1818–1826.

Xu C, Datta S, Wu M, Alreja M (2004) Hippocampal theta rhythm is reduced by suppression of the H-current in septohippocampal GABAergic neurons. European

Journal of Neuroscience 19:2299–2309.

Záborszky L, Gombkoto P, Varsanyi P, Gielow MR, Poe G, Role LW, Ananth M, Rajebhosale P, Talmage DA, Hasselmo ME, Dannenberg H, Minces VH, Chiba AA (2018) Specific Basal Forebrain–Cortical Cholinergic Circuits Coordinate Cognitive Operations. Journal of Neuroscience 38:9446–9458.

Zhang S-J, Ye J, Miao C, Tsao A, Cerniauskas I, Ledergerber D, Moser M-B, Moser EI (2013) Optogenetic Dissection of Entorhinal-Hippocampal Functional Connectivity. Science 340:1232627.

Zhou TL, Tamura R, Kuriwaki J, Ono T (1999) Comparison of medial and lateral septal neuron activity during performance of spatial tasks in rats. Hippocampus 9:220–234.

Appendix

Additional tables

Table 1: *Cell Parameters*

		HDI		
Parameter	Cell Type	2.5%	50%	97.5%
AHP (mV)	DS	10.383	16.626	22.989
	FS	15.334	23.892	32.977
	IN	10.919	19.749	28.516
	IN-L1	8.497	17.953	27.209
AP-Height (mV)	DS	56.718	72.004	85.606
	FS	41.815	65.065	89.373
	IN	37.891	61.749	84.893
	IN-L1	36.062	60.022	82.952
Adaptation	DS	0.034	0.908	4.596
	FS	0.015	0.964	5.357
	IN	0.019	0.928	4.787
	IN-L1	0.025	0.914	4.431
Cm (pF)	DS	51.115	134.615	242.936
	FS	28.448	101.196	196.491
	IN	19.292	71.346	147.839
	IN-L1	10.829	50.242	105.415
FWHM (ms)	DS	0.343	0.587	0.858
	FS	0.105	0.300	0.553
	IN	0.208	0.515	0.856
	IN-L1	0.330	0.621	0.957
Firing Frequency (Hz)	DS	26.000	65.000	120.000
	FS	50.000	196.000	408.000
	IN	39.000	121.000	218.000
	IN-L1	37.000	81.000	144.000

Table 1: *Cell Parameters*

		HDI		
Parameter	Cell Type	2.5%	50%	97.5%
Gain (Spikes/pA)	DS	0.063	0.287	0.599
	FS	0.182	0.830	1.786
	IN	0.128	0.563	1.259
	IN-L1	0.123	0.577	1.263
ISI 1/2 (s)	DS	0.019	0.058	0.118
	FS	0.001	0.020	0.080
	IN	0.001	0.028	0.123
	IN-L1	0.003	0.034	0.117
ISI 9/10 (s)	DS	0.022	0.052	0.093
	FS	0.002	0.019	0.063
	IN	0.003	0.027	0.090
	IN-L1	0.006	0.031	0.080
ISI min (s)	DS	0.014	0.040	0.085
	FS	0.003	0.012	0.027
	IN	0.005	0.018	0.044
	IN-L1	0.006	0.022	0.049
Latency (s)	DS	0.027	0.135	0.291
	FS	0.000	0.060	0.302
	IN	0.000	0.065	0.258
	IN-L1	0.000	0.065	0.239
Negative Slope (V/ms)	DS	-0.193	-0.120	-0.064
	FS	-0.705	-0.366	-0.111
	IN	-0.264	-0.135	-0.044
	IN-L1	-0.153	-0.090	-0.039
Positive Slope (V/ms)	DS	0.146	0.314	0.500
	FS	0.149	0.440	0.806
	IN	0.087	0.249	0.472
	IN-L1	0.091	0.209	0.360
Rheobase (pA)	DS	29.774	118.964	243.874
	FS	98.417	384.957	762.927
	IN	16.675	128.971	309.812
	IN-L1	19.343	129.790	308.746
Rin (MOhm)	DS	41.373	96.844	169.976
	FS	23.486	55.778	95.013
	IN	51.794	142.732	257.349
	IN-L1	48.665	138.088	253.781

Table 1: *Cell Parameters*

		HDI		
Parameter	Cell Type	2.5%	50%	97.5%
Sag Ratio	DS	0.706	0.866	0.984
	FS	0.785	0.889	0.967
	IN	0.789	0.908	0.990
	IN-L1	0.808	0.912	0.988
Slope Ratio	DS	1.344	2.563	4.053
	FS	0.705	1.182	1.754
	IN	1.026	1.814	2.718
	IN-L1	1.289	2.284	3.375
Threshold (mV)	DS	-41.681	-34.823	-28.289
	FS	-49.354	-36.950	-25.750
	IN	-45.156	-33.974	-22.211
	IN-L1	-46.455	-33.201	-20.528
Vm (mV)	DS	-80.450	-69.755	-59.076
	FS	-79.914	-69.919	-59.714
	IN	-79.689	-69.545	-58.732
	IN-L1	-80.473	-69.732	-58.816
mAHP (mV)	DS	-0.069	-0.027	0.000
	FS	-0.011	-0.005	0.000
	IN	-0.033	-0.012	0.000
	IN-L1	-0.042	-0.015	0.000

Table 2: *Cell Parameter Differences*

		HDI			
Parameter	Comparison	2.5%	50%	97.5%	non-zero
AHP (mV) (μ)	FS-DS	5.722	7.226	8.693	yes
	IN-DS	1.046	3.110	5.166	yes
	IN-L1-DS	-0.301	1.355	2.945	
	IN-FS	-6.526	-4.097	-1.847	yes
	IN-L1-FS	-7.991	-5.868	-3.921	yes
	IN-L1-IN	-4.218	-1.751	0.650	
AP Height (mV) (μ)	FS-DS	-10.722	-6.932	-3.106	yes
	IN-DS	-15.933	-10.239	-4.850	yes
	IN-L1-DS	-15.873	-12.119	-8.184	yes
	IN-FS	-9.563	-3.309	2.827	
	IN-L1-FS	-10.350	-5.164	-0.244	yes
	IN-L1-IN	-7.903	-1.798	4.137	

Table 2: *Cell Parameter Differences*

		HDI			
Parameter	Comparison	2.5%	50%	97.5%	non-zero
Adaptation (μ)	FS-DS	0.092	0.263	0.514	yes
	IN-DS	0.072	0.301	0.661	yes
	IN-L1-DS	0.004	0.145	0.335	yes
	IN-FS	-0.281	0.033	0.417	
	IN-L1-FS	-0.386	-0.113	0.115	
	IN-L1-IN	-0.539	-0.149	0.103	
Cm (pF) (μ)	FS-DS	-50.323	-34.819	-18.197	yes
	IN-DS	-83.189	-65.188	-46.687	yes
	IN-L1-DS	-100.877	-86.905	-72.644	yes
	IN-FS	-50.064	-30.342	-9.464	yes
	IN-L1-FS	-68.405	-52.176	-35.972	yes
	IN-L1-IN	-41.052	-21.735	-3.673	yes
FWHM (ms) (μ)	FS-DS	-0.324	-0.283	-0.242	yes
	IN-DS	-0.133	-0.067	0.002	
	IN-L1-DS	-0.024	0.032	0.086	
	IN-FS	0.144	0.215	0.287	yes
	IN-L1-FS	0.254	0.315	0.375	yes
	IN-L1-IN	0.015	0.099	0.180	yes
Firing Frequency (Hz) (μ)	FS-DS	105.753	141.081	178.084	yes
	IN-DS	32.916	55.940	82.108	yes
	IN-L1-DS	5.032	16.037	28.060	yes
	IN-FS	-126.680	-84.319	-48.185	yes
	IN-L1-FS	-161.004	-124.802	-89.504	yes
	IN-L1-IN	-67.963	-39.833	-14.465	yes
Gain (Spikes/pA) (μ)	FS-DS	0.454	0.576	0.703	yes
	IN-DS	0.177	0.300	0.434	yes
	IN-L1-DS	0.222	0.318	0.425	yes
	IN-FS	-0.446	-0.276	-0.101	yes
	IN-L1-FS	-0.408	-0.258	-0.099	yes
	IN-L1-IN	-0.135	0.017	0.173	
ISI 1/2 (μ)	FS-DS	-0.042	-0.035	-0.027	yes
	IN-DS	-0.033	-0.021	-0.005	yes
	IN-L1-DS	-0.028	-0.019	-0.009	yes
	IN-FS	0.001	0.014	0.030	yes
	IN-L1-FS	0.006	0.016	0.027	yes
	IN-L1-IN	-0.014	0.002	0.016	

Table 2: *Cell Parameter Differences*

		HDI			
Parameter	Comparison	2.5%	50%	97.5%	non-zero
ISI 9/10 (µ)	FS-DS	-0.040	-0.034	-0.027	yes
	IN-DS	-0.033	-0.023	-0.013	yes
	IN-L1-DS	-0.028	-0.021	-0.013	yes
	IN-FS	0.001	0.010	0.021	yes
	IN-L1-FS	0.005	0.013	0.022	yes
	IN-L1-IN	-0.009	0.003	0.013	
ISI min (s) (µ)	FS-DS	-0.035	-0.031	-0.027	yes
	IN-DS	-0.030	-0.024	-0.018	yes
	IN-L1-DS	-0.025	-0.020	-0.014	yes
	IN-FS	0.002	0.007	0.012	yes
	IN-L1-FS	0.007	0.011	0.016	yes
	IN-L1-IN	-0.002	0.004	0.010	
Latency (s) (µ)	FS-DS	-0.084	-0.056	-0.025	yes
	IN-DS	-0.086	-0.055	-0.024	yes
	IN-L1-DS	-0.089	-0.063	-0.033	yes
	IN-FS	-0.033	0.000	0.035	
	IN-L1-FS	-0.042	-0.007	0.023	
	IN-L1-IN	-0.040	-0.007	0.021	
Negative Slope Slope (V/ms) (µ)	FS-DS	0.709	0.798	0.885	yes
	IN-DS	0.112	0.180	0.251	yes
	IN-L1-DS	-0.032	0.008	0.050	
	IN-FS	-0.729	-0.618	-0.514	yes
	IN-L1-FS	-0.886	-0.790	-0.698	yes
	IN-L1-IN	-0.255	-0.172	-0.097	yes
Positive Slope (V/ms) (µ)	FS-DS	0.101	0.141	0.185	yes
	IN-DS	-0.097	-0.060	-0.022	yes
	IN-L1-DS	-0.129	-0.105	-0.082	yes
	IN-FS	-0.252	-0.200	-0.148	yes
	IN-L1-FS	-0.290	-0.246	-0.201	yes
	IN-L1-IN	-0.087	-0.045	-0.009	yes
Rheobase (pA) (µ)	FS-DS	232.967	285.973	340.774	yes
	IN-DS	-19.328	16.469	59.706	
	IN-L1-DS	-11.470	15.654	46.268	
	IN-FS	-335.387	-268.664	-204.478	yes
	IN-L1-FS	-331.755	-270.182	-212.538	yes
	IN-L1-IN	-47.034	-1.179	45.103	

Table 2: *Cell Parameter Differences*

Parameter	Comparison	HDI			non-zero
		2.5%	50%	97.5%	
Rin MOhm (µ)	FS-DS	-51.700	-43.405	-35.010	yes
	IN-DS	22.494	46.920	73.665	yes
	IN-L1-DS	25.382	43.791	65.136	yes
	IN-FS	66.181	90.179	117.085	yes
	IN-L1-FS	68.543	87.173	108.053	yes
	IN-L1-IN	-36.713	-3.071	27.690	
Sag Ratio (µ)	FS-DS	0.007	0.028	0.047	yes
	IN-DS	0.018	0.045	0.072	yes
	IN-L1-DS	0.028	0.050	0.073	yes
	IN-FS	-0.009	0.017	0.042	
	IN-L1-FS	0.001	0.022	0.043	yes
	IN-L1-IN	-0.020	0.004	0.031	
Slope Ratio (µ)	FS-DS	0.007	0.028	0.047	yes
	IN-DS	0.018	0.045	0.072	yes
	IN-L1-DS	0.028	0.050	0.073	yes
	IN-FS	-0.009	0.017	0.042	
	IN-L1-FS	0.001	0.022	0.043	yes
	IN-L1-IN	-0.020	0.004	0.031	
Threshold (mV) (µ)	FS-DS	-3.868	-2.024	0.000	yes
	IN-DS	-1.412	0.873	3.144	
	IN-L1-DS	-0.464	1.672	3.800	
	IN-FS	-0.033	2.907	5.717	
	IN-L1-FS	0.683	3.721	6.740	yes
	IN-L1-IN	-1.696	0.726	3.559	
Vm (mV) (µ)	FS-DS	-1.475	-0.051	1.042	
	IN-DS	-0.951	0.093	1.846	
	IN-L1-DS	-1.185	0.026	1.313	
	IN-FS	-0.807	0.154	2.168	
	IN-L1-FS	-1.149	0.066	1.633	
	IN-L1-IN	-1.800	-0.047	0.949	
mAHP (mV) (µ)	FS-DS	-0.001	0.013	0.026	
	IN-DS	-0.002	0.009	0.023	
	IN-L1-DS	-0.002	0.008	0.022	
	IN-FS	-0.008	-0.002	0.002	
	IN-L1-FS	-0.010	-0.003	0.001	
	IN-L1-IN	-0.007	0.000	0.004	

Abbreviations

Table 3: *List of Abbreviations*

4-AP	4-Aminopyridine
ACSF	Artificial Cerebral Spinal Fluid
ACh	Acetylcholine
AHP	Afterhyperpolarisation
AMPA	α-amino-3-hydroxy-5-methyl-4-isoxazolepropionic acid
AP	Action Potential
CB	Calbindin
CCK	Cholecystokinin
C_m	Membrane Capacitance
ChAT	Choline Acetyltransferase
ChR2	Channelrhodopsin-2
DG	Dentage Gyrus
DHβE	Dihydro-β-erythroidine hydrobromide
DS	Delayed Spiking
EPSC	Excitatory Postsynaptic Current
EPSP	Excitatory Postsynaptic Potential
FIR	Finite Impulse Response
FS	Fast Spiking
FWHM	Full Width Half Maximum
GABA	γ-aminobutyric acid
HCN	Hyperpolarisation-Activated Cyclic Nucleotide-Gated Non-Selective Cation Channel
HDI	Highest Density Interval
IN	Interneuron
IPSC	Inhibitory Postsynaptic Current
IPSP	Inhibitory Postsynaptic Potential
ISI	Inter-Spike-Interval
LEC	Lateral Entorhinal Cortex
LFP	Local Field Potential
LOR	Log Odds Ratio
LRN	Low-Rhythmic Firing Neurons
MEC	Medial Entorhinal Cortex

Table 3: *List of Abbreviations*

MLA	Methyllycaconitine citrate
MS	Medial Septum
NBQX	2,3-Dioxo-6-nitro-1,2,3,4-tetrahydrobenzo[f]quinoxaline-7-sulfonamide
NMDA	N-Methyl-D-aspartic acid
PBS	Phosphate-Buffered Saline
PFA	Paraformaldehyde
PV	Parvalbumin
PaS	Parasubiculum
PrS	Presubiculum
ROPE	Region Of Practical Equivalence
R_{in}	Input Resistance
SAP	IgG192-Saporin
STDP	Spike Time Dependent Plasticity
TTX	Tetrodotoxin
VGAT	Vesicular Inhibitory Amino Acid Transporter
VR	Virtual Reality
V_m	Resting Membrane Potential
WFS1	Wolframin ER Transmembrane Glycoprotein
YFP	Yellow Fluorescent Protein
sACSF	Sucrose Artificial Cerebral Spinal Fluid

List of Figures

Statement of contributions

All experiments in this thesis were conceived and designed by my PhD supervisor Prof. Dr. Dietmar Schmitz and myself. All surgeries, *in-vivo* recordings and data analysis were performed by me.

Detailed contributions of other people to the data presented in this work include:

Dr. Rosanna Sammons (AG Schmitz, Neuroscience Research Centre, Charité Berlin) contributed 81/214 recordings of parasubicular cells.
Dr. Alexander Stumpf (AG Schmitz, Neuroscience Research Centre, Charité Berlin) contributed 29/214 recordings of parasubicular cells.
Susanne Rieckmann and **Anke Schönherr** organised breeding and performed genotyping of transgenic animals.

List of publications

Related to this dissertation

Sammons RP, **Parthier D**, Stumpf A, Schmitz D (2019) Electrophysiological and Molecular Characterization of the Parasubiculum. The Journal of Neuroscience: The Official Journal of the Society for Neuroscience 39:8860–8876.

Gonzalez-Sulser A, **Parthier D**, Candela A, McClure C, Pastoll H, Garden D, Sürmeli G, Nolan MF (2014) GABAergic projections from the medial septum selectively inhibit interneurons in the medial entorhinal cortex. J Neurosci 34:16739–16743.

Non-related to this dissertation

Beed P, Ray S, Velasquez LM, Stumpf A, **Parthier D**, Swaminathan A, Nitzan N, Breustedt J, Las L, Brecht M, Schmitz D (2020) Species-specific differences in synaptic transmission and plasticity. Scientific Reports 10:16557.

Kornau H-C, Kreye J, Stumpf A, Fukata Y, **Parthier D**, Sammons RP, Imbrosci B, Kurpjuweit S, Kowski AB, Fukata M, Prüss H, Schmitz D (2020) Human Cerebrospinal Fluid Monoclonal LGI1 Autoantibodies Increase Neuronal Excitability. Annals of Neurology 87:405–418.

Stumpf A, **Parthier D**, Sammons RP, Stempel AV, Breustedt J, Rost BR, Schmitz D (2018) Cannabinoid type 2 receptors mediate a cell type-specific self-inhibition in cortical neurons. Neuropharmacology 139:217–225.

Parthier D, Kuner T, Körber C (2018) The presynaptic scaffolding protein Piccolo organizes the readily releasable pool at the calyx of Held. The Journal of Physiology 596:1485–1499.

Rueckl M, Lenzi SC, Moreno-Velasquez L, **Parthier D**, Schmitz D, Ruediger S, Johenning FW (2017) SamuROI, a Python-Based Software Tool for Visualization and Analysis of Dynamic Time Series Imaging at Multiple Spatial Scales. Frontiers in Neuroinformatics 11:44.

Greifzu F, **Parthier D**, Goetze B, Schlüter OM, Löwel S (2016) Ocular Dominance Plasticity after Stroke Was Preserved in PSD-95 Knockout Mice. PLOS ONE 11:e0149771.

Zhang W, Schmelzeisen S, **Parthier D**, Frings S, Möhrlen F (2015) Anoctamin Calcium-Activated Chloride Channels May Modulate Inhibitory Transmission in the Cerebellar Cortex. PLOS ONE 10:e0142160.

Eidestattliche Erklärung

Hiermit versichere ich,

Daniel Parthier, an Eides statt, dass die vorliegende Arbeit von mir selbstständig und ohne unerlaubte Hilfe Dritter verfasst wurde und ich keine anderen als die angegebenen Quellen und Hilfsmittel verwendet sowie wörtliche und sinngemäße Zitate als solche kentlich gemacht habe.
Diese Arbeit hat in gleicher oder ähnlicher Form noch keiner anderen Prüfungsbehörde vorgelegen und wurde bisher nicht veröffentlicht.

Berlin, 28.09.2021